

**REDUCTION OF MIXTURE STRATIFICATION IN A CONSTANT-VOLUME
COMBUSTOR**

by

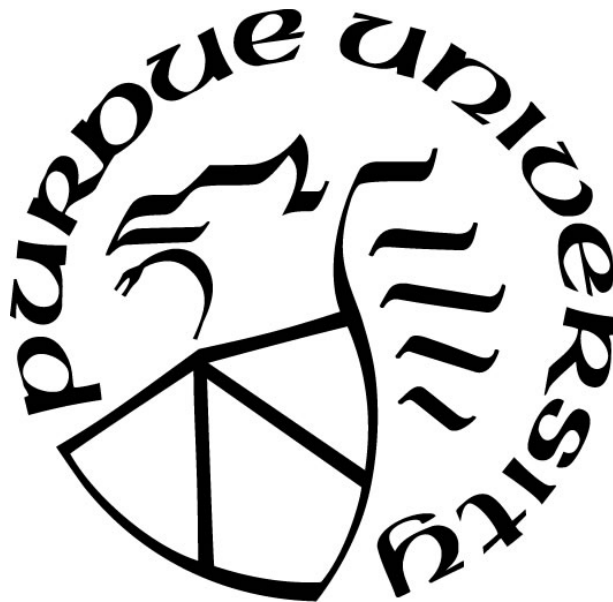
Richard Zachary Rowe

A Thesis

Submitted to the Faculty of Purdue University

In Partial Fulfillment of the Requirements for the degree of

Master of Science in Mechanical Engineering



Department of Mechanical and Energy Engineering at IUPUI

Indianapolis, Indiana

December 2021

THE PURDUE UNIVERSITY GRADUATE SCHOOL
STATEMENT OF COMMITTEE APPROVAL

Dr. M. Razi Nalim, Chair

Department of Mechanical and Energy Engineering

Dr. Carlos Larriba-Andaluz

Department of Mechanical and Energy Engineering

Dr. Huidan (Whitney) Yu

Department of Mechanical and Energy Engineering

Approved by:

Dr. Jie Chen

This thesis is dedicated to...

my family, who supported all of my academic and personal endeavors over the years;

my friends, who have seen me through it all and helped keep me sane;

and my lovely wife, who continually encouraged and gave me hope, even in the hardest of times.

ACKNOWLEDGMENTS

Many people and organizations are worthy of acknowledgements for helping me complete this accomplishment. Below are merely a few, but I can't thank all those who I have met during this journey enough. You have given me more than you can ever know, and I thank you for everything.

First off, I greatly thank and appreciate Dr. Mohamed Razi Nalim for all of his tremendous support and help over these past couple of years. His insight and experience was so helpful on this work, and overall, I could not have asked for a better mentor and research advisor.

Next, I want to give a huge thank you to the other professors on my thesis committee: Dr. Carlos Larriba-Andaluz and Dr. Huidan (Whitney) Yu. The patience and support from both of them during this difficult journey – both in the classroom and in my thesis work – was tremendously appreciated.

Of course, I can't go without giving thanks to everyone in the Combustion and Propulsion Research Lab who I have met and been inspired by every single day! Mohammed Ebrahim Feyz, Bhumika Sule, Chase Sumner, Swastik Ghume, Nirmala Priyanka Manthripragada, Rasheed Kehinde Yinusa, and Jared Miller: each of you has brought something great and unique to this lab over the years, and I would not have been able to make it through this thesis without each of your guys' help and support. Along with them, I'd like to thank all of the people in the IUPUI Department of Mechanical and Energy Engineering, especially Susan James, Jerry Mooney, and Linda Wright. Each of you has made my life easier whenever there was an academic issue, and I thank you for all that you do. Additionally, Keven Carr was a great help in fixing anything that seemed to go wrong in the lab, and without him, there would not have been a thesis.

A special thank you for Carrier Global is also in order. The financial support they provided me through the Carrier Research Fellowship was extremely generous, and I can't thank them enough for providing me the opportunity to focus on my work full time without financial worry.

Last, but certainly not least, I have to express my sincerest gratitude and appreciation to my mom Sandy Rowe, my dad Rick Rowe, my stepmom Jenna Rowe, my brother Zane Rowe, and my wife Racheal Benoy, as well as all of my friends that have stuck with me and supported me on this journey. It has been long, but I will always remember the parts each of you played in making it into a reality. Thank you.

TABLE OF CONTENTS

LIST OF TABLES	8
LIST OF FIGURES	9
GLOSSARY	14
ABSTRACT.....	16
1. INTRODUCTION	18
1.1 Pressure-Gain Combustion	18
1.1.1 Wave Rotor Systems.....	19
1.1.2 Wave Rotor Operation.....	20
1.1.3 Wave Rotor Development	23
1.2 Hot Jet Ignition	26
1.2.1 Hot Jet Ignition Delay Time Definition.....	27
1.3 IUPUI Combustion & Propulsion Research Lab	27
1.3.1 Prior Research.....	27
1.3.2 Objectives	28
1.3.3 Scope of Present Research.....	29
2. EXPERIMENTAL SETUP	31
2.1 Laboratory Facility.....	33
2.2 Main Chamber	33
2.2.1 XY Table	35
2.2.2 Recirculation Pump System.....	36
2.3 Pre-Chamber	36
2.3.1 Nozzle Insert.....	38
2.3.2 Diaphragm	39
2.4 Seal Plates and Leak Management	40
2.4.1 Spark Plug Seal Plate.....	40
2.4.2 O-Ring Seal Plate	41
2.4.3 Oil-Impregnated Bronze Seal Plate	42
2.4.4 Leakage Gap	43
2.5 Fueling System.....	45

2.5.1	Pre-Chamber Fueling.....	46
2.5.2	Main Chamber Fueling.....	47
2.6	Instrumentation and Data Acquisition.....	55
2.6.1	Electrical Systems.....	56
2.6.2	Ignition and Control System.....	57
2.6.3	Pre-Chamber Motor and Drive Control System	59
2.6.4	Remote Control Box	59
2.6.5	VFD Control Panel	60
2.6.6	LabVIEW VI Control Software.....	61
2.6.7	Magnetic Pickup Sensor	70
2.6.8	Pressure Transducers	71
2.6.9	Schlieren Imaging.....	72
2.6.10	Flame Luminosity Imaging	74
2.7	Ignition Process.....	74
2.7.1	Spark-Ignited Flame Process	74
2.7.2	Stationary Hot Jet Ignition Process.....	74
2.8	Experimental Procedure.....	75
2.8.1	Preparatory Steps	76
2.8.2	Steps for Spark-Ignited Flame Propagation Experiments	77
2.8.3	Steps for Stationary Hot Jet Ignition Experiments	78
2.8.4	Steps for Traversing Leak Analysis Experiments	79
2.8.5	Design of Experiments	79
3.	EXPERIMENTAL FINDINGS	81
3.1	Spark-Ignited Flame Experiments	81
3.1.1	Flame Front Propagation	81
3.1.2	Pressure Data Comparisons	95
3.1.3	Maximum Pressure Comparisons	102
3.2	Stationary Hot Jet Ignition Experiments.....	109
3.2.1	Ignition Delay Time.....	109
3.2.2	Shock Wave Speed	113
3.2.3	Pressure Data Comparisons	115

3.2.4	Visual Comparisons.....	123
3.3	Leak Analysis.....	128
3.3.1	Schlieren Visualization.....	128
3.3.2	Pressure Histories	129
3.3.3	Recommendations.....	131
4.	SUMMARY.....	132
4.1	Conclusions.....	132
4.2	Recommendations.....	134
	REFERENCES	137

LIST OF TABLES

Table 2.1. Main Chamber and Pre-Chamber Dimensions.	32
Table 2.2. MFC calibration constants for experimental fuels.....	55
Table 2.3. PCB Piezoelectric Pressure Transducer Information.....	72
Table 2.4. Experimental Design of Spark-Ignited Flame Tests.....	80
Table 2.5. Experimental Design of Stationary Hot Jet Ignition Tests.	80
Table 2.6. Experimental Design of Traversing Leakage Tests.	80

LIST OF FIGURES

Figure 1.1. An exploded-view illustration of a wave rotor system, with the top depicting the inlet side and the bottom displaying the outlet side [5].	20
Figure 1.2. A T-S plot diagram featuring an ideal Brayton and Humphrey cycle, along with a small diagram featuring which line represents each point in the WRC-gas turbine system [5].....	21
Figure 1.3. Schematic diagrams of a wave rotor combustor feature several ways to view the system, including an exploded-out view on the right and an unraveled view on the left [9].	22
Figure 2.1. Schematic Diagram of ET 109a with views of the apparatus and all fueling and data acquisition subsystems [42].	33
Figure 2.2. This picture shows a side profile view of the main chamber and its corresponding labels.	35
Figure 2.3. Picture showing the inside of the pre-chamber [42].....	37
Figure 2.4. Two side of the nozzle insert: a.) this is the backside of the nozzle that is inserted into the pre-chamber, and b.) this shows the front face of the nozzle with a pencil line showing where the main chamber opening lies in relation to the nozzle.....	39
Figure 2.5. The spark plug seal plate with mounted Champion FI21501 spark plug viewed from the a.) front and b.) back of the plate.	41
Figure 2.6. The O-ring seal plate used in stationary hot jet experiments viewed from the a.) front and b.) back.	42
Figure 2.7. The oil-impregnated bronze plate used in traversing hot jet experiments viewed from the a.) front and b.) back.	43
Figure 2.8. The a.) flexible rope clamp employed during traversing jet experiments and b.) c-clamp used for stationary jet experiments help maintain a consistent clamping force between the main chamber and pre-chamber.....	44
Figure 2.9. A photo of Kojok’s volume displacement method, using the MFC, a burette, and an acrylic tube container with water [7].	49
Figure 2.10. Methane calibration plots showing a.) delivered fuel mass vs time results and b.) error between the MFC reported volume and the actual delivered volume.	50
Figure 2.11. 50%-50% Methane-Hydrogen calibration plots showing a.) delivered fuel mass vs time results and b.) error between the MFC reported volume and the actual delivered volume..	51
Figure 2.12. Hydrogen calibration plots showing a.) delivered fuel mass vs time results and b.) error between the MFC reported volume and the actual delivered volume.....	52
Figure 2.13. 46.4%-53.6% Methane-Argon calibration plots showing a.) delivered fuel mass vs time results and b.) error between the MFC reported volume and the actual delivered volume..	53

Figure 2.14. Propane calibration plots showing a.) delivered fuel mass vs time results and b.) error between the MFC reported volume and the actual delivered volume.	54
Figure 2.15. Direction of flow of signals and data throughout the instrumentation and data acquisition systems [42].....	55
Figure 2.16. Diagram of the experimental apparatus' and remote control panel's electrical systems [42].....	57
Figure 2.17. Diagram of the circuit controlling the MFC fueling, spark plug triggering, and system synchronization [7].	58
Figure 2.18. The remote control box, featuring labels on all safety switches and buttons [42]. ..	60
Figure 2.19 Interface for the MFC calibration VI.....	62
Figure 2.20. Block diagram of the mfc_calibration.vi file.	63
Figure 2.21. Interface for the spark-ignited flame propagation VI.....	64
Figure 2.22. Block diagram of the spark-ignited flame VI file.	65
Figure 2.23. Interface for the stationary HJI VI.....	66
Figure 2.24. Block diagram of the stationary HJI VI file.	67
Figure 2.25. Interface for the leak analysis/traversing HJI VI.....	68
Figure 2.26. Block diagram of the leak analysis/traversing HJI VI file.	69
Figure 2.27. Image of the magnetic pickup sensor and its corresponding magnet [42].	70
Figure 2.28. A schematic diagram of the lab's schlieren setup, showing positions and relative angles of the light source, mirrors, camera, razor blade, and lab equipment [42].....	73
Figure 3.1. Schlieren filmstrips for five methane ($\Phi=1$) test cases: a) Trial 127: $\tau_{mix}=0s$, no pump; b) Trial 130: $\tau_{mix}=10s$, no pump; c) Trial 137: $\tau_{mix}=10s$, pump; d) Trial 135: $\tau_{mix}=30s$, no pump; e) Trial 140: $\tau_{mix}=30s$, pump.	83
Figure 3.2. Schlieren filmstrips for five 50%-50% methane-hydrogen ($\Phi=1$) test cases: a) Trial 186: $\tau_{mix}=0s$, no pump; b) Trial 190: $\tau_{mix}=10s$, no pump; c) Trial 210: $\tau_{mix}=10s$, pump; d) Trial 194: $\tau_{mix}=30s$, no pump; e) Trial 214: $\tau_{mix}=30s$, pump.	84
Figure 3.3. Schlieren filmstrips for five hydrogen ($\Phi=1$) test cases: a) Trial 235: $\tau_{mix}=0s$, no pump; b) Trial 239: $\tau_{mix}=10s$, no pump; c) Trial 260: $\tau_{mix}=10s$, pump; d) Trial 241: $\tau_{mix}=30s$, no pump; e) Trial 263: $\tau_{mix}=30s$, pump.	85
Figure 3.4. Schlieren filmstrips for four 46.4%-56.3% methane-argon ($\Phi=1$) test cases: a) Trial 433: $\tau_{mix}=10s$, no pump; b) Trial 472: $\tau_{mix}=10s$, pump; c) Trial 442: $\tau_{mix}=30s$, no pump; d) Trial 479: $\tau_{mix}=30s$, pump.....	86
Figure 3.5. Schlieren filmstrips for five propane ($\Phi=1$) test cases: a) Trial 309: $\tau_{mix}=0s$, no pump; b) Trial 312: $\tau_{mix}=10s$, no pump; c) Trial 395: $\tau_{mix}=10s$, pump; d) Trial 315: $\tau_{mix}=30s$, no pump; e) Trial 396: $\tau_{mix}=30s$, pump.....	87

Figure 3.6. Flame luminosity filmstrips for 3 methane ($\Phi=1$) test cases: a) Trial 127: $\tau_{\text{mix}}=0\text{s}$, no pump; b) Trial 135: $\tau_{\text{mix}}=30\text{s}$, no pump; c) Trial 140: $\tau_{\text{mix}}=30\text{s}$, pump.....	90
Figure 3.7. Flame luminosity filmstrips for 3 methane-hydrogen ($\Phi=1$) test cases: a) Trial 186: $\tau_{\text{mix}}=0\text{s}$, no pump; b) Trial 194: $\tau_{\text{mix}}=30\text{s}$, no pump; c) Trial 214: $\tau_{\text{mix}}=30\text{s}$, pump.....	91
Figure 3.8. Flame luminosity filmstrips for 3 methane ($\Phi=1$) test cases: a) Trial 235: $\tau_{\text{mix}}=0\text{s}$, no pump; b) Trial 241: $\tau_{\text{mix}}=30\text{s}$, no pump; c) Trial 263: $\tau_{\text{mix}}=30\text{s}$, pump.....	92
Figure 3.9. Flame luminosity filmstrips for 2 methane-argon ($\Phi=1$) test cases: a) Trial 442: $\tau_{\text{mix}}=30\text{s}$, no pump; b) Trial 479: $\tau_{\text{mix}}=30\text{s}$, pump.....	93
Figure 3.10. Flame luminosity filmstrips for 3 propane ($\Phi=1$) test cases: a) Trial 309: $\tau_{\text{mix}}=0\text{s}$, no pump; b) Trial 315: $\tau_{\text{mix}}=30\text{s}$, no pump; c) Trial 396: $\tau_{\text{mix}}=30\text{s}$, pump.....	94
Figure 3.11. Pressure history plots for five methane ($\Phi=1$) test cases: a) Trial 127: $\tau_{\text{mix}}=0\text{s}$, no pump; b) Trial 130: $\tau_{\text{mix}}=10\text{s}$, no pump; c) Trial 137: $\tau_{\text{mix}}=10\text{s}$, pump; d) Trial 135: $\tau_{\text{mix}}=30\text{s}$, no pump; e) Trial 140: $\tau_{\text{mix}}=30\text{s}$, pump.....	97
Figure 3.12. Pressure history plots for five 50%-50% methane-hydrogen ($\Phi=1$) test cases: a) Trial 186: $\tau_{\text{mix}}=0\text{s}$, no pump; b) Trial 190: $\tau_{\text{mix}}=10\text{s}$, no pump; c) Trial 210: $\tau_{\text{mix}}=10\text{s}$, pump; d) Trial 194: $\tau_{\text{mix}}=30\text{s}$, no pump; e) Trial 214: $\tau_{\text{mix}}=30\text{s}$, pump.....	98
Figure 3.13. Pressure history plots for five hydrogen ($\Phi=1$) test cases: a) Trial 235: $\tau_{\text{mix}}=0\text{s}$, no pump; b) Trial 239: $\tau_{\text{mix}}=10\text{s}$, no pump; c) Trial 260: $\tau_{\text{mix}}=10\text{s}$, pump; d) Trial 241: $\tau_{\text{mix}}=30\text{s}$, no pump; e) Trial 263: $\tau_{\text{mix}}=30\text{s}$, pump.....	99
Figure 3.14. Pressure history plots for four 46.4%-56.3% methane-argon ($\Phi=1$) test cases: a) Trial 433: $\tau_{\text{mix}}=10\text{s}$, no pump; b) Trial 472: $\tau_{\text{mix}}=10\text{s}$, pump; c) Trial 442: $\tau_{\text{mix}}=30\text{s}$, no pump; d) Trial 479: $\tau_{\text{mix}}=30\text{s}$, pump.....	100
Figure 3.15. Pressure history plots for five propane ($\Phi=1$) test cases: a) Trial 309: $\tau_{\text{mix}}=0\text{s}$, no pump; b) Trial 312: $\tau_{\text{mix}}=10\text{s}$, no pump; c) Trial 395: $\tau_{\text{mix}}=10\text{s}$, pump; d) Trial 315: $\tau_{\text{mix}}=30\text{s}$, no pump; e) Trial 396: $\tau_{\text{mix}}=30\text{s}$, pump.....	101
Figure 3.16. Maximum gauge pressure vs equivalence ratio for methane.	102
Figure 3.17. Maximum gauge pressure vs equivalence ratio for methane-hydrogen.	103
Figure 3.18. Maximum gauge pressure vs equivalence ratio for hydrogen.	104
Figure 3.19. Maximum gauge pressure vs equivalence ratio for methane-argon.....	105
Figure 3.20. Maximum gauge pressure vs equivalence ratio for propane.	106
Figure 3.21. Maximum gauge pressure vs equivalence ratio for all of the spark flame data.	107
Figure 3.22. Maximum gauge pressure vs equivalence ratio for 0s, no pump (NP); 30s, no pump (NP); and 30s, pump (YP) spark flame data.	108
Figure 3.23. Ignition delay time vs equivalence ratio for methane.	111
Figure 3.24. Ignition delay time vs equivalence ratio for methane-hydrogen.	111

Figure 3.25. Ignition delay time vs equivalence ratio for propane.	112
Figure 3.26. Ignition delay time vs equivalence ratio for all stationary jet data.....	112
Figure 3.27. Shock speed vs equivalence ratio for methane.	113
Figure 3.28. Shock speed vs equivalence ratio for methane-hydrogen.	114
Figure 3.29. Shock speed vs equivalence ratio for propane.	114
Figure 3.30. Shock speed vs equivalence ratio for all stationary jet data.	115
Figure 3.31. Pressure history plots for two methane ($\Phi=1$) stationary cases: a) Trial 43: $\tau_{mix}=0s$, no pump; b) Trial 68: $\tau_{mix}=30s$, pump.	116
Figure 3.32. Pressure history plots for two 50%-50% methane-hydrogen ($\Phi=1$) stationary cases: a) Trial 156: $\tau_{mix}=0s$, no pump; b) Trial 169: $\tau_{mix}=30s$, pump.	117
Figure 3.33. Pressure history plots for two hydrogen ($\Phi=1$) stationary cases: a) Trial 125: $\tau_{mix}=0s$, no pump; b) Trial 138: $\tau_{mix}=30s$, pump.	118
Figure 3.34. Pressure history plots for two propane ($\Phi=1$) stationary cases: a) Trial 182: $\tau_{mix}=0s$, no pump; b) Trial 193: $\tau_{mix}=30s$, pump.	119
Figure 3.35. Maximum gauge pressure vs equivalence ratio for methane.	120
Figure 3.36. Maximum gauge pressure vs equivalence ratio for methane-hydrogen.	121
Figure 3.37. Maximum gauge pressure vs equivalence ratio for hydrogen.	121
Figure 3.38. Maximum gauge pressure vs equivalence ratio for propane.	122
Figure 3.39. Maximum gauge pressure vs equivalence ratio for all stationary data.	122
Figure 3.40. Filmstrips for two methane ($\Phi=1$) test cases: a) schlieren and b) flame luminosity for Trial 43: $\tau_{mix}=0s$, no pump; c) schlieren and d) flame luminosity for Trial 68: $\tau_{mix}=30s$, pump.	124
Figure 3.41. Filmstrips for two methane-hydrogen ($\Phi=1$) test cases: a) schlieren and b) flame luminosity for Trial 156: $\tau_{mix}=0s$, no pump; c) schlieren and d) flame luminosity for Trial 169: $\tau_{mix}=30s$, pump.	125
Figure 3.42. Filmstrips for two hydrogen ($\Phi=1$) test cases: a) schlieren and b) flame luminosity for Trial 125: $\tau_{mix}=0s$, no pump; c) schlieren and d) flame luminosity for Trial 138: $\tau_{mix}=30s$, pump.	126
Figure 3.43. Filmstrips for two propane ($\Phi=1$) test cases: a) schlieren and b) flame luminosity for Trial 182: $\tau_{mix}=0s$, no pump; c) schlieren and d) flame luminosity for Trial 193: $\tau_{mix}=30s$, pump.	127
Figure 3.44. Video links for two propane ($\Phi=2$) 0 RPM top-to-bottom pump leak test case, with a.) the first video of the front of the main chamber and b.) the second video being the back of the main chamber.	128

Figure 3.45. Video links for two propane ($\Phi=2$) 400 RPM top-to-bottom pump leak test case, with a.) the first video of the front of the main chamber and b.) the second video being the back of the main chamber..... 129

Figure 3.46. Pressure history plots for a propane ($\Phi=2$) a.) 0 RPM top-to-bottom pump leak test case and b.) 400 RPM top-to-bottom pump leak test case..... 130

GLOSSARY

$A/F_{\text{stoichiometric}}$	Stoichiometric Air-Fuel Ratio
ABB	Asea Brown Boveri
B2T	Bottom-to-Top
BBC	Brown Boveri Company
CPRL	Combustion & Propulsion Research Lab
DARPA	Defense Advanced Research Projects Agency
DOE	Department of Energy
ET	Engineering & Technology Building
GE	General Electric
GPC	General Power Corporation
GRC	Glen Research Center
HJI	Hot Jet Ignition
ICWR	Integrated Combustion Wave Rotor
IUPUI	Indiana University – Purdue University Indianapolis
k	Fuel Slope Calibration Factor
M_{air}	Molecular Weight of Air
MFC	Mass Flow Controller
m_{fuel}	Mass of fuel
NASA	National Aeronautics and Space Administration
NI	National Instruments
ONR	Office of Naval Research
PCC	Phantom Camera Control
PGC	Pressure-Gain Combustion
P_{initial}	Initial Pressure
PT	Pressure Transducer
P_{total}	Total Pressure
RPM	Rotations Per Minute
S	Entropy
SCCM	Standard Cubic Centimeters per Minute

T	Temperature
T2B	Top-to-Bottom
T _{air}	Temperature of Air
t _{mix}	Mixing Time
t _{set}	Setpoint Signal Time
V	Voltage
VFD	Variable Frequency Drive
VI	Virtual Instrument
WRC	Wave Rotor Combustor

ABSTRACT

This study contributes to a better working knowledge of the equipment being used in a well-established combustion lab. In particular, several constant-volume combustion properties (e.g., time ignition delay, flame propagation, and more) are examined to deduce any buoyancy effects between fuel and air mixtures and to develop a method aimed at minimizing such effects. This study was conducted on an apparatus designed to model the phenomena occurring within a single channel of a wave rotor combustor, which consists of a rotating cylindrical pre-chamber and a fixed rectangular main combustion chamber. Pressure sensors monitor the internal pressures within the both chambers at all times, and two slow-motion videography techniques visually capture combustion phenomena occurring within the main chamber. A new recirculation pump system has been implemented to mitigate stratification within the chamber and produce more precise, reliable results. The apparatus was used in several types of experiments that involved the combustion of various hydrocarbon fuels in the main chamber, including methane, 50%-50% methane-hydrogen, hydrogen, propane, and 46.4%-56.3% methane-argon. Additionally, combustion products created in the pre-chamber from a 1.1 equivalence ratio reaction between 50%-50% methane-hydrogen and air were utilized in the issuing pre-chamber jet for all hot jet ignition tests. In the first set of experiments, a spark plug ignition source was used to study how combustion events travel through the main chamber after different mixing methods were utilized – specifically no mixing, diffusive mixing, and pump circulation mixing. The study reaffirmed that stratification between fuel-air mixtures occurs in the main chamber through the presence of asymmetrical flame front propagation. Allowing time for mixing, however, resulted in more symmetric flame fronts, broader pressure peaks, and reduced combustion time in the channel. While 30 seconds of diffusion helped, it was found that 30 seconds of pumping (at a rate of 30 pumps per 10 seconds) was the most effective method at reducing stratification effects in the system. Next, stationary hot jet ignition experiments were conducted to compare the time between jet injection and main chamber combustion and the speed of the resulting shockwaves between cases with no mixing and 30 seconds of pump mixing. Results continued to show an improvement with the pump cases; ignition delay times were typically shorter, and shock speeds stayed around the same, if not increased slightly. These properties are vital when studying and developing wave rotor combustors, and therefore, reducing stratification (specifically by means of a recirculation

system) should be considered a crucial step in laboratory models such as this one. Lastly, experiments between a fueled main chamber and rotating pre-chamber helped evaluate the leakage rate of the traversing hot jet ignition experimental setup paired with the new pump system. In its current form, major leaks are inevitable when attempting traversing jet experiments, especially with the pump's suction action drawing sudden large plumes of outside air into the main chamber. To minimize leaks, gaps between the pre-chamber and main chamber should be reduced, and the contact surface between the two chambers should be more evenly distributed. Also, the pump system should only be operated as long as needed to evenly distribute the fuel-air mixture, which approximately happens when the main chamber's total volume has been circulated through the system one time. Therefore, a new pump system with half of the original system's volume was developed in order to decrease the pumping time and lower the risk of leaks.

1. INTRODUCTION

As people continue to develop and work toward a technological future, the demand for a more environmentally conscious society is growing continuously. Cars are moving to more hybrid and electric options. Renewable energy sources are becoming more abundant. And reusable materials are being widely adopted. However, progress is slow-going at times, and with the recent relaxations on Covid-19 restrictions causing an increase in land and air travel, it's obvious that both fossil fuels and combustion engine systems are still here to stay for quite some time. As industries continue to push the bounds of efficiency on current devices, researchers should also look at challenging these norms with novel, innovative designs and concepts that further enhance and supplement current energy systems' overall efficiency, power output, and emission standards.

The point of this thesis is to aid in the development of such concepts, specifically in the practices around and configurations of models used to study pressure-gain combustion (PGC). While small, the field of PGC is growing and shows great promise in aiding many combustion systems that are used daily. Computational and analytical work has been performed on these systems over the years, but experimental work is vital in order to provide essential validation for the theories that have been put forth and to help make these helpful tools more of a reality. In order to do this, though, the experimental models themselves need to be carefully designed and thought out to ensure that the systems they reflect are being accurately represented. Fuel stratification, for example, can cause numerous effects on combustion events as a whole. But, if it were to occur in a model whose analogous system shouldn't experience such a phenomenon, then it should be accounted for and minimized if possible. This thesis experimentally examines this exact situation for a specific wave rotor combustor model and seeks to improve its operational accuracy – not only for the sake of this work but also for that of all the future works to come from any institution working with these systems.

1.1 Pressure-Gain Combustion

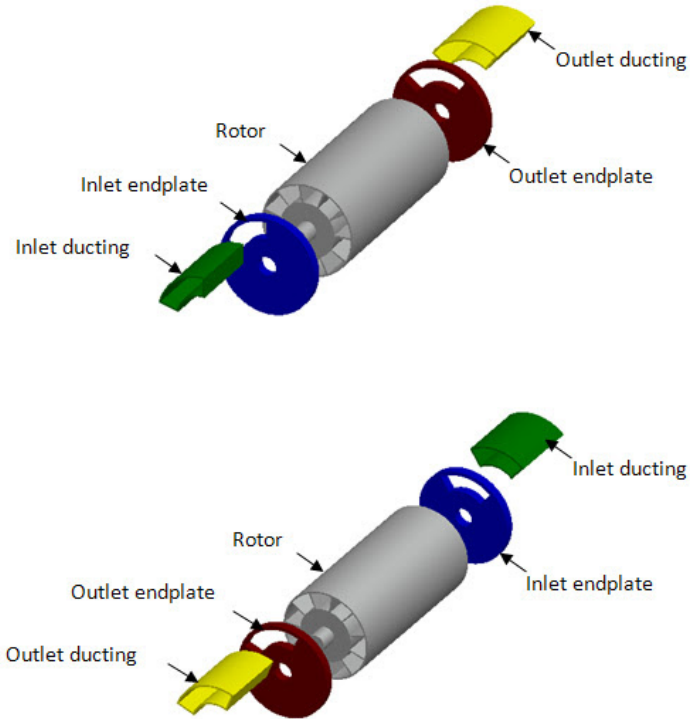
Pressure-gain combustion is a form of combustion in which a constant-volume combustion process is utilized to produce high pressure gases. In an internal combustion engine, for example, the combustion process occurring in the piston cylinder results in work being performed by the

gas products on the surroundings to push the piston down and expand the volume of the chamber. While effective, constant-volume combustion stores the energy that would have been wasted during this expansion process and utilizes it later. Made into a cyclic process, constant-volume combustion is considered by many as thermodynamically advantageous over such systems [1].

The key to success in PGC systems is their ability to balance steady and unsteady flow. While steady flow is maintained at the inlet and outlet of the devices themselves, unsteady flow properties found within help generate the characteristic high stagnation pressures of the outflow [2]. These devices can be particularly advantageous when placed in turbomachinery systems, in which the high-pressure products of the combustor can be exhausted directly into a turbine system – thus producing more work from the turbine while requiring less fuel to do so. There are several examples of PGC applications that exist today, including pulse detonation engines, rotating detonation engines, pulse jets, wave rotor combustors, and more. Wave rotor combustors (WRCs) are of particular interest in this study and will be discussed in further detail in the following subsections.

1.1.1 Wave Rotor Systems

Wave rotors are a kind of pressure wave machine utilizing unsteady flow in order to produce pressure waves that act as vehicles for transferring energy. With certain geometries, even, such devices can generate internal compression and expansion waves that are able to directly transfer energy between different fluids within the machine and can do so without the need of additional components (e.g. pistons, vanes, etc.) [3]. To add to this, these machines can generate large pressures within short time- and length-scales [4], which make them perfect devices to keep up with and exchange high pressure gasses with turbine fan systems. And what is more amazing is that they are fairly simple in their construction. Wave rotors primarily consist of a cylindrical drum containing an array of axial channels that rotate between two fixed endplates. In the simplest of constructions, such as that seen in Fig. 1.1, there is at least one port on each endplate that acts as an inlet and outlet for the rotating channels and that controls the flow through the drum. These ports also serve as generators for the necessary pressure waves within each channel; as the drum rotates, the ports open and close on either side of each channel, resulting in expansion and compression waves being formed, respectively.



Wave rotors are designated as one of two groups of rotors based on their functionality. One kind is known as a pressure exchange wave rotor, and it serves as a method of exchanging energy between two fluids with different pressure levels. And the other type is known as a wave rotor combustor, which utilizes each rotor channel as a constant-volume combustion chamber to produce high pressure gases at the outlet [6]. The current study focuses on these wave rotor combustors and models the constant-volume combustion and hot jet ignition processes that are critical components to these systems. Readers wanting to learn more about pressure exchange wave rotors can refer to Akbari et al. [1]. To fully understand current WRC technology, though, the following subsections delve into how these machines operate and how they have developed over time.

1.1.2 Wave Rotor Operation

A wave rotor combustor is often best used in-line with a gas turbine system, as it improves the efficiency and output of the system. How it does this, however, involves the thermodynamic nature of the WRC system. A typical gas turbine cycle can be represented by a constant-pressure

combustion process known as a Brayton cycle; in contrast, a WRC is a constant-volume combustion process known as a Humphrey cycle. Given that there is a constant inlet temperature and outlet pressure in both systems, the two cycles are best visualized on the temperature (T)-Entropy (S) diagram in Fig. 1.2, with the Humphrey cycle making up the 1-2-3-4 line and the Brayton cycle making up the 1-2-3_b-4_b line. In this application, the Brayton cycle involves a compressor spool increasing the air pressure (line 1-2), a constant-pressure combustion event causing heat addition to the system (line 2-3_b), the now-high pressure and temperature gas expanding in the turbine to produce shaft work (line 3_b-4_b), and the system rejecting the remaining heat to return to the starting position (4_b-1) [7]. In the Humphrey cycle, on the other hand, the heat addition process is different; here, the heat addition derives from a constant-volume combustion process (line 2-3), which instead results in a gain in pressure and a reduction in entropy generated by the cycle. In fact, a study by Akbari once estimated that the reduction in entropy generation could be up to 25% compared with a similar Brayton cycle process [6]. The overall result of this ends up being that, for the same amount of input energy, power generated by the turbine system not only increases but also becomes more efficient.

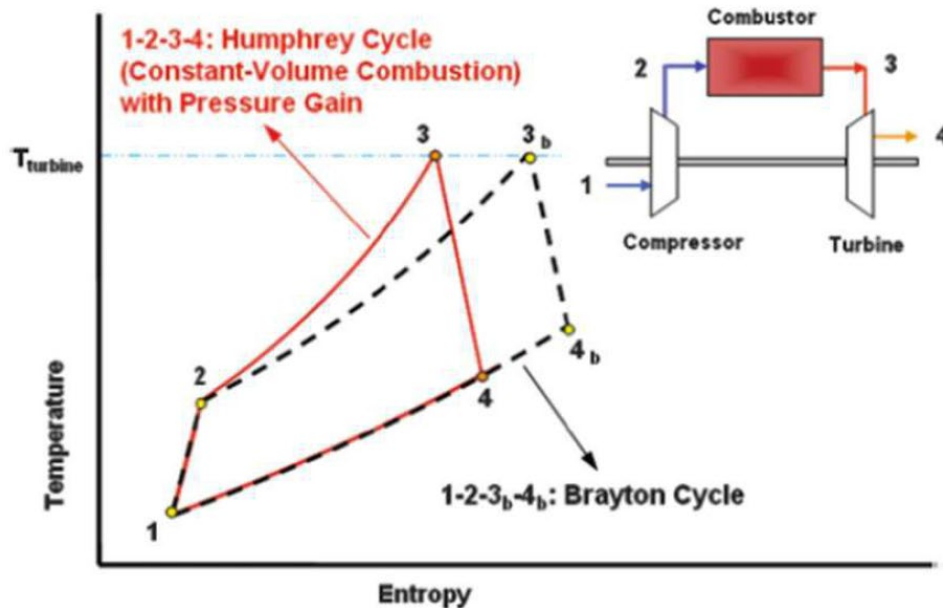


Figure 1.2. A T-S plot diagram featuring an ideal Brayton and Humphrey cycle, along with a small diagram featuring which line represents each point in the WRC-gas turbine system [5].

For these systems to work, they must operate quickly for the combustion to fully occur by the time the wave rotor finishes on complete cycle in its rotation - an added benefit of which is that it reduces nitrogen oxide emissions [8]. To visualize what is happening within the wave rotor itself, imagine cutting a line along the length of the cylindrical rotor and unrolling it like an orange, like in Figure 1.3b. Starting with the middle-most channels, the high pressure combustion products have just left the channels through the outlet port on the right side of the rotor diagram, and once exposed to the left-side inlet port, the channels are exposed to and fueled with a fuel-air mixture. Next, moving up in the diagram with the rotation of the rotor, the exhaust port eventually shuts close on the right side, causing a hammer shock to travel through the channel and compress its contents. Moving along, the channel aligns with an ignition source, which combusts the fuel mixture within the channel. This combustion event causes the gas products to expand rapidly. Upon rotating a little more, the channel is exposed to the outlet port on the right side of the channel, which causes an expansion wave to propagate leftward as the high-pressure gas products stream out of the channel. This process then repeats for each channel as the rotor continues its rotation.

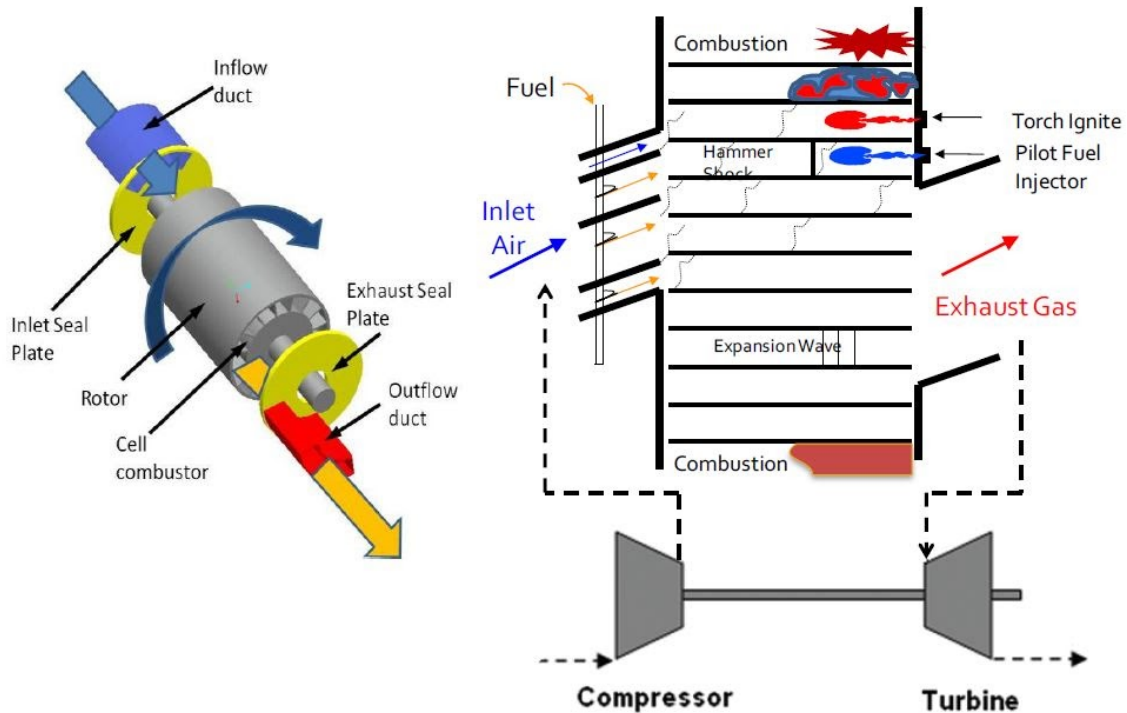


Figure 1.3. Schematic diagrams of a wave rotor combustor feature several ways to view the system, including an exploded-out view on the right and an unraveled view on the left [9].

There are several key features to the above description that also contribute to the benefits of these systems. For example, the ignition source used to ignite the fuel-air mixture can be a traditional torch ignitor, or it can be a small stream of chemically active combustion product radicals that have been diverted from the exhausting gas to a channel further in the rotation. This method is a great way to make the system even more energy efficient, and this hot jet ignition process will be discussed further in Sect. 1.2. Additionally, combustion events can occur in both deflagration and detonation modes; although, the deflagration mode is the most preferred of the two, as it has already been experimentally built and operated as well as rotating detonation engine systems already being more established [9, 10, 11]. Lastly, the location of the ports is precisely placed to ensure the channels have enough time to fully combust while also creating the necessary expansion waves needed for the fuel-air mixture to fill the entire channel. An important note to make though is that, even with this expansion wave filling process, the fuel-air mixture in each channel can be stratified along the length of the channel (i.e., longitudinally) [8], with there being a richer fuel-air mixture towards the inlet side of the channel. While this form of stratification can be present, latitudinal stratification should not be found at all, and for this reason, this study specifically focused on reducing latitudinal stratification in a laboratory WRC model.

1.1.3 Wave Rotor Development

The earliest origins of a pressure wave machine can be traced back to a design proposed by Knauff in 1906 for a pressure exchanger that exchanges pressure levels between fluids by way of a cellular drum rotating between two seal plats [12]. This inspired more designs by Knauff [13], Burghard [14], and Lebre [15] in 1906, 1913, and 1928 respectively. These newer designs became known as a Lebre's machine and exchanged pressure between fluids through long, narrow channels. By 1928, Burghard patented a cell rotor device where in compressible fluids entering the elongated cells making up the rotating wheel compress the fluid within the cell through use of a pressure wave [16]. While rotating, the cells are systematically opened and closed at specific times to complete a full cycle of compression and discharge during one rotation of the drum.

The first practical application of a pressure wave exchanger was made in 1942 as part of a superstage for a gas turbine compressor by the Brown Boveri Company (BBC), which later became known as Asea Brown Boveri (ABB) [17]. Over the years, ABB developed the idea further and began deploying their devices in trucks and diesel engines throughout the 1970s until it developed

into the Comprex car supercharger system by 1988, when it was implemented into passenger cars and became the most commercially successful wave rotor device out there. The first cars to sport them were the Mazda 626 Capella's, followed by Mercedes-Benz, Ferrari, and Peugeot. This would later spawn many other projects, as well - such as topping a gas turbine cycle with a pressure wave supercharger [18] and designing a fully working, highly performing integrated combustion wave rotor (ICWR) demonstrator engine [17].

By the 1950s, other organizations had begun looking into wave rotor technology and trying to find useful applications for them. The Cornell Aeronautical Laboratory employed a massive 2m wave superheater as part of an air supply unit for their hypersonic wind tunnel system. UK-based Power Jets Ltd eventually developed two wave rotor systems for an air-cycle refrigerator that was to be used in gold mines found in India and South Africa. Additionally, the Ruston-Hornsby Turbine Company managed to successfully operate at speeds ranging from 3000 to 18000 RPM and generate up to 26kW of power [19]. General Electric (GE) made impressive developments on a form of internal combustion wave rotor system by 1958, reaching pressure ratios of up to 1.3 until they hit with expansion and sealing problems with the rotor [20]. Partnering with Ford and later the United States Department of Energy (DOE) and U.S. Defense Advanced Research Projects Agency (DARPA) in the 1960s-1985, the General Power Corporation (GPC) worked on a wave rotor that would join a gas turbine system in automotive applications. However, GPC designed the device to utilize curved blade channels to generate shaft power, but this design proved to be too inefficient [21]. From 1965-1972, Rolls Royce tried developing a wave rotor topping stage for a small helicopter engine called Allison Model 250. After considerable effort, the design suffered a multitude of issues, including leaks, start up issues, bearing durability problems, and other various control issues [22.]. From 1978-1985, Mathematical Science Northwest, Inc. designed a laboratory model of a wave rotor with help from the DOE and DARPA. The lab results ended up matching well with the numerical analysis done beforehand using an unsteady flow code. By the end, they were able to design a small turbofan engine capable of generating 600lbs of thrust [23]. During the 1980s, the Office of Naval Research (ONR) joined a joint project with DARPA in which they performed a thorough analytical and computational breakdown of wave rotor systems, which included taking the GE wave rotor mentioned previously to the Turbopropulsion Laboratory. Not only did they manage to produce shaft work at around 5-6000 RPM, but also, they developed a 2D code meant to study fluid flow through wave rotor channels.

A lot of this research still continues to this day even. The NASA Glen Research Center (GRC) and Rolls Royce, for example, have long worked together on an application for wave rotors in aircraft propulsion [10]. NASA GRC also developed a quasi-1D code used to estimate the performance of a wave rotor combustor through the efforts of Nalim and Paxson, who later confirmed their results through experimental validation [24]. Additionally, Rolls Royce Allison was able to produce an 18-20% specific power increase with an accompanying 15-20% specific fuel consumption decrease for their Allison 250 turboshaft engine [25]. Also, during the 1990s, Nalim and Paxson performed a feasibility study assessing combustion in wave rotor channels as part of a pressure-gain combustion system, and Paxson took the opportunity to further develop their wave rotor code with combustion prediction abilities [8]. Several others developed codes of their own during this time as well, especially those at universities. Researchers at the University of Florida looked at flow in a wave rotor and adjoining duct and developed their own models to analyze it both analytically and numerically. This code was then used to model both NASA's three-port wave rotor as well as the GPC rotor [26]. Likewise, several university researchers at the University of Tokyo have worked to develop a code modeling NASA's four-port wave rotor system [27]. In terms of experimental work, Michigan State University has previously looked at micro-turbine systems with accompanying wave rotor topping cycles [1]. Lastly, the IUPUI CPRL group has been performing both computational and experimental wave rotor combustor research under the guidance of Dr. Razi Nalim; more on this past work will be discussed later in Sect. 1.3.1. More information regarding the history and development of wave rotor systems can be found in Akbari's research [6].

Overall, despite the hardships in studying these over the past several decades, wave rotor systems and constant-volume combustion units as a whole show a lot of promise in potential thermodynamic efficiency and improved work capability. Not only that, but they do so with the added benefit of offering less nitric oxide emissions as well as other benefits that come with their inherent operation, such as self-cooling and utilizing unsteady processes in a continuous manner. For these and many other reasons, they continue being studied to this day and offer a promising future for devices in everyday life. This study adds to the knowledge learned about these systems in hopes of improving their functionality and usefulness in future technologies.

1.2 Hot Jet Ignition

In order for combustion events to begin, there needs to be a source of activation energy in the form of heat that exceeds the fuel-oxidizer mixture's own energy requirement with the flammability limit. This source can be many things, such as the spark from a spark plug, the compression process in a diesel engine, and more. For wave rotor combustors, the fuel-air mixture must ignite quickly for the combustion event to have enough time to burn through all the available fuel. To do this, a turbulent hot-jet is usually employed in such WRC systems due to its ability to mix chemically-active radicals quickly and turbulently with the fuel-air mixture, thus producing many potential ignition source locations for the channel. Additionally, the radicals present in the turbulent jet can overcome the slow combustion velocities found in lean fuel-air mixtures, making these jets perfect for the conditions found in the WRC channels [28].

While these jets are extremely effective and reacting with fuel-air mixtures, the actual location for the source ignition is often debated. Sadanandan et al. [29] claimed that, despite the sides of the ignition jet experiencing the most shear stresses and highest rates of mixing, the tip of the jet was where the highest amount of probability of ignition could be found. Contrary to this, however, Elhsnawi [30] studied the effects of heated inert gas being introduced to H₂-O₂ mixtures and reported that ignition is most likely to occur on the jet edge/sides. Iglesias on the other hand argued differently, finding that ignition location is dependent upon the reactant's diffusivity more so than the jet's Reynolds number [31]. For instance, hydrogen gas being a very diffusive fuel would mean that ignition was more likely to occur at the jet tip; however, less diffusive fuels would more than likely experience ignition along the jet sides.

Additionally, another crucial factor in the effectiveness of the turbulent jet turned out to be the nozzle from which the turbulent jet is emitted from. A study performed by Biswas found that supersonic nozzles reduced not only the ignition delay time but also the lean flammability limit in the fuel-air mixture. While converging and converging-diverging nozzles produce elevated temperatures ahead of the resulting shock wave, nozzles forming supersonic jets produced shock waves that increased the static temperature of the region left behind by the shock [32]. As such, both the nozzle shape and type of fuel used for hot jet ignition are factors that must be accounted for.

With all this being said, the turbulent and chemically-reactive nature of these ignition sources makes them regarded by some to be more effective than traditional spark plug ignition

methods [33]. And this is not just an academically-held stance either. Many car/internal combustion engine manufacturers have taken note of this as well and applied stationary hot jet ignition sources to various car engines over the years - including Mahle powertrain, Ford, Porsche, Volkswagen, and even a car manufacturer from 1918 [34, 35, 36, 37, 38]!

1.2.1 Hot Jet Ignition Delay Time Definition

The definition of hot jet ignition delay time can vary from the type of machine being studied to the researcher conducting the study and the kinds of limitations they may have. Broadly speaking, the ignition time delay is the amount of time it takes between two predetermined events to occur within an ignition/combustion sequence. For example, in a regular spark-ignition engine, the ignition time delay constitutes the amount of time between sparking in the engine and the first noticeable point of pressure rise. Diesel engines, however, have it defined as the time between the moment fueling ends to the moment combustion begins. And shock tubes base this value on the moment the reflected shock wave arrives to the moment ignition starts. For wave rotors, at least with regards to this study, the ignition delay time will be framed by the moment the pre-chamber nozzle diaphragm ruptures to the moment of the onset of ignition.

1.3 IUPUI Combustion & Propulsion Research Lab

1.3.1 Prior Research

The history of the Combustion and Propulsion Research Laboratory (CPRL) at Indiana University-Purdue University Indianapolis (IUPUI) is quite extensive and even begins outside of Indianapolis, Indiana. Bilgin [39] was the first student to design and experiment with what would become known as the first iteration of the current experimental setup. Located at the University of Washington in 1998, the design consisted of two pre-chambers and a premixed main combustion chamber, which allowed him to study both stationary and traversing hot jet ignition processes. Using this, Bilgin developed a way to define successful ignition based on the Damkoehler number. The high-speed camera available at the time, however, was not as fast as the one in use today, so his work was limited in the amount of detail he was able to capture. Afterward, Dr. Razi Nalim brought the experimental rig to IUPUI. Perera was the first to operate the rig in its new home, and using a faster high-speed camera and data acquisition system, he worked with various fuel-air

mixtures to study the ignition delay time in the main chamber caused by a stationary hot jet ignition source [5]. Perera also introduced a method of calculating the rupture moment of the diaphragm by measuring the pre-chamber pressure. Next, Chinnathambi studied hot jet ignition time delay with a traversing pre-chamber and found a relationship between the rotational speed of the hot jet and the ignition delay time [40]. Following this, Paik worked on implementing the schlieren photography setup that is still in use today and developed a new way to calculate ignition delay time for stationary hot jet ignition experiments using different methane-hydrogen fuel blends [41]. Then, Kojok created the third iteration of the main chamber with improved accessibility that allowed him to conduct high temperature experiments using an air heater system he implemented [7]. Additionally, he created the pre-chamber wear plate to be used for traversing hot jet ignition experiments and found that the stationary ignition delay time increased with higher equivalence ratios and pre-chamber initial pressures and lower hydrogen content/fuel reactivity. Lastly, Chowdhury continued with Kojok's work by finalizing the traversing case procedure and found that ignition time delay decreased while the pre-chamber rotation increased. Chowdhury also examined what he called spark-ignited "laminar" flame propagation in the main chamber to see if latitudinal stratification could be to blame and was the first to find evidence of this stratification within the apparatus.

1.3.2 Objectives

The objectives for this for this research work include...

1. Revive the lab and learn all of its functionalities after being dormant for around a year.
2. Design and implement a fuel-air recirculation system to reduce stratification within the main chamber.
3. Compare the effectiveness of both diffusion and recirculation mixing methods at reducing fuel-air stratification on pressure history and spark-ignited flame propagation.
4. Utilize the pump to show the recirculation system's effectiveness at minimizing buoyancy effects on ignition time delay and shock speed in stationary hot jet ignition experiments.
5. Evaluate the leakage in the traversing hot jet ignition experimental setup with and without pumping.
6. Recommend the best practices for using the new recirculation system.

7. Write an official laboratory operations manual for future students to refer back on for guidance and troubleshooting.

1.3.3 Scope of Present Research

This research work primarily focuses on reducing fuel-air stratification on hydrocarbon combustion and ignition delay time by developing new experimental procedures for a constant-volume combustion system. This serves as a continuation of all the previous CPRL researchers' work, especially that of Chowdhury. In his study [42], Chowdhury noticed large variations in his results, indicating that the fuel-air mixture inside the main chamber might not be fully mixed. While Chowdhury focused largely on traversing cases, the work in this thesis primarily looked at stationary hot jet ignition and spark-ignited flame experiments, along with some leak testing analysis. Chowdhury also only utilized diffusion as a means for fuel-air mixing during the last set of his experiments, but for this study, a new recirculation pump was implemented into the experimental rig. In order to see how it handled mixing, fuels of various densities were utilized. These included pure methane, hydrogen, and propane; additionally, 50%-50% methane-hydrogen and 46.4%-53.6% methane-argon blends were used, with the methane-argon blend only being utilized for spark-ignited flame propagation experiments. For all fuels in the stationary jet and spark-ignited flame tests, the equivalence ratios were set to 0.4, 0.7, 1.0, and 1.3 inside the main chamber while the temperature and pressure were left at room conditions. The pre-chamber, however, was held at a 1.1 equivalence ratio of 50%-50% methane-hydrogen at atmospheric pressure and temperature. Additionally, test cases utilized either the new recirculation pump or diffusion effects between the fuel and air for mixing. In spark-ignited flame cases, the pump was used for 10 and 30s in some trials while diffusive mixing was allowed to take place for 0, 10, and 30s in others. For stationary cases, on the other hand, only 0s non-pumping cases and 30s pumping cases were considered; similarly, the leak tests only evaluated cases with both no pumping and 15s of pumping.

By the time research began, the lab had been sitting for over a year without use, so learning about the system and how it works was crucial. The spark-ignited flame cases primarily helped in determining how effective the pump can be in minimizing stratification in the main chamber, while the stationary cases focused on further seeing if stratification was a factor in ignition time delay results and if the pump remained effective in cases where turbulent mixing was inherently part of

the experiment. For the leak analysis experiments, no combustion occurred, but the main chamber and pre-chamber were still coupled together and fueled as though traversing cases were being conducted. This was done in order to see how the additional pumping mechanism affected the overall leakage rate on the system. Schlieren and flame luminosity footage was used to analyze the flame propagation across all of the experiments for visual evidence of buoyancy phenomena. Additionally, pressure history profiles and maximum pressures were used to see how different mixing techniques not only affected the time ignition delay but also the performance of combustion within the main chamber. Ultimately, this study provided this and other PGC labs with the necessary concepts and tools needed for future researchers to be successful and know how to effectively reduce stratification effects and make the system overall a more representative model of a WRC.

2. EXPERIMENTAL SETUP

The experimental apparatus used for this work can currently be found in the CPRL at IUPUI. The device was initially designed by the late professor Jakob J. Keller as a way to model the combustion phenomena occurring within each wave rotor combustor channel, and with the help of the NASA Lewis Research Center, it was carefully built at the University of Washington by Dr. M. Bilgin [39]. The apparatus itself was segmented into two main parts: a rectangular main chamber and a cylindrical pre-chamber. This allows for simplification of the wave rotor geometry while still accounting for rotational effects by way of rotating the pre-chamber and modeling the single channel's combustion behavior within the main chamber. After moving these pieces to IUPUI, CPRL graduate students have worked tirelessly on the apparatus over the years, with several redesigning it in order to improve various shortcomings.

Now on its third iteration, the equipment has gone through even more small additions in order to improve its performance. Designed by Kojok [7], design minimized heat loss, simplified opening/sealing of the main chamber, enhanced schlieren visibility, and added new fueling capabilities. In addition, Chowdhury [42] provided necessary tweaks to the system, such as creating new main chamber seal plates, optimizing the fuel delivery system, and expanding fuel port uses. These improvements alone have made significant benefits. The new seal plates and sealing design have effectively reduced leakage from the apparatus; the mass flow controller-driven fueling system allows for more exact experimentation and repeatability between experiments; and the fuel port additions have increased the range of use beyond what was previously possible (e.g. new fuels, better cleaning, and improved safety). One of the issues that was still not addressed, however, was that stratification between the fuel and air inside the apparatus was not being taken into account. In order to correct for this, a new pump-driven distribution system was designed in order to be incorporated into the existing fuel line piping that Chowdhury had added on previously. The new manual pump feature consisted of a bulb-style siphon pump connected to rubber tubing on both ends that can allow for two different flow directions and, subsequently, new mixing opportunities between the fuel-air mixtures in the chamber. Additionally, the author added necessary ports and valves to the existing pipe fittings for the pump system. Ultimately, this increased the functionality of apparatus and gave the user more control over what conditions they want to control. A table featuring the apparatus' dimensions can be seen below in Table 2.1.

Table 2.1. Main Chamber and Pre-Chamber Dimensions.

Name	Value
<i>Main Chamber</i>	
Length X Width X Height	16.25 X 4.43 X 4.99 in ³
Channel Cross-Sectional Dimensions	1.43 X 1.84 in
Aspect Ratio	0.77
Length to Hydraulic Diameter	8.69 in
Combustion Volume (without Pump)	45.47 in ³
Combustion Volume (with Pump)	59.15 in ³
XY Table Linear Resolution	2 mm/rev
Viewing Window Dimension	14 X 1.85 in
PT2 Distance (from Chamber Front Edge)	1.50 in
PT3 Distance (from PT2)	10.22 in
PT4 Distance (from Chamber Rear Edge)	1.75 in
Air Inlet Distance (from Chamber Rear Edge)	4 in
Air Outlet Distance (from Chamber Front Edge)	1.5 in
Fueling Port Distance (from Chamber Front Edge)	5 in
Wear Plate Thickness (A2 Tool Steel)	0.5 in
Seal Plate Thickness (Steel/Bronze)	0.25 in
<i>Pre-Chamber</i>	
Internal Diameter	6.52 in
Width (without Wear Plate)	1.54 in
Converging Nozzle Throat Diameter	0.27 in
Diaphragm Thickness	0.003 in
Diaphragm to Nozzle Outlet Distance	1 in
Nozzle L/D Ratio	3.73
Combustion Volume	49.3 in ³
Combustion Volume Ratio	1.14

2.1 Laboratory Facility

The CPRL resides on the first floor of the Engineering & Technology (ET) Building at IUPUI, located in room ET 109. The room is split into two separate sections, with a wall and door entry dividing the two. In the first half of the room, a bank of computers is used for computational fluids and combustion research; lining the wall is a row of windows looking into the second half of the facility as well as a gray control box that is meant for remote control of the experimental devices. The second portion of the lab (named ET 109a) exclusively houses the experimental equipment – including the apparatus itself, a motor controller, fuel cylinders, compressed air lines, hardware pieces, cleaning supplies, electronic components, and archived equipment. Figure 2.1 depicts ET 109a in a simplified form, showcasing all the instrumentation and systems involved in experiments with the wave rotor model apparatus.

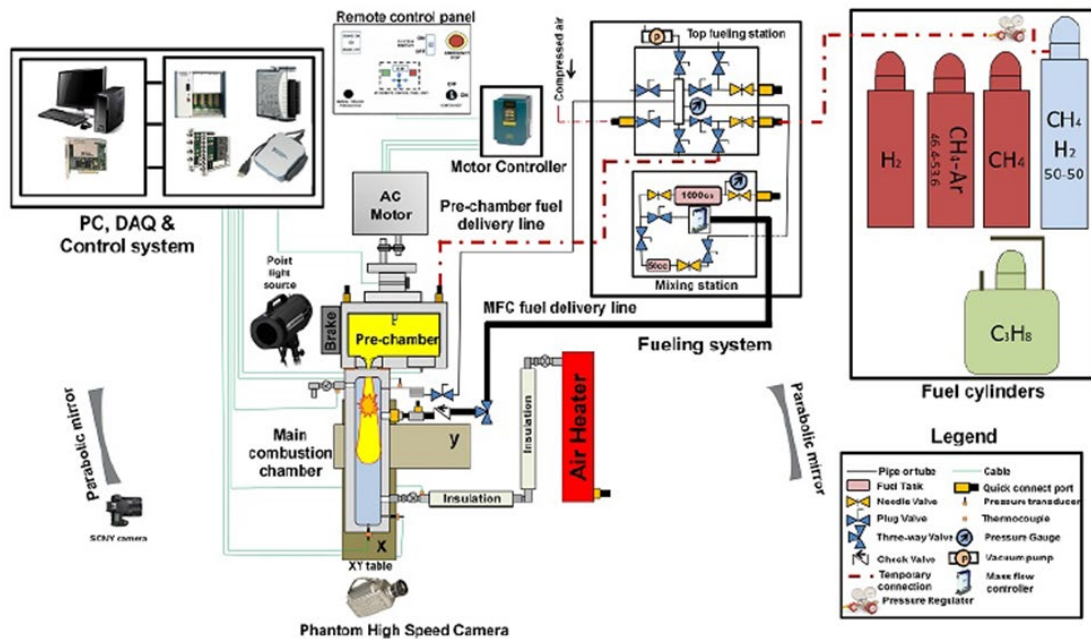


Figure 2.1. Schematic Diagram of ET 109a with views of the apparatus and all fueling and data acquisition subsystems [42].

2.2 Main Chamber

The main chamber is the fixed rectangular combustion chamber portion of the wave rotor experimental rig. It is comprised of 3 pieces made up of 304 stainless steel: a middle piece that holds all of the port openings for the main chamber and two side pieces each containing a rectangular TSC-3 clear fused quartz glass block in the center for schlieren visibility. In order to

create a seal, an O-ring is placed at each metal-to-glass contact area (four in all); additionally, a Buna-N/Aramide gasket is positioned in-between the side and middle pieces on both sides. Eight holes are present through the width of all three chamber pieces, and once lined up, a rod featuring a threaded end can be placed through each one and torqued with a nut up to 250 in-lbs. Due to its relative simplicity, this also makes cleaning the chamber a much easier process, as laid out by Kojok in his work [7]; this is an important step since combustion products and dried water vapor can lead to diminished visibility through the glass and impurities left behind can potentially affect results. Overall, these attributes culminate to a design that minimizes heat loss during high temperature experiments and reduces leakage of fuel-air mixtures from the system.

Other features of the chamber can be found along the outside of the chamber. The “front” – the side facing the pre-chamber – has four screw holes in its face that allow for various seal plates to be secured to it (see Sect. 2.4 for details). And the “back” has four more screw holes of a bigger size that allow for aluminum profile bars to be fastened to the chamber, which function as both a bracing method when sealing the two chambers together as well as a mount for the new pump distribution system. Also, six ports are present along the top and bottom of the chamber for the purposes of functionality and data measurement. Three of the six ports act as fueling and air ports for the system. The top middle port is connected to the fuel delivery system and also supports a quick connect port that can be connected to a vacuum pump. The top back and bottom front ports are connected to a compressed air line and the surrounding air, respectively, to allow thorough purging of the system between experiments; both of these ports also connect to the pump system for ease in circulating fuel and air in the chamber. These features can be seen visually in Fig. 2.2 below with corresponding labels.

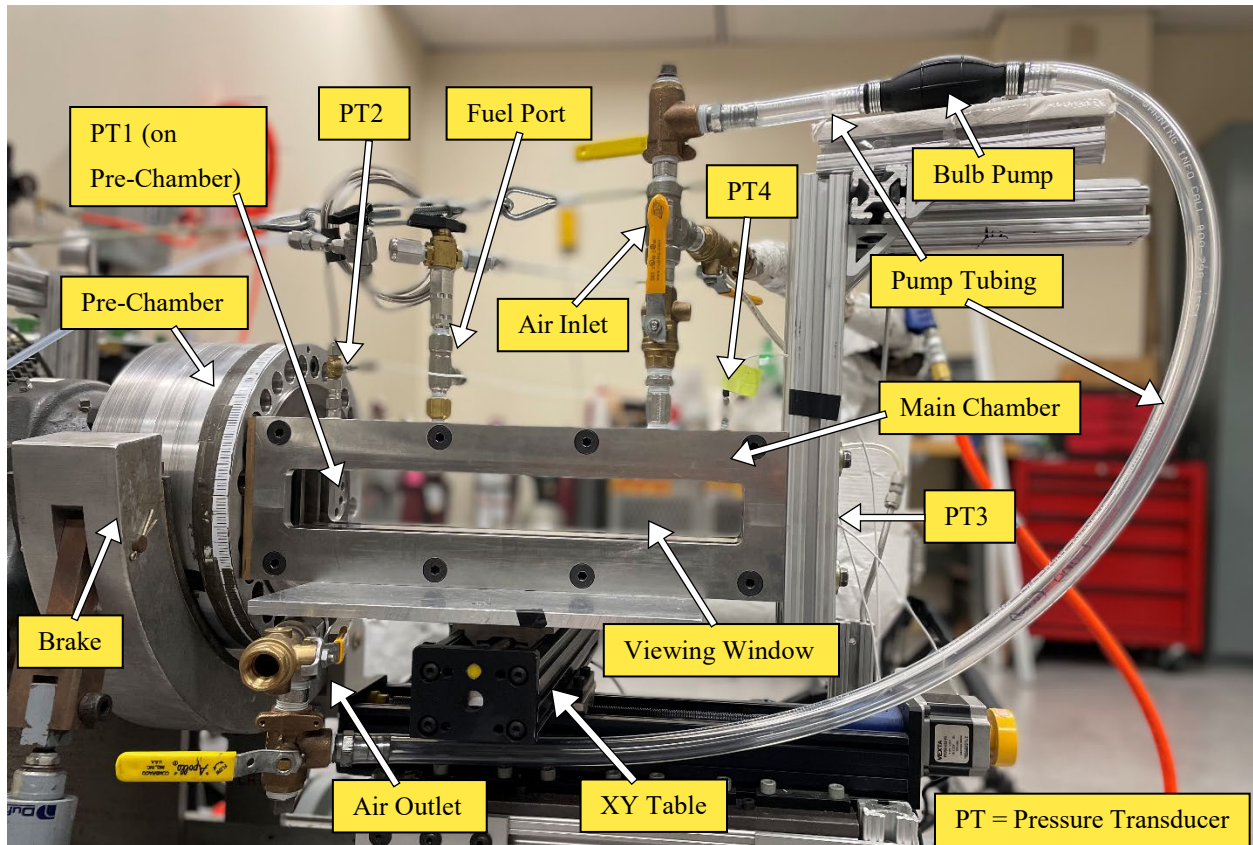


Figure 2.2. This picture shows a side profile view of the main chamber and its corresponding labels.

2.2.1 XY Table

In order to position the main chamber for various experiments, the chamber is affixed on top of a Velmex XY positioning table (model MN10-0100-M02-13). This table is made up of two lead screw slides that are connected to stepper motors, and a control box below the rig electrically controls the direction of movement of the chamber. Additionally, the portion of the table responsible for putting the chambers closer to or further apart from one another (denoted as the X-slide in previous works) can be fine-tuned using a yellow circular knob below the main chamber's back end. For spark-ignited flame tests, the XY table can act as a way to move different portions of the chamber in and out of the schlieren visualization region. However, for hot jet ignition related experiments, the table functions more as a precise method of coupling and sealing the main chamber and pre-chamber together as well as a quick means for decoupling them in order to purge the system between test cases.

2.2.2 Recirculation Pump System

A new addition to the main chamber is a manual pump circulation system comprised of PVC tubing and a fuel primer pump. Metal pipe fittings on the top and bottom air vent ports were extended to allow a 3-way directional-control valve at both ports, which only allows flow from the middle opening to either the top or bottom valve opening depending on the position of the handle. For both valves: one opening was connected to the newly-added pipe fittings; the middle opening was fitted with a barbed hose fitting; and the exposed opening was capped with a metal plug. Clear PVC tubing was cut to length, with a short tube connected to the top port and a much longer tube connected to the bottom. A 42mm diameter rubber primer bulb pump connected the two portions of tubing, and hose clamps secured all of the tubing.

The pump features two 12mm bard hose ports on both sides of the bulb, and inside each port is a one-way valve that allows flow to move in only one direction through the pump. Upon compression of the bulb, the fluid inside is push out the exhaust port until compression stops; once one relaxes the bulb, the inlet port begins drawing fluid back into the bulb, ready to be sent out the exhaust port once compressed again. Due to the design of the pump system, the pump can be flipped from one flow direction orientation to the other by simply disconnected from the tubing and reassembling once rotated. This means the user can either draw fuel-air mixture from the top-back port of the main chamber and send it to the bottom-front port (Top-to-Bottom orientation, or T2B) or vice versa (Bottom-to-Top orientation, or B2T).

2.3 Pre-Chamber

The pre-chamber is a hollow, stainless steel, cylindrical combustion chamber that is often pressed up against the main combustion chamber during experiments in the CPRL. Its purpose is to be an ignition source for the main chamber by streaming a jet of chemically-active combustion product radicals through a converging nozzle as well as account for the rotational effects experienced by normal WRCs. The pre-chamber itself is made up of four separate parts: a wear plate, front plate, intermediate ring, and rear plate. The wear plate was designed by Kojok and made from A2 tool steel that had been surface finished to 16microns of average surface roughness [7]. The smooth surface was a necessary component of getting the pre-chamber to seal well against the oil-impregnated bronze main chamber seal plate employed by Chowdhury in his traversing HJI

experiments [42]. The wear plate is mounted to the front plate, which is affixed to the intermediate ring – all of which comes off of the rear plate that stays bolted to the motor drive shaft. The rear plate serves several functions, in fact, for it not only attaches the remainder of the pre-chamber to the motor shaft but also features two quick connect fueling ports on its backside and a Champion RC11ZYC4 spark plug ignitor at its center, all of which is visible in Fig. 2.3. The fueling ports allow for quick fueling of the pre-chamber on either side, so long as the fueling occurs on the opposite side from the nozzle insert. Additionally, the spark plug acts as the ignition source for the combustion event within the pre-chamber during experimentation. All of the pre-chamber parts have circular holes lining the perimeter of the chamber that act as potential clamping points to hold the chamber together. Six long bolts are inserted in equidistant points located along this ring and are subsequently tightened with washers and bolts in a star pattern using 250in-lbs of torque. Paik once estimated that the nominal pre-chamber volume was around 51.27in³ [41], but taking into account the space occupied by all of the bolts holding everything together, Kojok lowered this estimate to around 49.3 in³ [7]. While there is not often a need to take this chamber apart, it is good to do so every so often to clean out any lingering combustion products that may affect results.

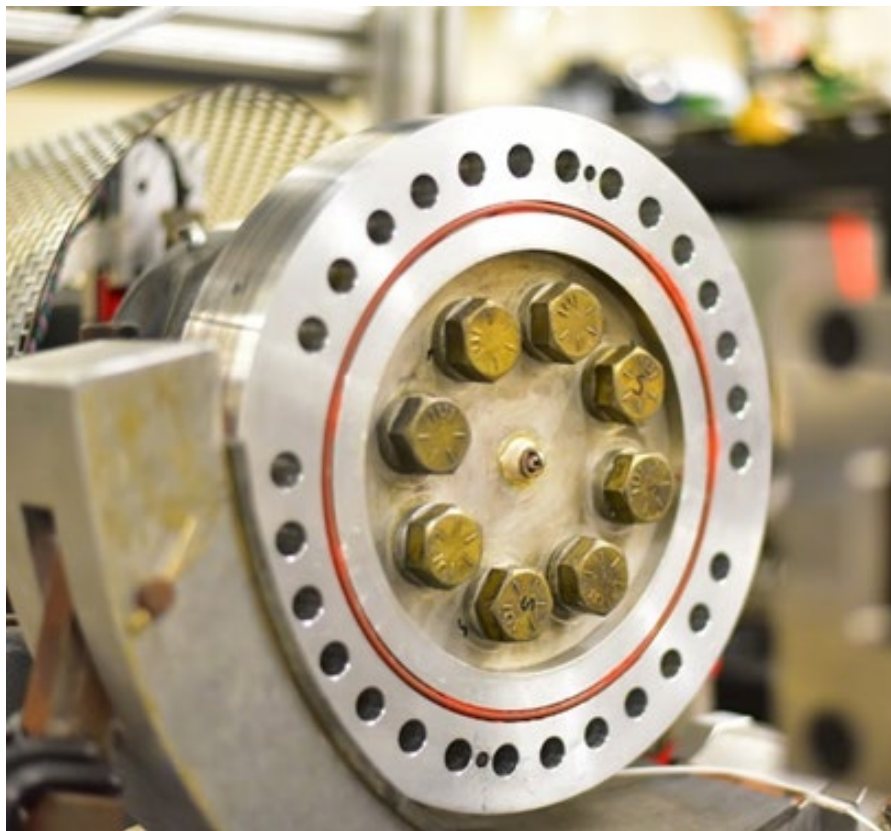


Figure 2.3. Picture showing the inside of the pre-chamber [42].

Another feature of the pre-chamber is the two symmetrically-located, cylindrical cavities in the face of the pre-chamber; these are meant to house nozzle inserts that can be removed and interchanged depending on the experiment. These cavities are purposefully kept in symmetric locations so as to promote equal balancing while the pre-chamber rotates at high velocities, with Ferrara's work going into great detail about these cavities' locations [5]. One of the three inserts for these cavities is the converging nozzle that was mentioned previously. Another insert, however, does not have a nozzle; instead, there is a pressure transducer (labeled as PT1) embedded in the center of the insert. After screwing it into one of the cavities, the PT1 wire is plugged into the transducer jack, and the computer is able to receive pre-chamber pressure data. This insert is only used during stationary jet experiments, and the pressure data collected at this position during combustion events is reasoned to be the same as the pressures experienced at the diaphragm-nozzle assembly due to the symmetric nature of their locations. Lastly, the third insert is a simple solid blank insert meant for use in traversing HJI experiments. Because the pre-chamber is rotating during these experiments, the PT1 external port would be severely damaged from high velocity impacts with the main chamber. Further, the cable would become very twisted and probably tear off during the rotation as well. As such, pressure data cannot currently be collected during traversing cases, but the solid insert is still necessary to switch out with the PT insert so that balance in the pre-chamber is maintained.

2.3.1 Nozzle Insert

The nozzle used for the current study was developed by Arshad for the purpose of fitting Kojok's newly designed pre-chamber. Previous students of the CPRL facility have designed a multitude of different nozzle configurations over the years; however, Perera found that a convergent nozzle with a 0.27in exit diameter, 10-degree taper, and 1in distance between nozzle diaphragm and exit produced the smallest ignition delay times out of all the nozzles previously studied [5]. Since his pre-chamber featured a thicker design due to a front wear plate, Kojok adapted this nozzle design to sit flush with the pre-chamber surface and drag evenly across the oil-impregnated bronze seal plates used in his traversing hot jet ignition experiments [7]. Kojok's nozzle features a clamping disk, aluminum diaphragm, and nozzle insert base, as depicted in Fig. 2.4a. The nozzle base houses a large O-ring to create a seal against the pre-chamber when fully inserted, and both sides of the aluminum diaphragm are pressed against smaller O-rings embedded

in the nozzle base and clamping disk. In order to work properly, though, the nozzle must be oriented so that the large space between the screw holes is oriented vertically, as highlighted by the pencil outline on the nozzle face in Fig. 2.4b.

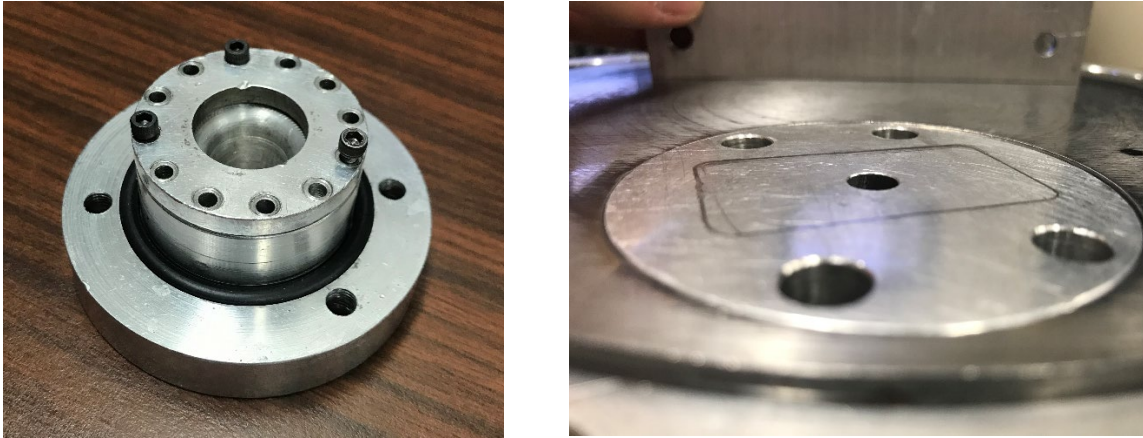


Figure 2.4. Two side of the nozzle insert: a.) this is the backside of the nozzle that is inserted into the pre-chamber, and b.) this shows the front face of the nozzle with a pencil line showing where the main chamber opening lies in relation to the nozzle.

2.3.2 Diaphragm

The aluminum diaphragm is a key component in the nozzle insert assembly used for stationary and traversing jet experiments. Once set in the nozzle and sealed by O-rings on both sides, the diaphragm effectively seals off the internal pre-chamber volume from the surroundings. This allows for controlled fueling of the pre-chamber and, consequently, gives the pre-chamber the ability to be primed to a different equivalence ratio than that found in the main chamber. The diaphragm itself is a 0.003in thick, 40mm diameter circular piece of aluminum that has been scored with a Score1 50050 glass cutter. The glass cutter has been modified in such a way that a gliding metal plate slides underneath the scoring wheel; therefore, pushing the plate back and forth completes two passes under the scorer. To score a disk, one is laid down on the metal plate, and a line is imprinted into it using two passes under the wheel. The disk is then rotated 90-degrees and another line is made, thus resulting in a “+”-shape in the disk. The scoring process ensures that the aluminum disk actually bursts after a maximum internal pressure is reached due to the combustion of pre-chamber fuel. In a valid test, all 4 petals of the disk must burst; otherwise, asymmetrical bursting can cause a non-uniform flow through the nozzle.

Other alternatives to this diaphragm method have been utilized over time, but they presented significant problems in their implementation. Most notably, a latex barrier once sealed the main chamber in a similar fashion, with the heat from the resulting jet being the cause for the latex to burst. However, the heat would inadvertently cause the latex to burn at the same time, which introduced unintended chemical radicals in the ensuing pre-chamber jet. Thus, this method was not an effective means of sealing, and so the diaphragm method was adopted instead. Similarly, though, bits of diaphragm debris resulting from the sudden busting of the aluminum is sometimes visible in videos of the experiments. It was once thought by previous CPRL researchers that cases in which this occurred needed to be thrown out due to also introducing unintended radicals into the main chamber system. After further analysis, though, it was determined that this assessment was not that case and that this phenomena was instead a natural part of fuel-rich premixed combustion, and thus, these cases have also been included this investigation.

2.4 Seal Plates and Leak Management

Several seal plates are available for use on the main chamber but are selected for use based on the type of experiment being performed. Each plate goes about preventing leaks in different ways, and the following subsections will review each kind of plate and how leakage from the main chamber as a whole is prevented as much as possible. All seal plates are roughly 4.43in by 5in with four 0.25in diameter holes meant for the seal plate screws positioned near the corners, and the two jet ignition seal plates feature a small, rounded rectangular window in the center that measures around 1.75in by 1in.

2.4.1 Spark Plug Seal Plate

Spark-ignited flame experiments only involve the main chamber for experimentation. The other seal plates attempt to act as an intermediary by creating a seal between themselves and the main chamber and pre-chamber, but the spark ignition seal plate only needs to effectively seal the main chamber. To that end, the design of the spark plug seal plate is quite simple: a 0.375in thick piece of aluminum cut to size with a 14mm diameter screw hole at its center. A Champion model FI21501 spark plug is situated in the center while a liquid gasket material prevents leaks from the spark plug. This model of spark plug was chosen due to its long stem being able to reach the optical

window portion of the main chamber and thus being visible for schlieren analysis. On the opposite side, a 0.14in thick O-ring is set into the plate in a 1.75in by 1in outline, ensuring that the main chamber channel opening is sealed as well. Figure 2.5 showcases the seal plate and accompanying Champion spark plug below.

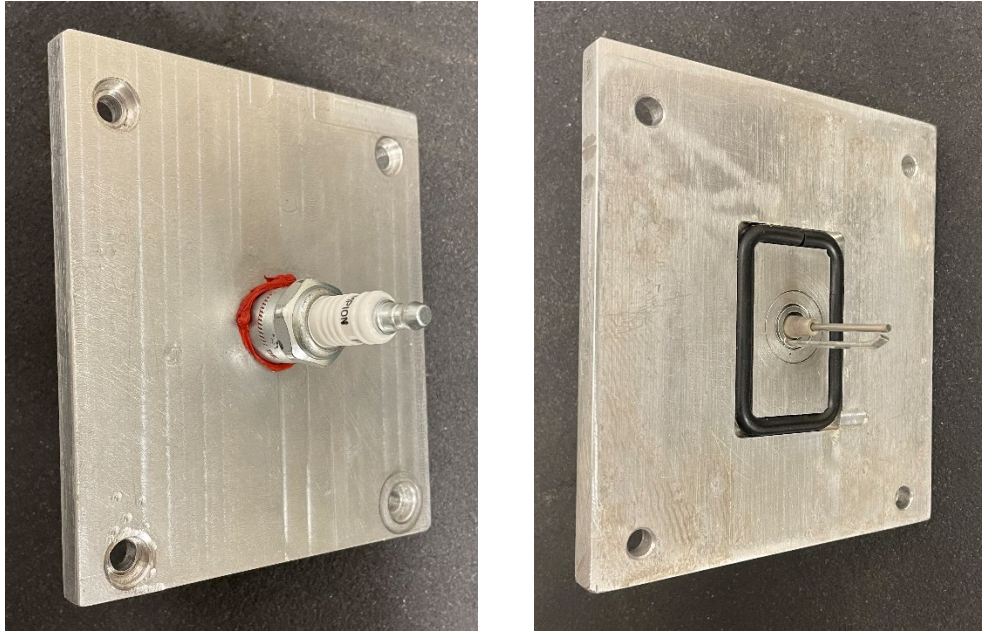


Figure 2.5. The spark plug seal plate with mounted Champion FI21501 spark plug viewed from the a.) front and b.) back of the plate.

2.4.2 O-Ring Seal Plate

This aluminum seal plate is the most conventional seal plate configuration compared to the others in this work, as it features O-rings on both sides of the central rectangular window cutout (see Fig. 2.6). Since O-rings work best under static conditions, this seal plate is only used for stationary hot jet ignition experiments. Once affixed to the main chamber's front face, the chamber can then be pushed up against and clamped to the pre-chamber nozzle face, causing both O-rings to be squished into a secure seal on both sides.

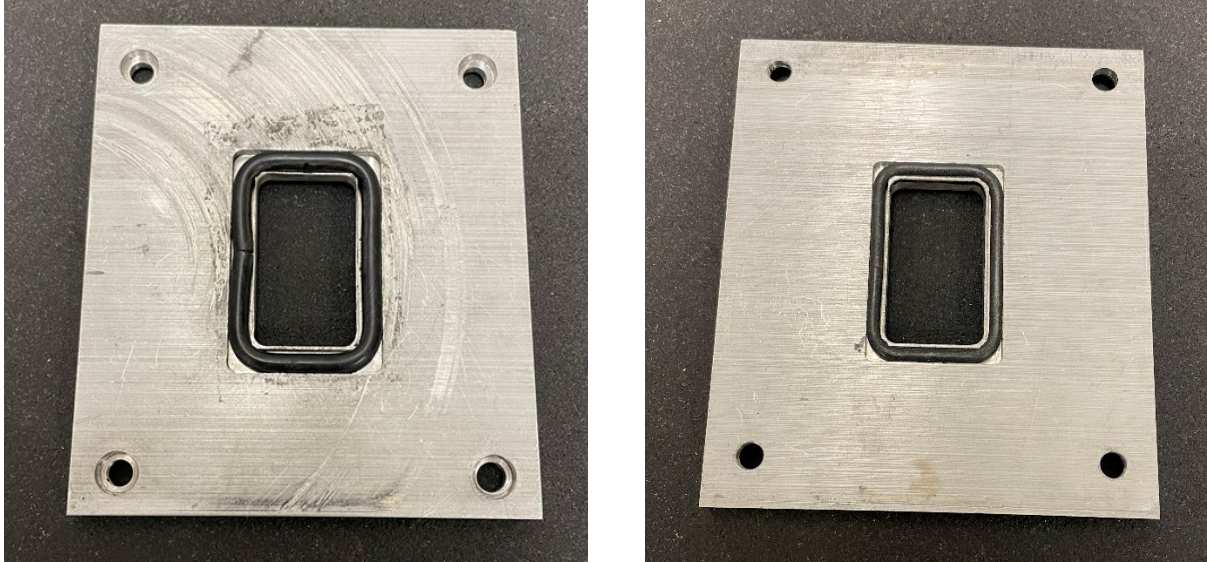


Figure 2.6. The O-ring seal plate used in stationary hot jet experiments viewed from the a.) front and b.) back.

2.4.3 Oil-Impregnated Bronze Seal Plate

Due to the increased temperatures from high amounts of friction experienced during traversing cases, traditional O-ring style sealing methods are not feasible for rotating hot jet ignition tests since the O-rings can become stretched and damaged through continued use [40]. As such, Chowdhury developed a new seal plate specifically for traversing experiments that took advantage of the friction between the seal plate and Kojok's pre-chamber wear plate. Since bronze has a much lower coefficient of friction between it and steel compared with other materials, Chowdhury employed an oil-impregnated bronze plate for use as a seal plate. When the friction between the bronze and pre-chamber face heats up the bronze plate, the increased temperature causes the oil to expand and emerge from the bronze. Thus, the seal plate becomes a lubricated surface, creating a dynamic seal between the pre-chamber and bronze surfaces. On the flip side, a rectangular-shaped O-ring forms a seal between the plate and the main chamber face. Photos of this seal plate are visible in Fig. 2.7 below.

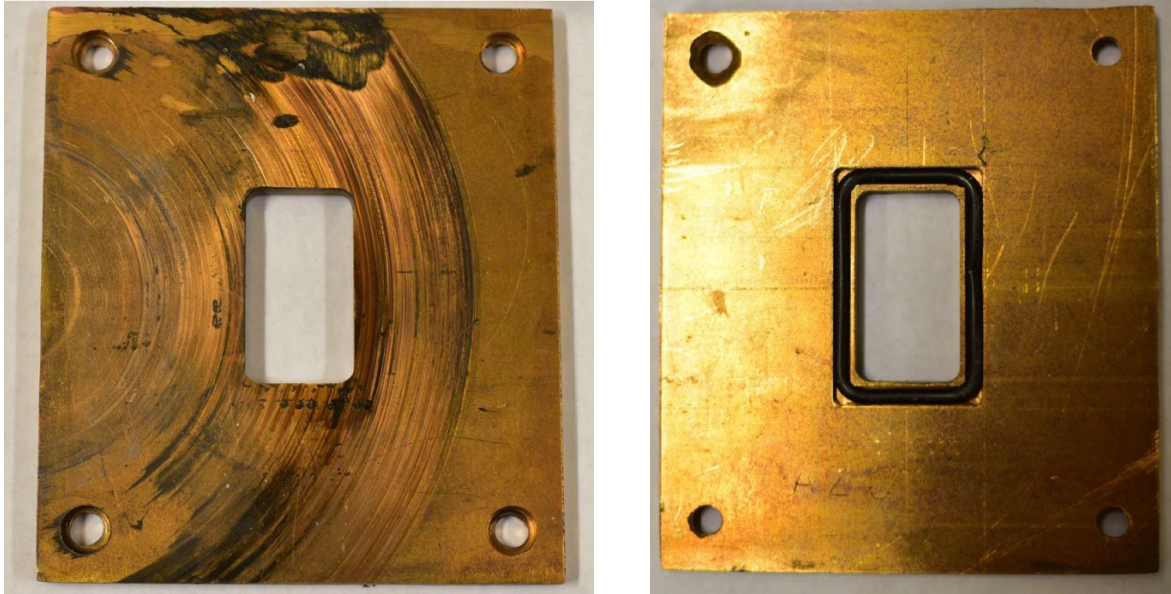


Figure 2.7. The oil-impregnated bronze plate used in traversing hot jet experiments viewed from the a.) front and b.) back.

2.4.4 Leakage Gap

The leakage gap for this system refers to the space between the seal plate and pre-chamber surface when conducting traversing hot jet cases. In these cases, since there is no O-ring present and the seal is reliant on the oil emerging from the bronze plate (which is in turn dependent on the friction generated between the seal plate and pre-chamber face), the leakage rate is much higher than the other test cases. Therefore, this gap is an important factor during such experiments and must be closely monitored during each test. For instance, if the gap is too small, then the leakage rate will decrease; however, the friction will be so high that the motor cannot maintain a steady pre-chamber rotational speed and the heat energy will affect the incoming radical jet entering the main chamber. And if the gap is too big, then the leakage rate will increase, and both the radical jet and main chamber fuel-air mixture will partially release out to the surroundings and cause unreliable data.

In order to effectively control the leakage gap in a reliable fashion, the pre-chamber speed is monitored while coupling the two chambers together. Using an Extech tachometer while the pre-chamber is rotating, the X-slide of the XY table is used to push the main chamber toward the pre-chamber by manually turning the external lead screw wheel and watching the rotational speed decrease until a desired lower speed is reached – typically no more than 2% less than the initial

pre-chamber decoupled speed. To aid in the coupling process and in maintaining this contact force, a flexible rope clamp is also employed as another method of adjusting the force between the two systems (Fig. 2.8a). This is much like the stationary cases, in which a large C-clamp is used as a backup method to press the two chambers together and form a tight seal with the O-rings embedded in the O-ring seal plate (Fig. 2.8b). Despite this reliable method of maintaining the leakage gap, however, the leak rate during traversing experiments is still quite extensive, with this problem being examined later in this study in Sect. 3.3.

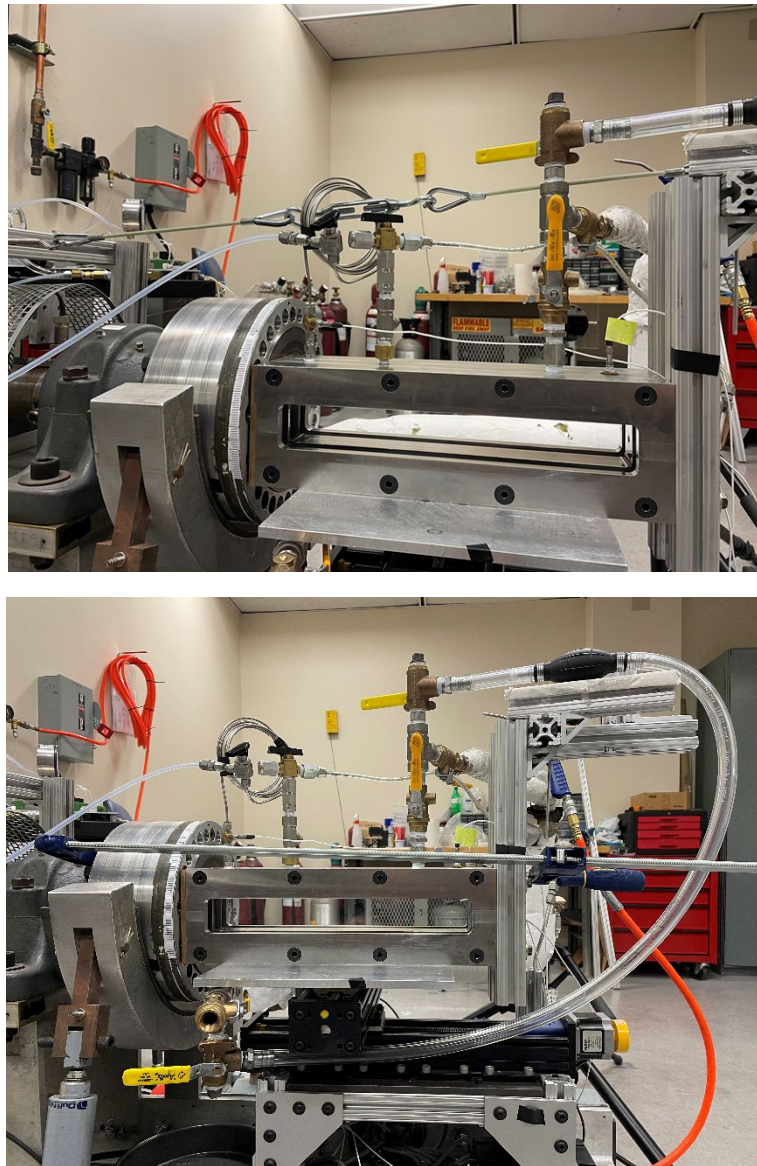


Figure 2.8. The a.) flexible rope clamp employed during traversing jet experiments and b.) c-clamp used for stationary jet experiments help maintain a consistent clamping force between the main chamber and pre-chamber.

2.5 Fueling System

Two different methods of fueling are utilized in the CPRL: a partial pressure method and a mass flow controller method. These techniques have been developed and refined over the years through the work of previous graduate students. While Paik, Perera, and Chinnathambi manually fueled both combustion chambers in the system using the partial pressure method [41, 5, 40], Kojok installed a device known as a mass flow controller in order to electronically add fuel to the main chamber. Other minor differences between these authors have also been honed over time. For example, each researcher had slight variations in how their fueling processes were done; some added air to the system upon fueling to help with mixing, and others would add pure fuel mixture components individually instead of as a pre-blended mixture. Additionally, of the students would manually make methane-hydrogen fuel mixtures in batch quantities for use in the system, Chowdhury, on the other hand, used a premixed gas cylinder of this same fuel blend to ensure consistency [42]. Furthermore, the author of this research took this a step further by not making batch fuel mixes of any kind and using already-available premixed gas cylinders, instead.

In particular, five specific fuels were used for experiments in this work; these include pure hydrogen, methane, and propane as well as 50%-50% methane-hydrogen and 46.4%-53.6% methane-argon blends. All of the fuels are supplied by Praxair except for propane, which is filled by Blue Rhino, and specifications for each fuel can be found in Chowdhury's work [42]. While creating batch mixtures in-house reduced the number of gas tanks needed in the lab, it also caused variations in the fuel between batches, which meant that specific air-fuel ratios were difficult both to achieve and to maintain when performing a range of experiments. In this way, switching to premixed gas tanks has helped keep experiments more consistent and data more reliable, especially in the pre-chamber which contains a 50%-50% methane-hydrogen fuel and air mixture during experiments. On top of this, the mass flow controller system delivers a consistent amount of fuel to the main chamber every single time, thus improving its fueling reliability and repeatability across experiments. As previously done by both Kojok and Chowdhury, though, fueling calibrations are necessary in order to maintain reliable performance with the system, and this will be discussed further in Sect. 2.5.2. For those interested in reading the exact details on the procedures and calculations involved in the fueling operations, readers are encouraged to read Kojok's and Chowdhury's research works [7, 42] while others may read a brief overview of these ideas in the following subsections.

2.5.1 Pre-Chamber Fueling

As described before, the pre-chamber is a well-constructed unit of the experimental apparatus, and with the help of several internal O-rings, it's been estimated that the pre-chamber leakage is only around 0.0001 psi/min when vacuumed to a pressure of -10psig [42]. Because of this tight seal, one of the most effective ways to fuel it is through the partial pressure method. To find out how much gas must be put into the chamber, an equation (Eqn. 2.1) is developed through the application of the ideal gas law, Dalton's law of partial pressure, and the chemical equation of the combustion reaction between methane-hydrogen and air and denoted below:

$$P_{total} = P_{initial} + \frac{2\phi}{2\phi + (4.76*2.5)} \quad (2.1)$$

Here, $P_{initial}$ is the air pressure before fuel is added; P_{total} is the pressure after fueling; and ϕ is the equivalence ratio the chamber is being fueled to. In order to create a stable system and help prevent leaks while the pre-chamber waits to be ignited, it's best to keep the end pressure of the system around the same as the ambient pressure in the lab room. This means that the pre-chamber must first be vacuumed out slightly before any fuel is added. For the purposes of this work, the pre-chamber was only ever set to an equivalence ratio of 1.1, and knowing this as well as the desired P_{total} , $P_{initial}$ can be solved in order to find out how much air needs to be vacuumed out of the pre-chamber.

After finding this out, the fueling of the system itself is quite easy given the simple construction. First, the methane-hydrogen gas cylinder regulator is tapped directly into a fueling station that is off to the side of the apparatus – which has access to quick connect hoses, mixing tanks, a vacuum pump, and a compressed air line (more details can be found at [7]). From there, a quick connect hose is connected to the fuel port on the back of the pre-chamber opposite from the screwed-in nozzle assembly. With an ASHCROFT VAC 30psig pressure gauge located on the fueling station monitoring the internal pressure of the chamber, the ports on the fueling station are opened to the vacuum pump, and the calculated amount of air is drawn out of the system before it is closed once again. Next, the fuel is streamed into the pre-chamber with the help of a needle valve, and while it fills up, the pressure gauge ensures that the atmospheric pressure is not missed. The fuel line is disconnected at this point, and the pre-chamber is ready for the main chamber to fill up and for the combustion to occur.

2.5.2 Main Chamber Fueling

The main chamber features a port on the top of its casing that allows for fuel to enter the chamber; however, unlike the pre-chamber, the main chamber's leak rate is higher. This means that the partial pressure method for fueling is not as viable and that a faster technique is required, especially for traversing cases. To account for this, an MKS PFC-60 mass flow controller is incorporated into the fueling station and connected to the main chamber fuel port. With this device, fueling is achieved quickly and more reliably than with the partial pressure method, and since it is pressure-insensitive, changes in the pressure of the main chamber and fuel supply lines will not affect the MFC's constant flow rate. Kojok describes the theory and implementation of this system in great detail [7], but at a glance, the MFC operates using a simple closed feedback loop between a flow rate sensor and control valve. The flow rate sensor is comprised of a resistive heated winding that measures the temperatures of the upstream and downstream flows, and since temperature and mass flow rate are proportional, the flow through the system is able to be constantly monitored and maintained at a steady rate no matter the surrounding conditions. The solenoid control valve is responsible for how long flow is allowed through the MFC and is controlled by a voltage pulse, staying open as long as it receives the pulse from user. An important note to make, however, is that the MFC takes 1.5s in order to get up to a constant flow rate and 2-3s to settle at that rate; this 3s is known as the rise time of the MFC. Once fueled though, the MFC measures and reports flow in units of standard cubic centimeters per minute (SCCM) and can maintain a maximum flow rate of 1000 SCCM if need be. After the valve is closed, the MFC produces a raw voltage value that is multiplied by a fuel-specific SCCM/V calibration factor within LabVIEW to show the amount of fuel actually delivered by the system. This can then be used to calculate the actual equivalence ratio within the main chamber at the time of ignition.

Fueling the main chamber is more simple and easy than the pre-chamber, as the system is automated and a part of the equipment control system. First, the user must connect the fuel regulator line to the top half of the fueling station, and from here, the fuel supply can be brought down to the bottom half of the fuel station where the MFC presides by one of two ways. One way is by directly connecting the top fuel station hose to the quick connect port at the base of the MFC, and the other way is to fill the 1000cm³ storage tank upstream from the MFC. Then, an excel table calculator designed by Chowdhury [42] is pulled up, and the room pressure and temperature as

well as the main chamber volume are used to find the mass of fuel needed to reach a specific equivalence ratio in the given conditions. This is calculated by Eqn. 2.2 below

$$m_{fuel} = \frac{P_{air} * V_{main} * M_{air} * \Phi}{R * T_{air} * (A/F)_{stoichiometric}} \quad (2.2)$$

Where m_{fuel} is the desired amount of fuel mass, P_{air} is the ambient room air pressure, V_{main} is the main chamber volume, M_{air} is the molecular weight of air, Φ is the desired equivalence ratio, R is the gas constant, T_{air} is the room air temperature, and $(A/F)_{stoichiometric}$ is the stoichiometric air-to-fuel ratio for the fuel being used. This result is then carried on to find the amount of time needed to keep the MFC open through the equation

$$t = m_{fuel} / k \quad (2.3)$$

Here, k is another fuel-specific calibration constant found during calibration tests that relates the amount of fuel delivered by the MFC to the number of seconds the MFC is kept open. This time (t) is then converted to a duty cycle percentage by dividing t by the set point signal on time (t_{set}) used by the system. This number is then given to LabVIEW control software, and once all other settings are supplied, the program is initiated and fuels the chamber accordingly.

Because this fueling system is able to be pressure insensitive and adjust itself in order to maintain a constant flow rate, the fueling itself is an unsteady process, and therefore, it needs validation through calibration tests in order to ensure its operation and that the correct amount of fuel is being delivered. This is done through a volume displacement method detailed by Kojok [7], but in short, a fuel line from the MFC is fed through the top of a glass burette while the two pieces are held upside down in a cylindrical acrylic container (much like a graduated cylinder) filled with water (see Fig 2.10 for a visual). As fuel dispenses from the MFC and gets fed through the tube, the burette holds onto the gas and pushes the water down and out of the burette. Thus, by knowing the water line before and after fueling, the actual amount of fuel delivered by the system can be determined and compared against the MFC reported fuel amount.

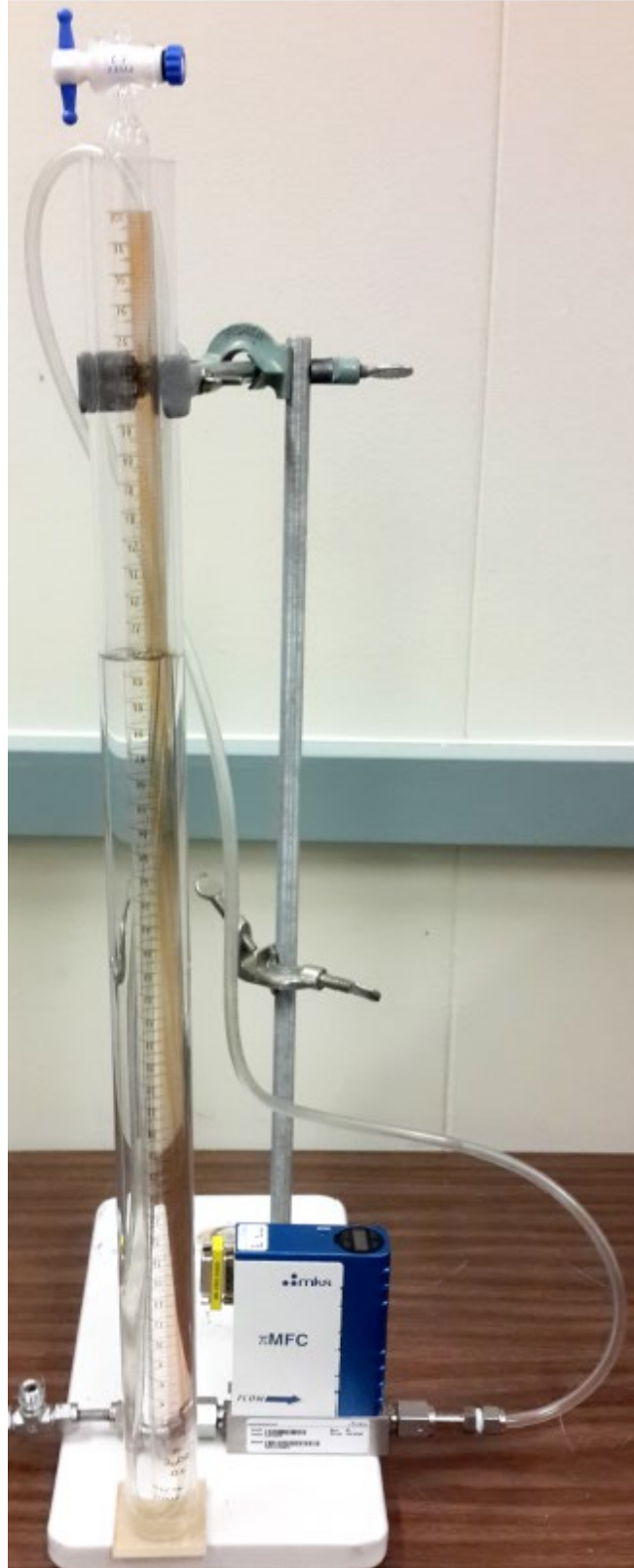


Figure 2.9. A photo of Kojok's volume displacement method, using the MFC, a burette, and an acrylic tube container with water [7].

The calibration factor can then be adjusted to minimize error between the reported and delivered values, and a scatter plot showing the relative error between both values versus the amount of time the MFC is open can be produced to show a downward trend. Since the initial 2-3s rise time ends up delivering less fuel than it should, the error is very high, so all experiments were designed so that the fueling would take at least longer than this amount of time in order to ensure greater accuracy in the setup. Additionally, by ranging across different amounts of the time the MFC is kept on, plots between the open time and delivered amount of fuel can be made, the slope of which can be used to find the fuel-time calibration constant k from Eqn. 2.3 This was done for all of the fuels used in this work, and the resulting delivered fuel vs time open and relative error plots are shown in Figs. 2.10 through 2.14 with the final results being tabulated in Table 2.2.

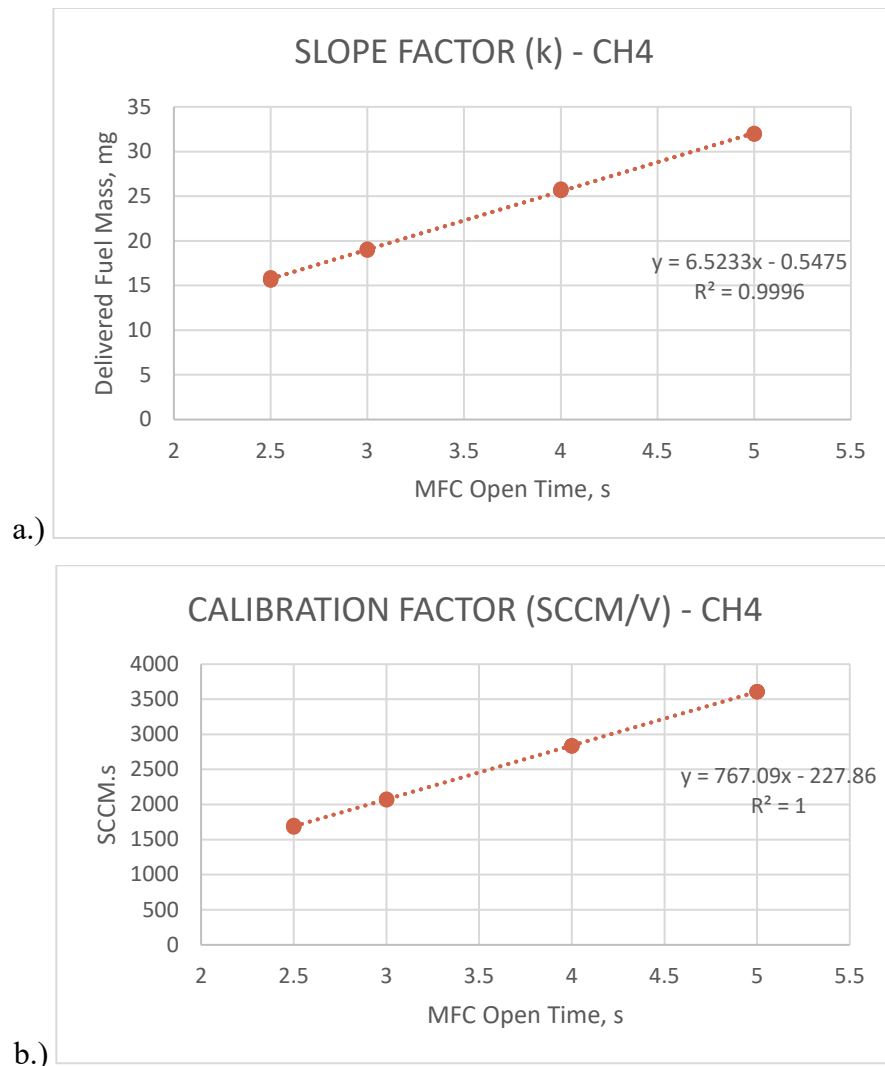


Figure 2.10. Methane calibration plots showing a.) delivered fuel mass vs time results and b.) error between the MFC reported volume and the actual delivered volume.

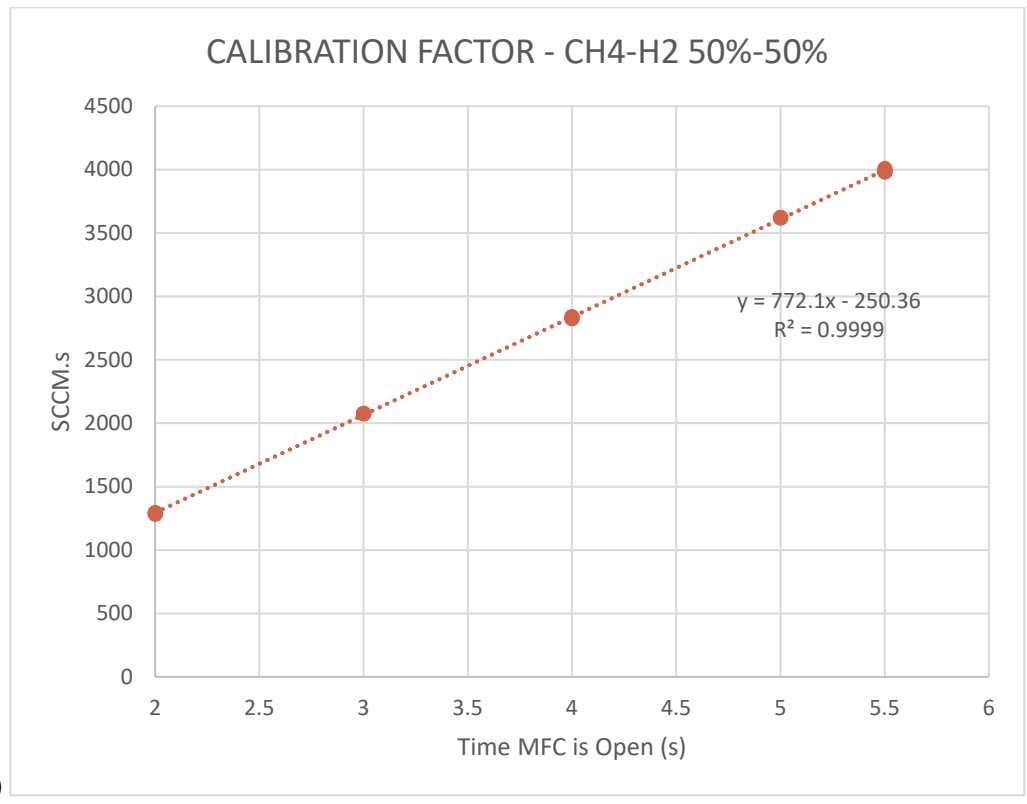
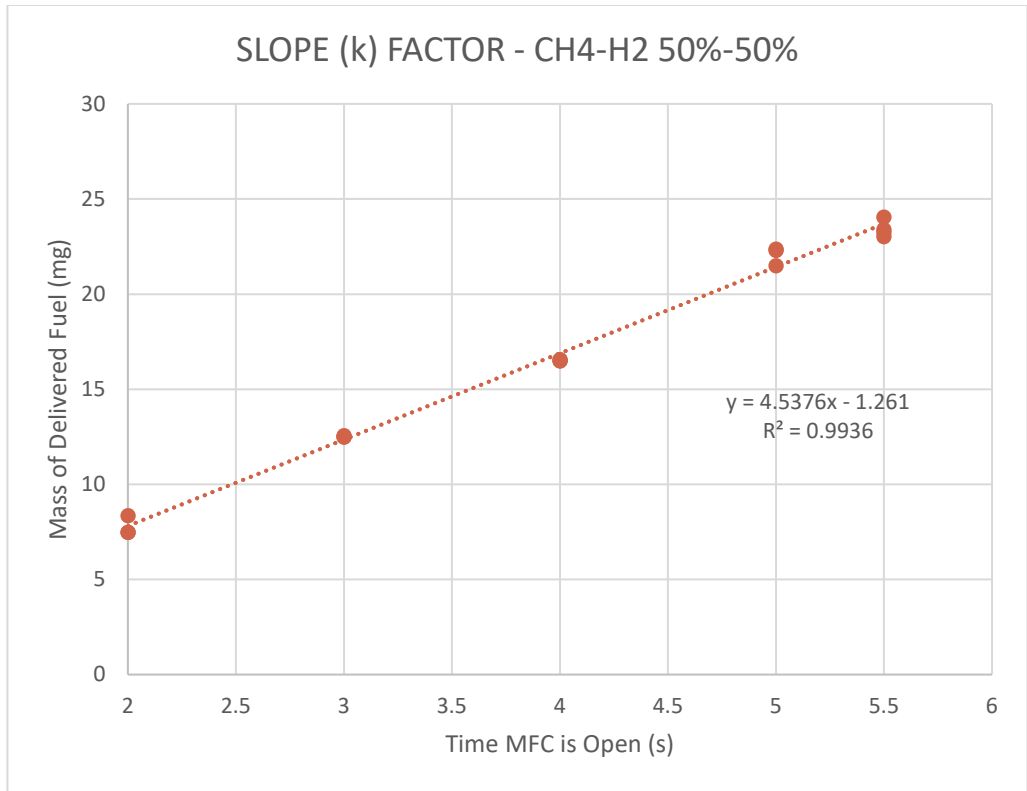
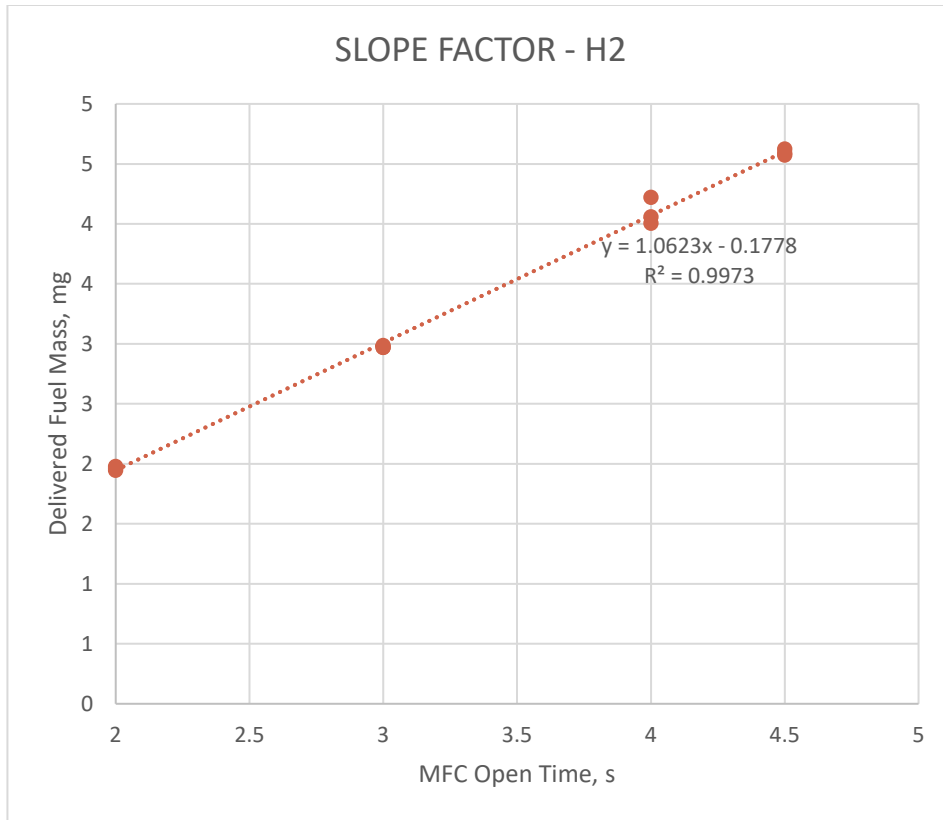
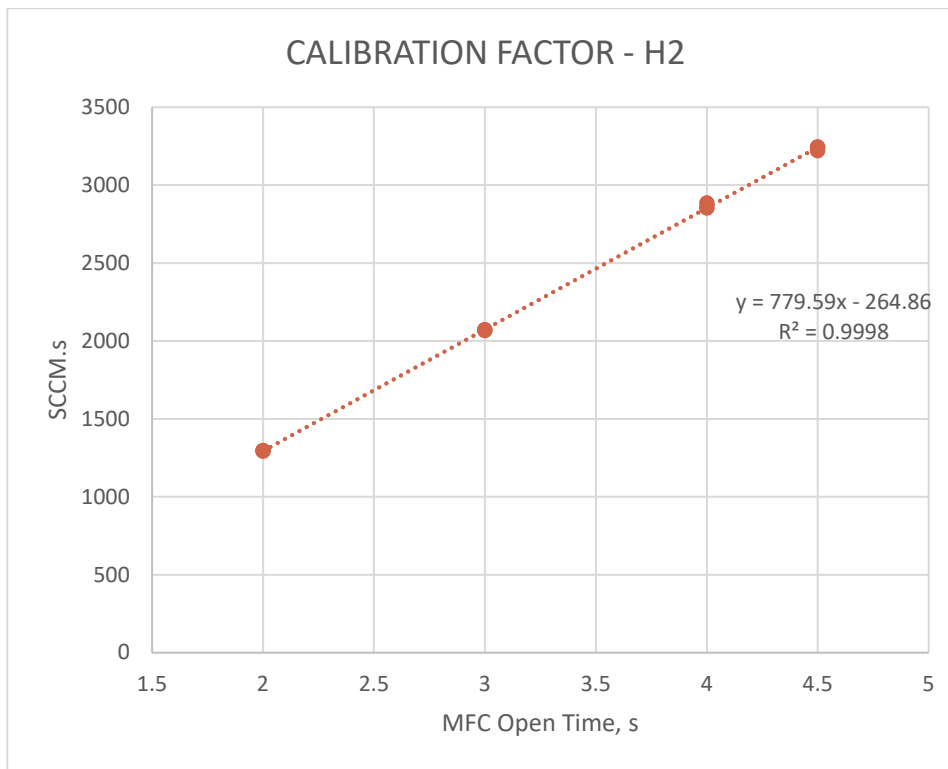


Figure 2.11. 50%-50% Methane-Hydrogen calibration plots showing a.) delivered fuel mass vs time results and b.) error between the MFC reported volume and the actual delivered volume.



a.)



b.)

Figure 2.12. Hydrogen calibration plots showing a.) delivered fuel mass vs time results and b.) error between the MFC reported volume and the actual delivered volume.

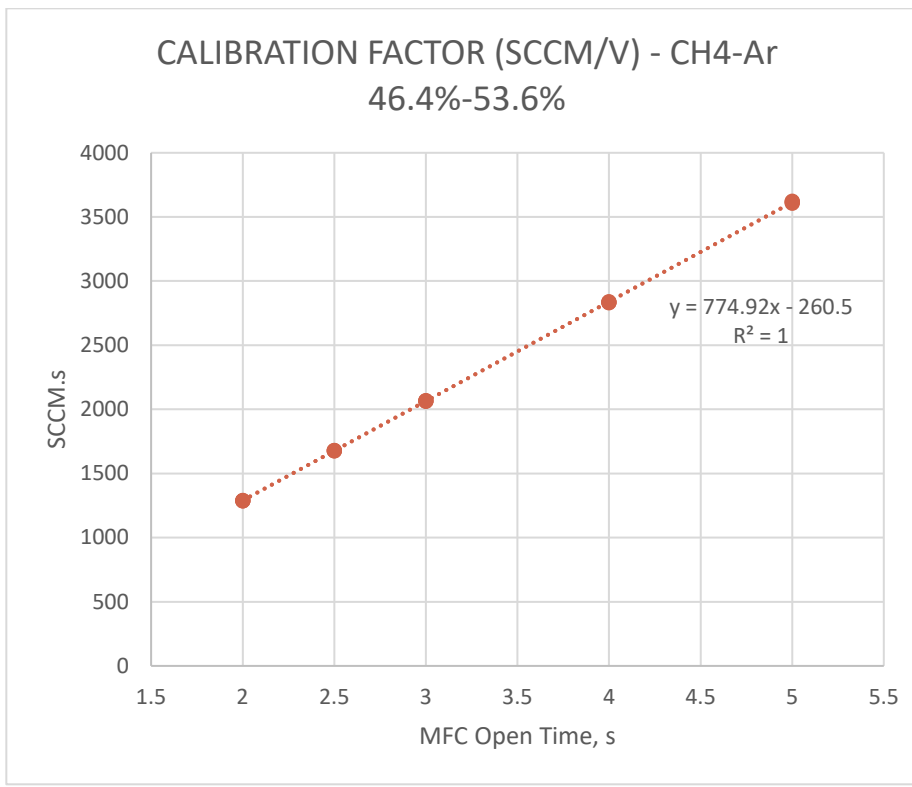
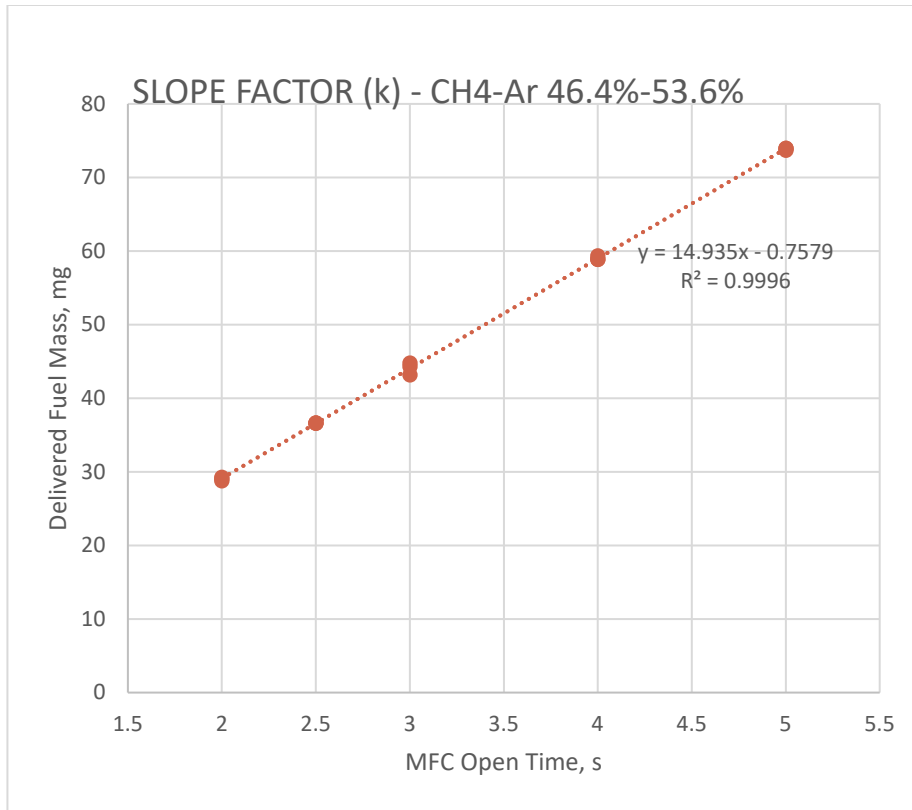
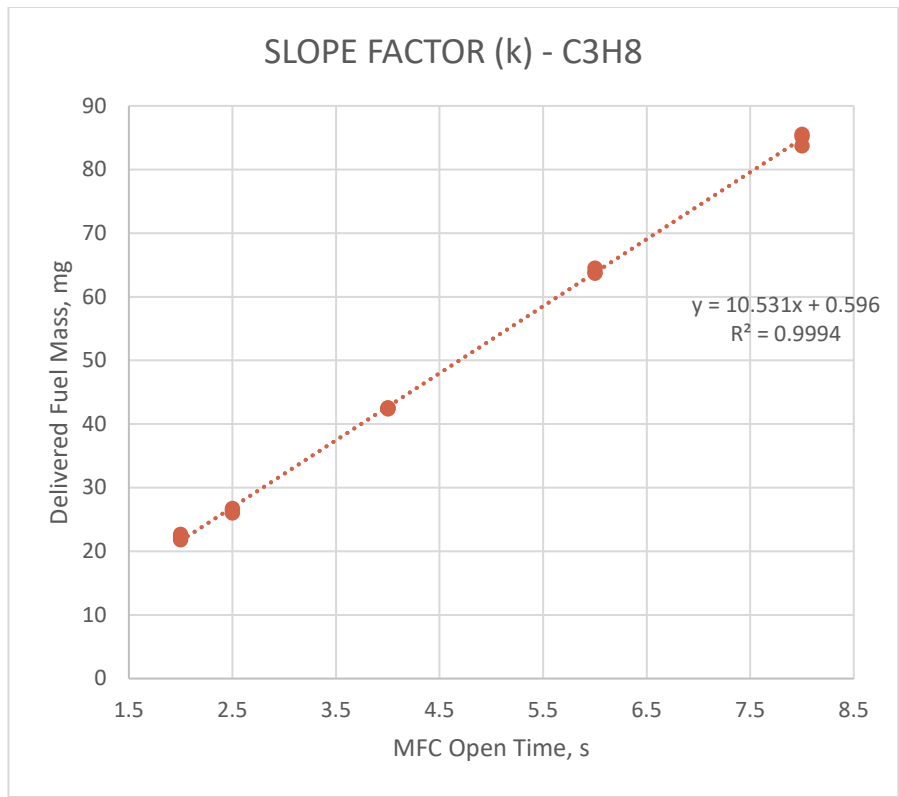
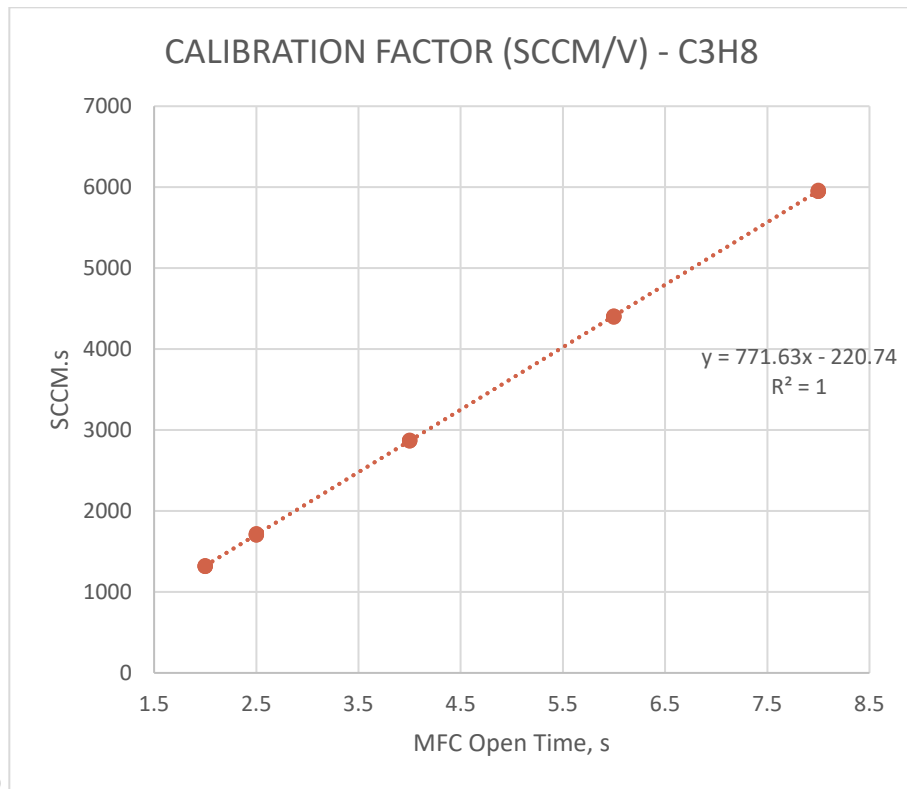


Figure 2.13. 46.4%-53.6% Methane-Argon calibration plots showing a.) delivered fuel mass vs time results and b.) error between the MFC reported volume and the actual delivered volume.



a.)



b.)

Figure 2.14. Propane calibration plots showing a.) delivered fuel mass vs time results and b.) error between the MFC reported volume and the actual delivered volume.

Table 2.2. MFC calibration constants for experimental fuels.

Fuel	Conversion Constant (SCCM/V)			k-Slope Factor (mg/s)	
	Factory	Chowdhury [42]	Current	Chowdhury [42]	Current
H_2	200	200	146	1.338	1.0077
50%-50% CH_4 - H_2	N/A	131	127	3.928	3.9678
CH_4	144	115	115	6.423	6.2557
46.4%-53.6% CH_4 -Ar	N/A	154	152	14.775	14.927
C_3H_8	N/A	56	53	8.674	8.026

2.6 Instrumentation and Data Acquisition

While the main chamber and pre-chamber are some of the most important pieces of the CPRL, there is an entire network of sensors and devices working hand-in-hand to operate the equipment and collect the desired data. In an attempt to visualize this, Fig. 2.15 showcases all of the paths in which data flows from various sensors (e.g. PTs, MFC voltage output, magnetic pickup sensor, etc.) to the data acquisition and control systems (such as the lab computer, LabVIEW, and control box) and back out again to several actuators (like the Phantom camera, spark plug, MFC, etc.).

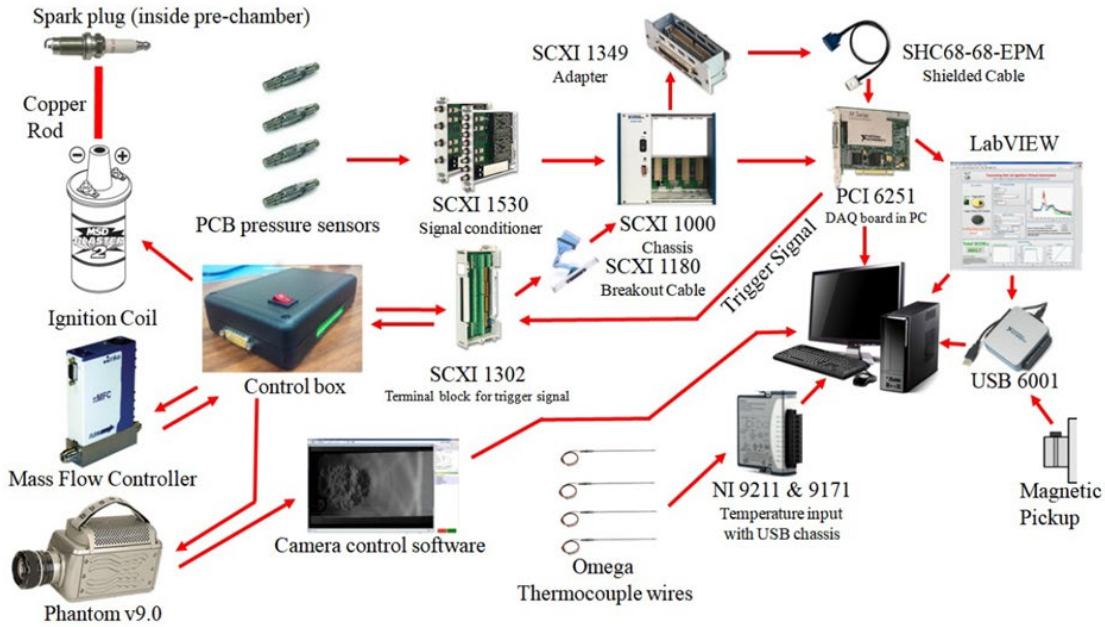


Figure 2.15. Direction of flow of signals and data throughout the instrumentation and data acquisition systems [42].

In untangling this web, the pressure transducers send voltage data to a National Instruments (NI) signal conditioner (model NI SCXI-1530), which then goes to a data chassis (NI SCXI-1000) that is wired directly to the lab computer's data acquisition board (NI PCI-6521) by means of a special adapter (NI SCXI-1349) and shielded cable (SHC68-68-EPM). Continuing on, an NI SCXI-1302 terminal break out board connected to the previously mentioned chassis by an NI SCXI 1180 breakout cable performs several duties, such as generating a special triggering signal for the pre-chamber spark plug through use of a custom-made control box and receiving the mass flow controller's output voltage signal. The control box subsequently plays an important role in triggering the Phantom high speed camera as well, for the signal it generates for the spark plug also goes on to be the necessary signal needed by the phantom control software to trigger the camera into recording footage. Independent from all of the DAQ devices, however, is the NI USB 6001, which receives the magnetic pickup voltage data to be used by LabVIEW to trigger the system.

2.6.1 Electrical Systems

The equipment's electrical system can be laid out in a fairly easy to see method, as demonstrated by Fig. 2.16 A brake switch in the remote control box activates a geared AC motor that is in control of pre-chamber brakes, which allows for the pre-chamber to be either held fixed in a particular orientation or free to rotate. Additionally, to engage the actual rotation of the pre-chamber, the motor is driven by a variable frequency drive (VFD) control box near the apparatus, which is subsequently connected to a remote operation panel on the remote control box by way of a LAN line. Lastly, several components make up the ignition system, including an ignition key that breaks the connection when not engaged. Otherwise, an MSD 6AL ignition module is controlled one of two ways: either through the manual trigger located on the remote control box or by the NI signal conditioner modules. Once engaged, though, a 500V signal is sent to a spark ignition coil, and the resulting 10kV signal initiates whichever sparkplug the coil is connected to.

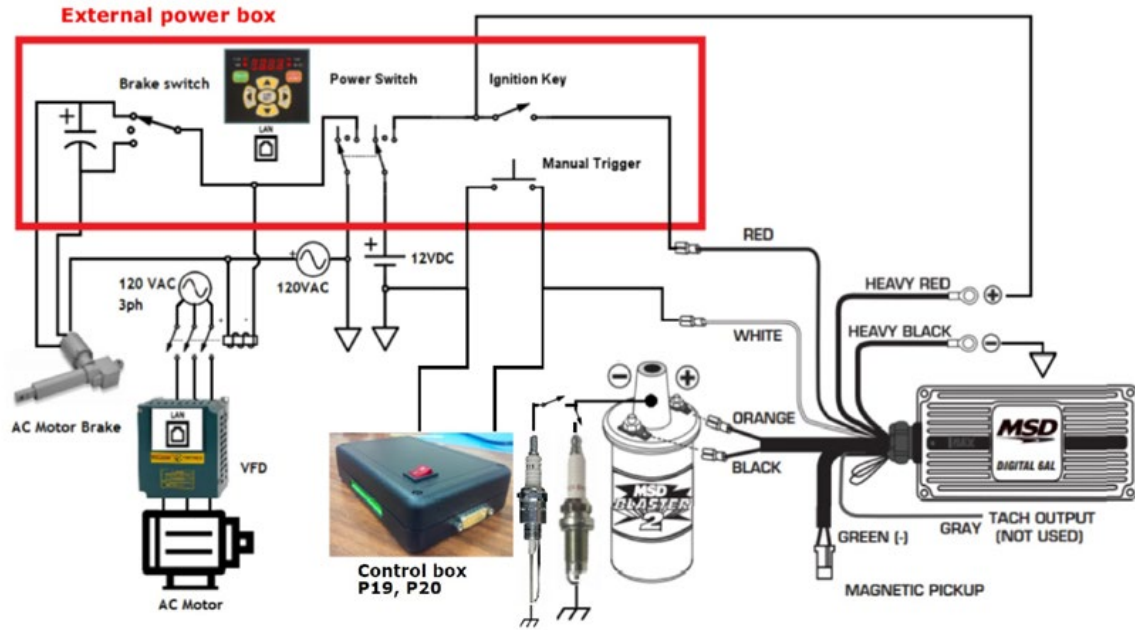


Figure 2.16. Diagram of the experimental apparatus' and remote control panel's electrical systems [42].

2.6.2 Ignition and Control System

As stated previously, the ignition system is responsible for triggering the rig's spark plug (either the one located in the pre-chamber or the one attached to the spark-plug-mounted seal plate depending on which experiment is being conducted) along with the other sensors and equipment through a series of steps. When initiated by the LabVIEW control software, a 5V square pulse width modulated signal is generated by a circuit connecting the computer's PCI-6251 DAQ board, NI SCXI-1000 chassis, and NI SCXI 1302 breakout board – shown in Fig. 2.17 The signal then gets sent to a voltage divider and split into a 1.2V signal that energizes the push button switch on the remote control board and subsequently trigger the spark plug. The 5V signal then travels to an NPN-2222A common emitter transistor within the triggering circuit along with a 5V trigger circuit voltage supplied from the Phantom camera's internal triggering mechanism. Once the pulse modulated signal arrives, the base current in the transistor rises, causing the camera's trigger voltage to drop to 2V. As a result, the camera trigger activates, and the high speed camera begins recording footage of the experiment. From here, the circuit follows different paths depending on whether stationary hot jet/spark-ignited flame or traversing hot jet ignition tests are being

is sent to the MFC in order to start fueling. The MFC then reports back its resulting voltage corresponding to how much fuel was delivered through the system, and this signal is delivered to the NI SCXI-1302 breakout board. From here, the DAQ board within the computer reads the signal and converts the voltage to an SCCM amount using the SCCM/V calibration factors found through the fuel calibration tests. If need be, the internal fuel settings of the MFC can be modified by hardwiring the MFC to the lab computer directly with an Ethernet cable, but for the purposes of this study, the MFC was kept on the Methane setting throughout all of the experiments and calibrations, as done in Chowdhury [42].

2.6.3 Pre-Chamber Motor and Drive Control System

In order to make the pre-chamber rotate a various desired speeds, a Baldor electric motor (Catalog no. M3218T, 5 HP, 60Hz) has been paired with a VS1MD25 variable frequency drive (VFD) controller. This controller works by changing the frequency of the lab's AC current supply going into the system based on the desired speed; due to the nature of AC voltage in inducing a magnetic field, this new AC supply will create a magnetic field within the Baldor motor that drives the rotor itself and bring the system up to speed. Due to how this system works, the desired rotational speed needs to be input into the system in terms of a controller frequency. Chowdhury performed extensive tests in looking for a correlation between input frequencies and output pre-chamber RPM speeds and developed the following linear equation:

$$N = 39.11x \quad (2.4)$$

Where N is the resulting pre-chamber speed in RPM and x is the input frequency [42].

2.6.4 Remote Control Box

The remote control box can be found in the computational side of the lab located outside of the ET109a experimental facility. It features a brake, on/off, emergency stop, and manual push button ignition switch, as well as the VFD control panel, ignition key, and power indicator bulb – all of which can easily be seen in Fig. 2.18 below. It should be noted that, while still present on the panel, the manual push button ignition switch is no longer used for actual experiments; it now serves as a troubleshooting method to check if the spark plug connection is still strong.

There are a multitude of safety features to protect researchers while in the experimental lab. The pre-chamber brake is always engaged when rotational cases are not being performed; however, the brake is not meant to be used as the primary method for stopping a rotating pre-chamber, as it will wear the brake pad out faster and thus make it less effective in an emergency situation. Instead, the “stop” button on the VFD controller should be pressed, and the pre-chamber should slow down on its own over time. In case of a serious emergency, however, the emergency stop button can be initiated, which cuts all power to the system and engages the brake on the pre-chamber. Additionally, no experiments can occur so long as the ignition key is turned to off. All of these features help promote safety within the lab and ensure no accidents ever occur.

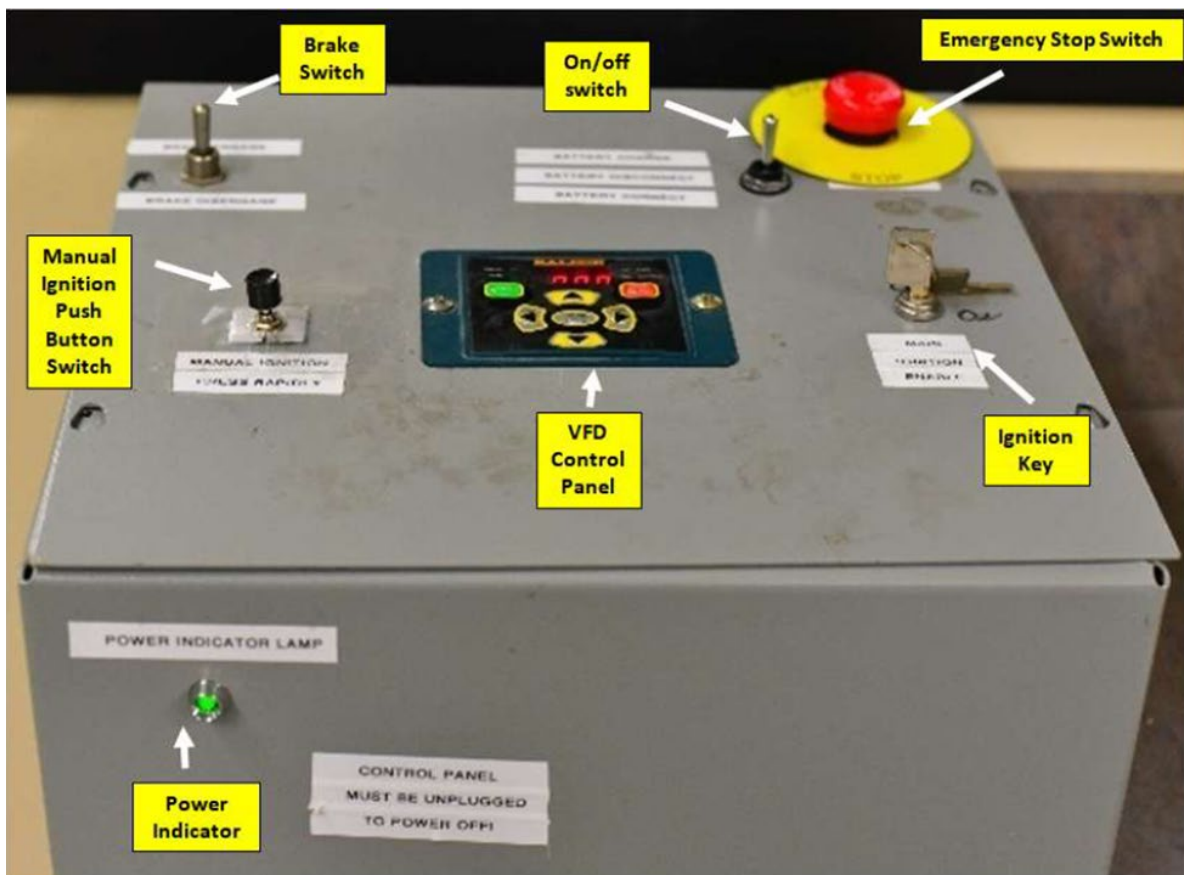


Figure 2.18. The remote control box, featuring labels on all safety switches and buttons [42].

2.6.5 VFD Control Panel

The VFD panel is a small control panel located in the center of the remote control box outside the lab. With it, one gains access to the motor speed control settings, in which a variety of

variables can be set – including operating frequency, torque, acceleration, current, and more. The VFD can also display all of this information in real-time as well. The only setting typically changed for the purposes of the lab, however, is the operating frequency, which changes the pre-chamber rotational speed. An additional panel also exists within the ET109a experimental facility and is mounted to the wall nearest the rig; however, only once of these panels can be used at a time. In order to promote safety, the panel outside the experimental lab portion is used so that researchers are not in the room when the rotation starts up.

For rotational cases, an operating frequency is calculated using Eqn. 2.5 and then input into the VFD remote panel. The green button is then pressed, and the pre-chamber quickly accelerates up to speed; however, it must be a slightly faster speed than what is desired. As described earlier in Sect. 2.4.4, coupling the two chambers will decrease the pre-chamber slightly, and using a tachometer, the speed can be lowered 2% by using the right amount of clamping force. Anything lower would damage the motor and potentially lead to the pre-chamber sparking too soon anyway. Once the experiment is completed, the red stop button can then be pressed, and the motor will decelerate and come to a stop within a matter of seconds.

2.6.6 LabVIEW VI Control Software

LabVIEW Virtual Instruments (VI's) allow users to create their own custom visual interfaces in order to run and control various pieces of lab equipment and experiments. This is done through a graphical form of coding that involves manipulating block diagrams instead of more traditional lines of code. This author adapted the VI's created by Chowdhury [42] and made slight changes to them in order to improve their usability and make them more functional for pumping cases. For instance, a loop function previously only found in Chowdhury's laminar flame propagation VI was added to other VI's in order to make pumping cases more feasible. There are four separate VI's that were consistently used throughout this work: one to perform calibration tests and purge MFC fuel lines, another to run spark-ignited flame propagation experiments, another to control stationary HJI experiments, and a final one to run leak analysis tests. Figures 2.19 through 2.26 below showcase the interfaces and their corresponding block diagrams. Additionally, the outputs received from LabVIEW were imported into MATLAB for further analysis and data visualization [43].

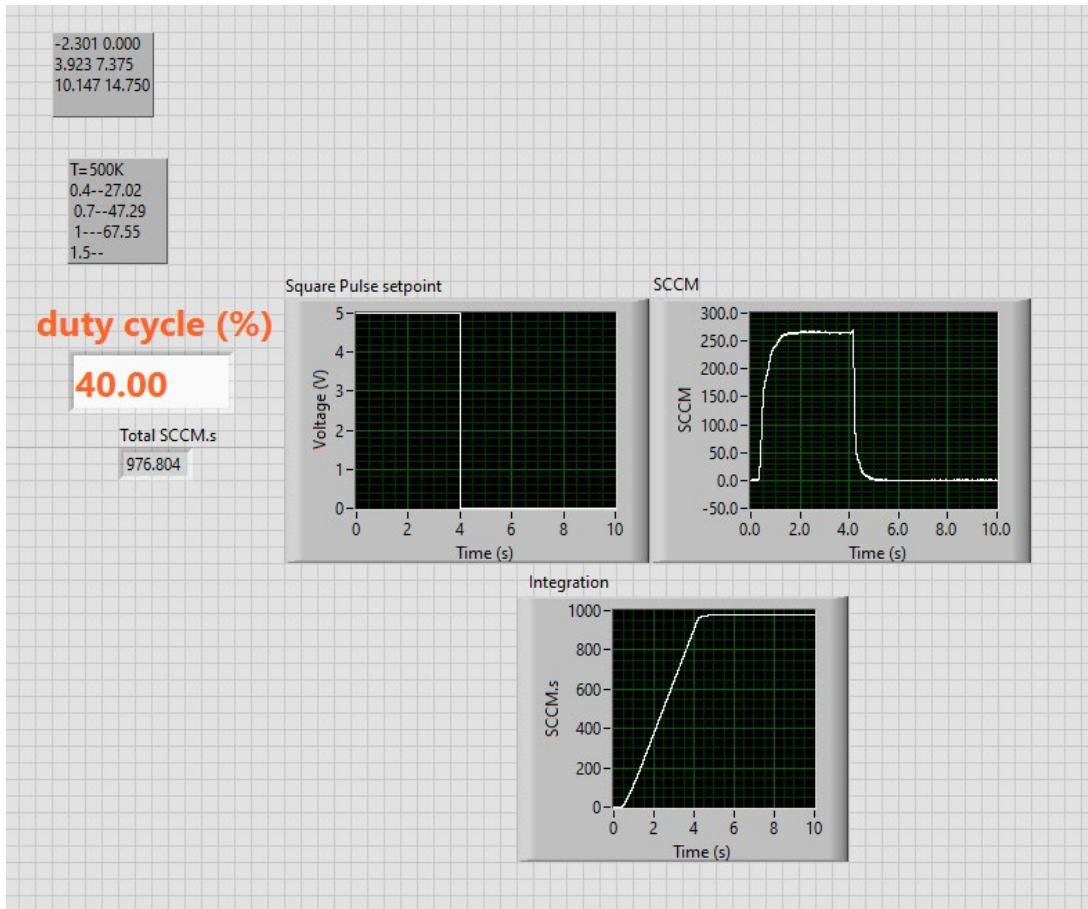
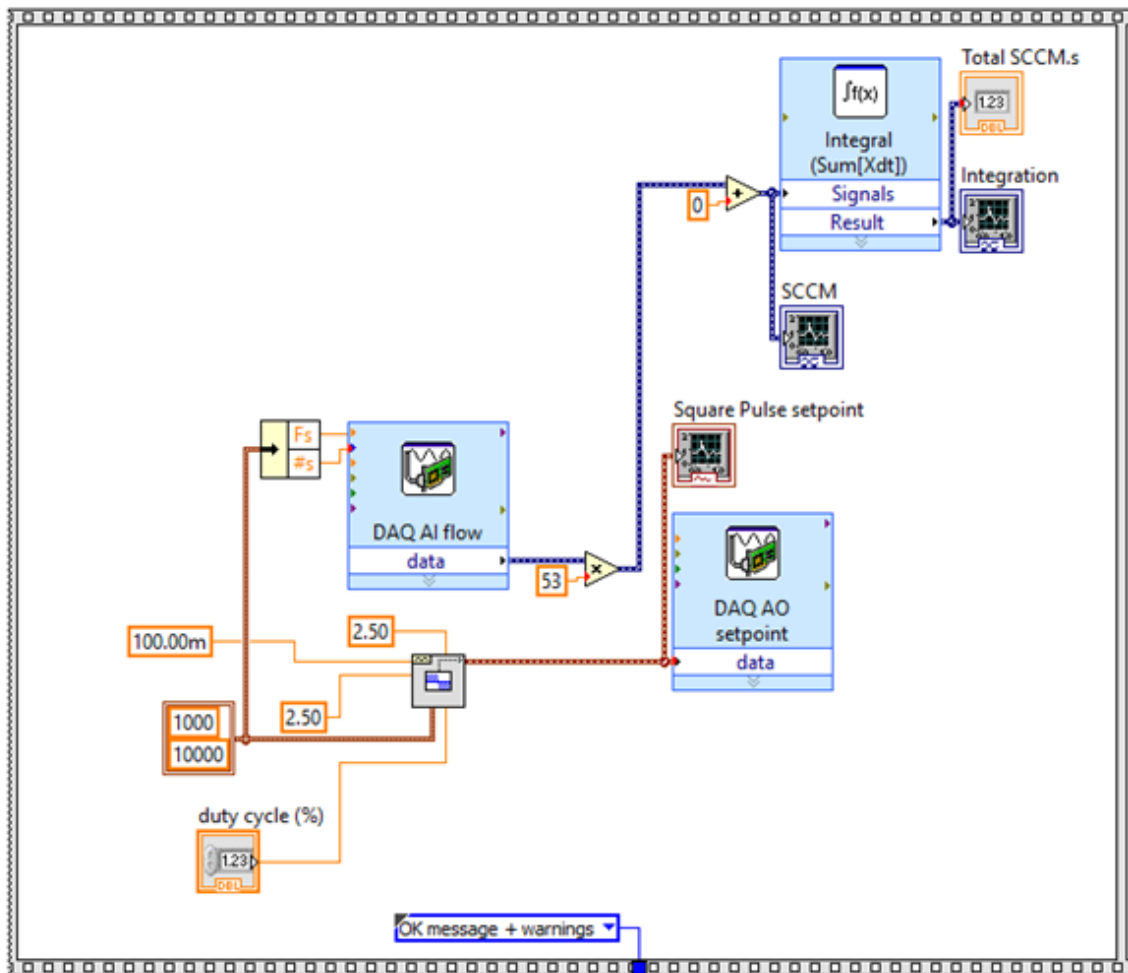


Figure 2.19 Interface for the MFC calibration VI.



Spark Ignition in a long channel of a Constant Volume Combustor

(Press Capture in Phantom Pcc First! Set sampling rate spark pulses etc!)

(Turn off status light! Set mixing time! Spark plug fires when timer reaches zero!)

Information

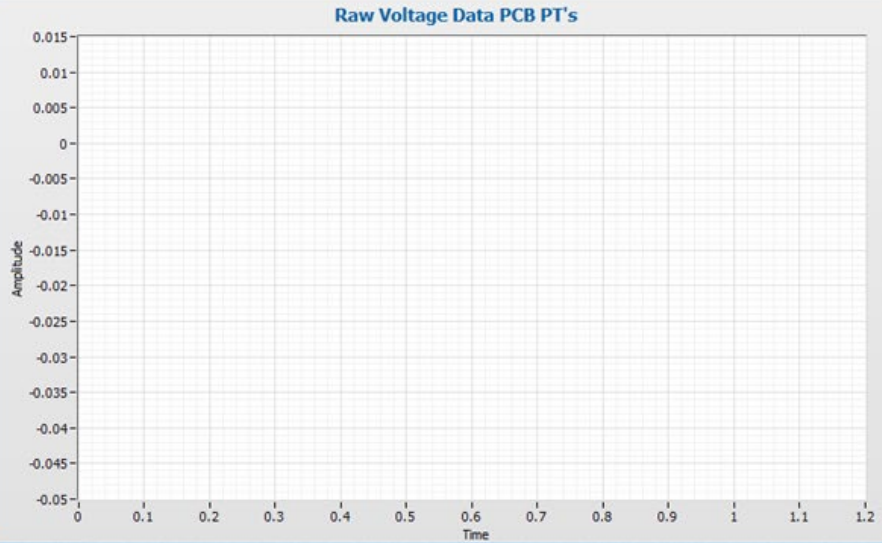
Author: M Arshad Zahangir Chowdhury
Date Created: 04/10/2018 Modified: 07/14/2020
Instruments: Phantom V9, PCB PTs,
NI SCXI-1000, PCI-6251, USB-6001, SCXI-1530,
piMFC, Autolite & Champion 220 Spark Plug



PT settings

Sample Rate:

No. of Samples:



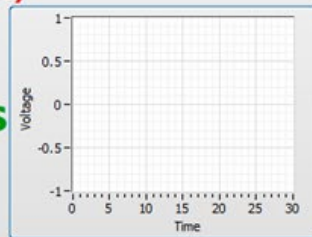
- PT1
- PT2
- PT3
- PT4

Fueling Duty cycle (%)

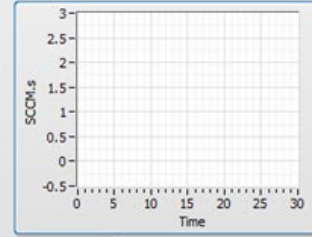
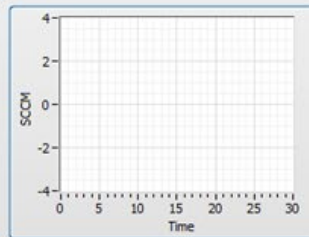
90.07

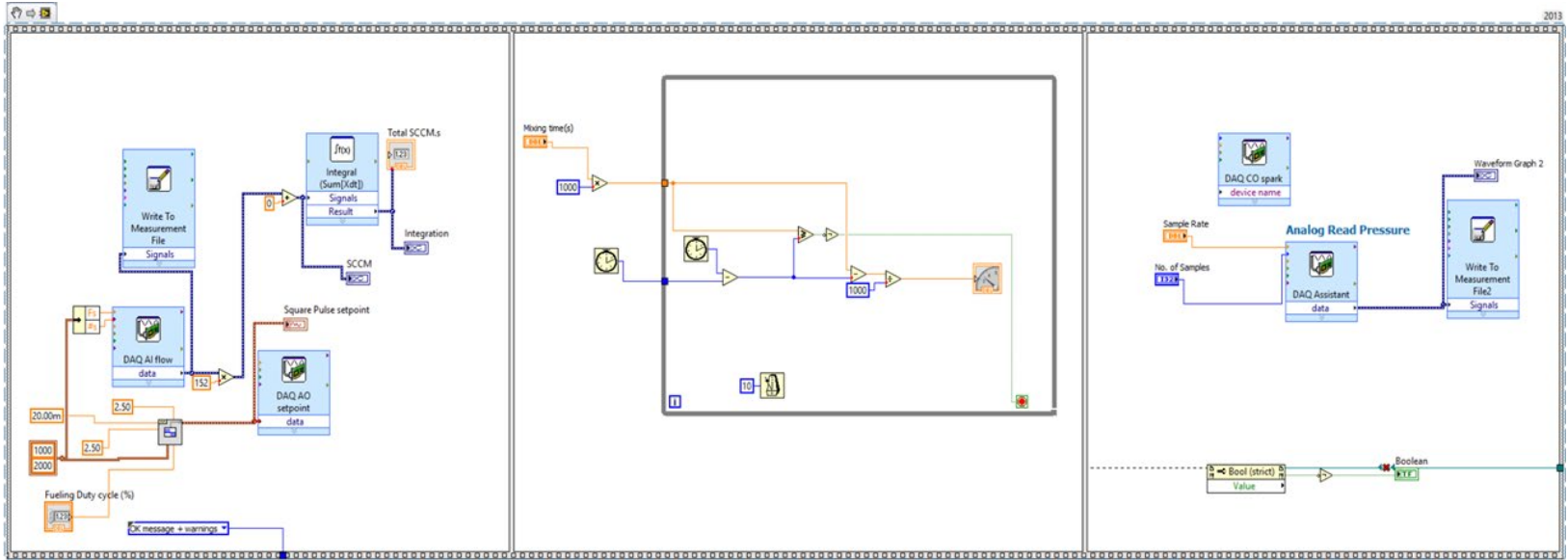
Total SCCM.s

15871.8




Fueling Settings





Timer Settings



Mixing time (s)

0

Status

Filename - Pressure Data
F:\Zack_Research\Stationary HJ Experiments\Data\StatTestNo186-C3H8-Phi1_3-t_0s-NP-Pdata.lvm

Sampling Rate
250000

No of Sample
50000

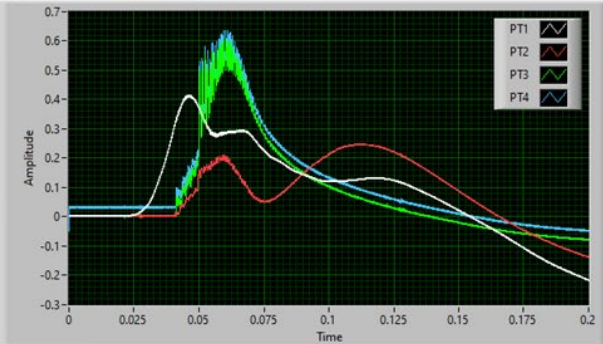
Stationary Hot Jet Ignition Experiment VI

(Press Capture in Phantom Pcc First! Set sampling rate spark pulses etc!)

(Turn off status light! Set mixing time! Spark plug fires when timer reaches zero!)

PT Settings

Pressure data



Duty Cycle (%)

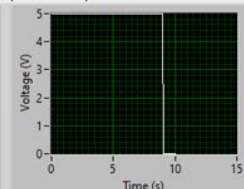
18.05

Total SCCM.s
5572.26

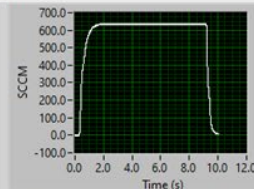
Filename - MFC Data
F:\Zack_Research\Stationary HJ Experiments\Data\StatTestNo186-C3H8-Phi1_3-t_0s-NP-mfc.lvm

Fueling Settings

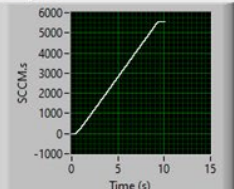
Square Pulse setpoint



SCCM




Integration



Information (Press Capture in Phantom Pcc First! Set sampling rate spark pulses etc!) Date Created: 02/06/2018 by Arshad Chowdhury


Traversing Hot Jet VI (Wait 1s after run!) Instruments: Phantom V9, PCB PTs, NI SCXI-1000, PCI-6251, USB-6001, SCXI-1530, piMFC Modified: 08/04/2021 by Zack Rowe

User Controls

PUMP STATUS


Mixing time (s)

MagV Data

TRIGGER STATUS


PT Timing Settings

Sample Rate

Samples per Loop (total no. of sample)

Spark Settings

Counter

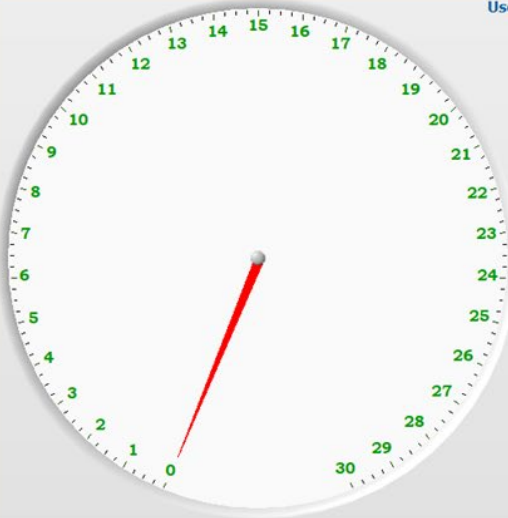
Output Terminal

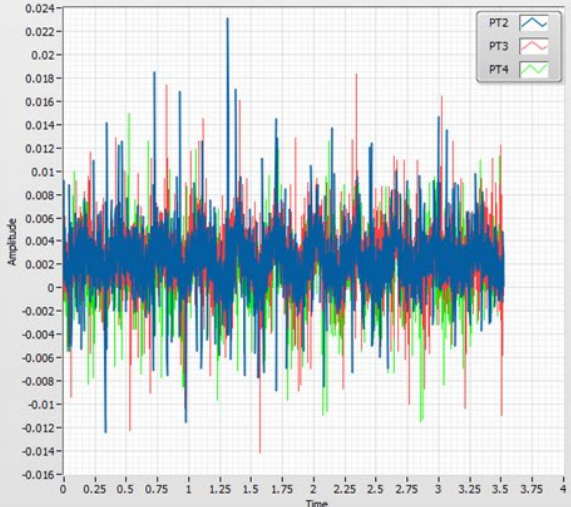
Frequency

Number of Pulses

Synchronizer Settings

Synchronization Type*





File Settings

Filename (Troubleshoot)

Filename (RPM)

Filename (Pdata)

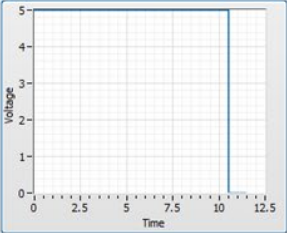
Fueling Settings

Filename (Fueling)

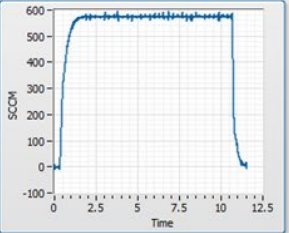
Fueling Duty cycle (%)

Total SCCM.s

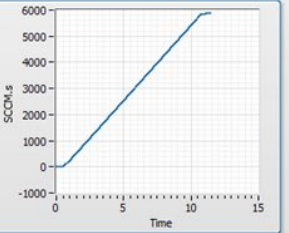
Square Pulse Setpoint

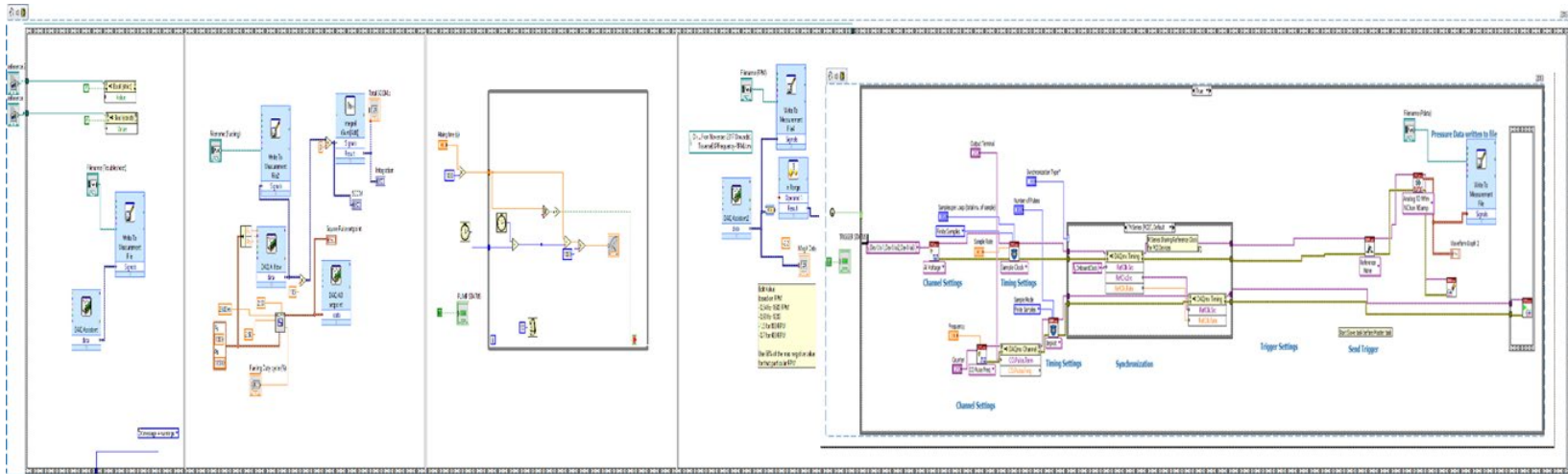


SCCM



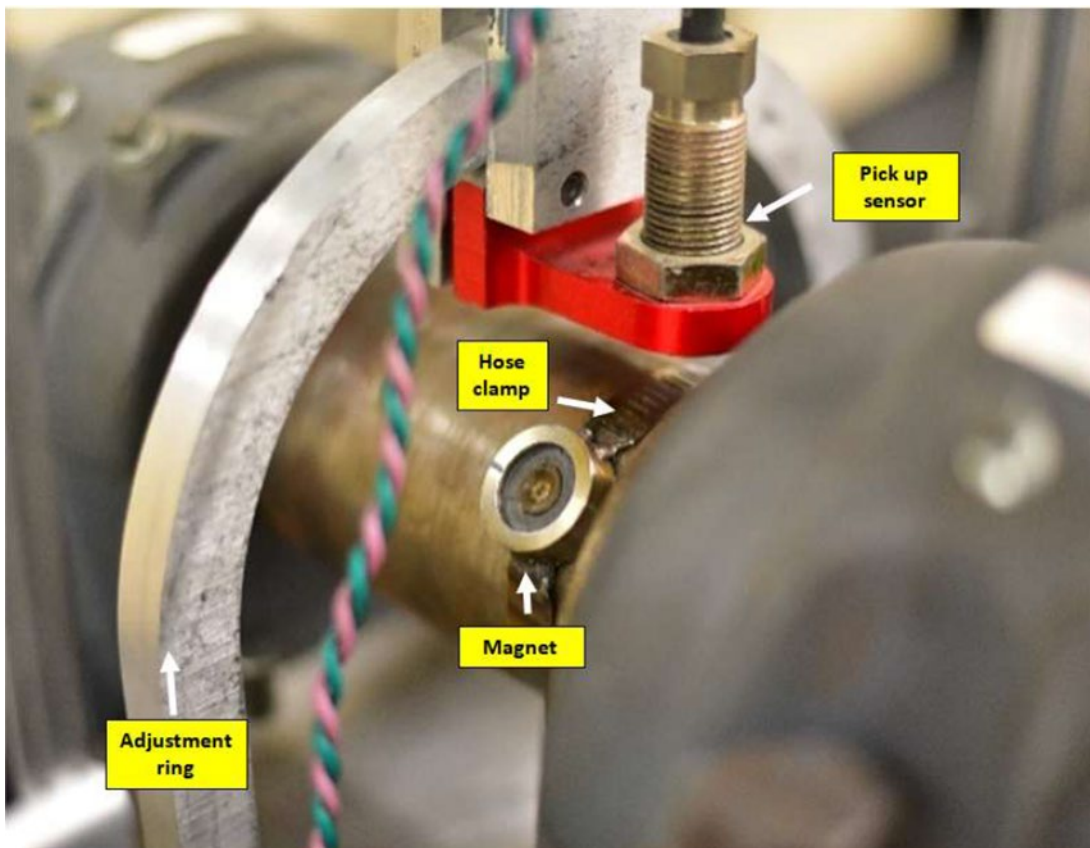
Integration





2.6.7 Magnetic Pickup Sensor

The magnetic pickup sensor configuration (Fig. 2.27) was initially used as a signaling device that communicated with the MSD 6AL ignition box as a way of determining when the spark signal should occur [44]. Chowdhury developed a way, instead, to continuously monitor the magnet's (and therefore the pre-chamber's) position during rotation using an NI USB 6001 DAQ and LabVIEW VI [42]. His VI triggers the pre-chamber spark plug once a specific voltage threshold is reached – specifically, when the magnet is really close to the sensor. The implication of this method is that the threshold changes for each rotational speed, as the velocity of a moving magnet inherently affects the magnitude of an induced voltage. Additionally, while the magnetic pick up sensor itself never has to move, the magnet itself does, which is possible since the magnet is affixed to the top of a hose clamp. This is done so that the spark will trigger earlier or later on in the rotation if the given rotational speed is higher or lower, respectively.



2.6.8 Pressure Transducers

Four PCB Piezoelectric pressure transducers are utilized throughout this experimental rig on both the main chamber and pre-chamber, and specific model information for each transducer can be found in Table 2.3 below. These transducers are vital in finding ignition and rupture moments, shock speeds, pressure wave oscillations, and so on, but in order to be effective, the transducers must operate at significantly high sampling rates. These phenomena operate at such fast speeds and such short time scales, so all of the transducers operated at a 250 kHz sampling rate for both spark-ignited flame and stationary HJI experiments. In terms of the number of samples, though, spark ignition experiments required about 0.8s worth of data typically, while stationary HJI experiments only needed around 0.2s of data. Because the spark flame tests were ignited due to a spark plug rather than a jet ignition source, the ignition process sometimes took a little longer and resulted in flames that moved slightly slower than their HJI-ignited counterparts, requiring longer lengths of data collection. As a result, some spark flame cases that did not want to ignite right away needed 1.2-1.6s-worth of data. Leak Analysis experiments, on the other hand, required much longer sampling times, and because the only phenomena occurring was the pressure fluctuations due to pumping the primer bulb, the sampling rate did not need to be so high. For these reasons, the PTs operated at a 10 kHz sampling rate for 2.1s.

The transducers themselves have been labeled differently in the past. Going through all four, PT1 is also known as “pre-chamber PT,” PT2 is equivalent to “near PT,” PT3 is referred to as “end-wall PT,” and PT4 is called “far PT” in past works. It is also worth noting that each pressure transducer is mounted to the system in different ways. PT1 is embedded in the pre-chamber PT nozzle insert that sits across from the nozzle during stationary HJI tests. PT2, however, was designed by Paik [41] and features the PT part way through a hollow metal loop; because the loop is so long compared to the size of the transducer, it can be approximated as “infinite long” and thus helps protect the transducer by allowing any acute pressure spikes or heat blasts from incoming jets to be dissipated throughout the tube. For PT3, the transducer is mounted flush against the back wall of the inside of the main chamber [7]. Lastly, PT4 is located in a small cavity that resembles a Helmholtz resonator. More details on each of these installations can be found in Paik’s work [41].

Table 2.3. PCB Piezoelectric Pressure Transducer Information

Pressure Transducer	Model #	Conversion Factor (mV/psig)	Installation
PT1	111A26	9.906	Cylindrical Cavity
PT2	113B26	9.861	Infinite Probe
PT3	113B26	9.725	Flush
PT4	113B26	9.992	Chamber Cavity

PT = Pressure Transducer

2.6.9 Schlieren Imaging

The lab employs a Z-type schlieren method in order to visualize flow regimes occurring within the main chamber, which consists of a point light source, two large parabolic mirrors, a razor blade, and a Phantom v9.0 monochrome high speed camera. The way it essentially works is by having a point light source be a distance away from the first mirror equal to that mirror's focal length. The mirror's shape reflects this pin source now as a column of light that is angled in such a way that the light column passes through the main chamber. After doing so, the density gradients within the main chamber refract the light in various angles, and once the column is reflected off the second mirror toward the camera, it starts to revert back to a point. The razor blade then cuts off half of the point, allowing some of the affected light to bend out of and into the camera lens, thus showing the density gradients that were once invisible. For more detail, readers are encouraged to read through the works of Paik [41] and Settles [45], who describe this setup and these concepts at length. A general schematic of this setup is visualized below in Fig. 2.28.

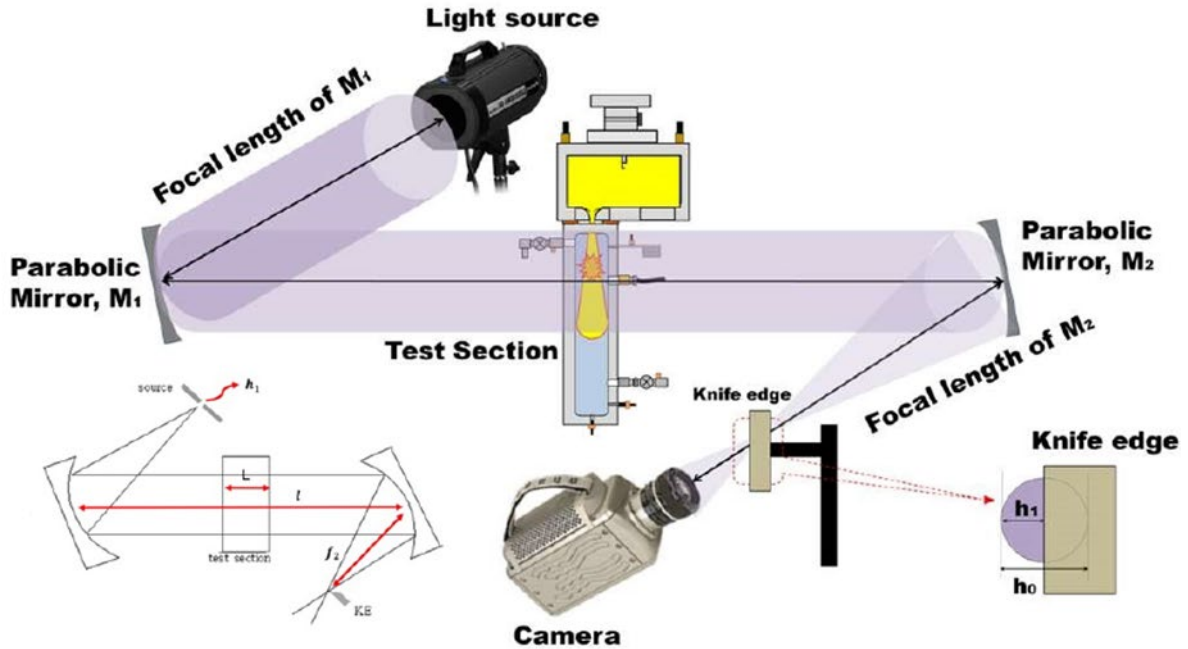


Figure 2.28. A schematic diagram of the lab’s schlieren setup, showing positions and relative angles of the light source, mirrors, camera, razor blade, and lab equipment [42].

The videos captured through this process help largely by allowing CPRL researchers to spot ignition moments/kernels, watch flame propagation, find flow vortices, visualize shock-flame interactions, and more. While these images are very helpful, they do not show the full story, for the size of the mirrors limits how big the column of light can be and therefore how much of the main chamber length is visible at any given time in the video. In this case, the mirrors are only 7in in diameter, which means that only 7in of the main chamber can be visualized at a time. For most cases, the front 7” of the chamber are presented in this work and analyzed; however, there are some cases denoted later on that will showcase the back end of the chamber when necessary. The different camera settings used throughout this work are tabulated below. The different camera settings used throughout this work include: 528x144 resolution and 18691 frames-per-second for spark flame and stationary cases as well as 528x152 resolution and 2000 frames-per-second for leak analysis experiments.

2.6.10 Flame Luminosity Imaging

Because the schlieren technique is effective in only visualizing around half of the main chamber at any given time, it is useful to have another method of recording combustion events throughout the entire length of the chamber. This is accomplished in the lab by using a SONY DSC-RX10 IV high speed digital camera. While it is not fast enough to capture minute details like the schlieren process can, it is still a useful visualization method that is able to capture footage at 960 FPS in full color and still be synced up with the schlieren videos in order to see how the flame propagation continues further on in the main chamber once it leaves the edge of the Phantom footage. The camera unfortunately does not have a way to sync up the triggering mechanism with the Phantom camera; however, it does support a digital end trigger that allows researchers to capture the preceding 3.5s of video once pressed.

2.7 Ignition Process

The following subsections outline a general description of how ignition tends to progress in the two types of combustion experiments researched in this work.

2.7.1 Spark-Ignited Flame Process

The long-stemmed spark plug in the main chamber is triggered by the electrical control software, and during one of the pulses, an ignition kernel forms in-between the spark plug electrodes. As it grows, a spherical wave forms and expands radially outward until it reaches the sides of the chamber. Once this happens, the kernel begins propagating down the length of the chamber; however, due to stratification between the fuel and air, the flame front begins to warp and become asymmetrical. “Heavier” fuels like propane result in flames that propagate with a bulge towards the bottom of the chamber, whereas “lighter” fuels tend to bulge out toward the top. Pressure waves interact with the flame front as it propagates along, and once it reaches the end, the flame dies out, leaving soot and water vapor behind along the chamber walls.

2.7.2 Stationary Hot Jet Ignition Process

When triggered by the control module, an electric signal is sent through a copper rod in the back of the motor shaft to the spark plug inside the pre-chamber that it is connected to. Upon

receiving the signal, a small ignition kernel forms between the spark plug electrodes, and the pre-chamber fuel-air mixture begins combusting. Because this chamber is a constant-volume combustor, the pressure inside increases as more fuel is burned from the kernel propagating outward from the center. At a certain point, the pressure at the nozzle assembly becomes so great that the scored aluminum diaphragm bursts and releases a hot uniform stream of combustion products and chemical radicals into the converging nozzle.

The rupture of the diaphragm and subsequent rapid pressure change releases a rupture shock out ahead of the jet and into the main chamber beyond, where it turns into a reflected shock off the chamber side and back walls and continues propagating back and forth throughout the length of the channel. Following this, the jet of combustion products rushes into the main chamber and begins steadily increasing its pressure while the pressure transducers in the main chamber record the mounting pressure as well as the jet's interactions with the oscillatory reflected shocks. The turbulent mixing of the chemically-active radicals with the chamber's fuel-air mixture eventually spurs an ignition kernel inside the main chamber, and the mixture begins rapidly combusting. The reflected shocks continue bombarding the flame front as it propagates toward both ends of the chamber, resulting in a visible bulk motion of the main chamber's gases. The flame front wavers shakily as a result of these waves and oscillatory motions before finally extinguishing once it reaches the end of the chamber.

2.8 Experimental Procedure

There are three different classifications of experiments being performed with the equipment in this work, and they can be categorized as the following. Spark-ignited flame propagation experiments are tests in which the main chamber is the only combustion chamber in use, and the spark plug seal plate is mounted to it and used as the source of ignition. Stationary hot jet ignition experiments refer to tests in which the main chamber and pre-chamber are coupled together, but the pre-chamber brake is applied and held in place so that the jet does not move during experimentation. Since there is no rotation, the pre-chamber pressure transducer is also in play here and is plugged into the pre-chamber pressure transducer insert. Lastly, leak analysis experiments are those in which the two chambers are coupled together while the pre-chamber is allowed to rotate. In these cases, the pre-chamber pressure transducer insert is replaced with the solid pre-chamber insert, but the pre-chamber does not have any combustion going on, as the main

focus is on the leakage into and out of the main chamber. While different, these experimentation types can be broken down into a series of steps, with all of them sharing a set of preliminary steps that must be done before experiments of any kind can be carried out. The following subsections will detail each type of steps in list form.

2.8.1 Preparatory Steps

1. Turn on the lab computer (ET10902), NI SCXI-1000 chassis, gray remote control box (outside the lab, with the ignition key set to “ON”), and black electrical control box, as well as plug in the NI USB 6001 DAQ if performing rotational cases. This will subsequently turn on the MFC, which will take around 30 minutes to fully warm up, and give one the needed time to perform the remaining tasks.
2. Plug the necessary power and control cables into the schlieren Phantom v9.0 camera to turn the camera on.
3. Make any small adjustments to the schlieren setup as needed.
4. Turn on the Sony RX10 camera once plugged into an outlet with a USB-C cable, and frame the main chamber appropriately.
5. Setup the fuel regulator on the desired fuel tank, and connect the fuel line to the top fueling station.
6. One-by-one, purge all fuel lines with at least 60 psig compressed air before purging them with fuel. Once the MFC is all warmed up, make sure to run it several times in order to adequately purge the MFC line with fuel.
7. Purge the main chamber and pre-chamber with compressed air and run the vacuum pump at the same time if need be in order to assist.
8. Screw on the appropriate seal plate given what kind of experiments are about to take place.
9. Fill the bottom fuel storage tank up with the desired fuel if experiments will require use of both combustion chambers and involve separate fuels to be used in each.
10. Launch the NI Max software on ET10902, and reset, self-calibrate, and self-test each piece of NI equipment currently in use.
11. Pull up the excel fueling calculator and experiment log files, appropriate LabVIEW VI file, and Phantom Camera Controller (PCC) program, and have them ready for input data.

Additionally, it is recommended that the researcher leak test all of the fuel lines in the mixing stations once per month to ensure no leaks have formed. Upon completion, you should now have a warmed up system and be ready to go with any of the below experiment types. After finishing up the final experiment for the day, the entire system must be shut down and thoroughly purged before leaving.

2.8.2 Steps for Spark-Ignited Flame Propagation Experiments

In order to perform spark flame tests, one should first make sure that the red spark plug voltage wire has been transferred from the back of the pre-chamber motor to the spark plug seal plate before continuing. Once verified, the following procedure is followed for each test:

1. Close both air vent valves in order to fully close off the main chamber system. If performing a case with no pumping, then also have the three-way pump valves closed to the main chamber system; otherwise, if pumping is involved, make sure the three-way valve is open between the chamber and pump on both the top and bottom piping.
2. The correct volume of the main chamber setup (which depends on whether or not the pump is in use or not) along with the room pressure and temperature are used to calculate the mass of fuel needed to reach a desired fuel equivalence ratio within the main chamber.
3. Input this number into the homemade LabVIEW calculator to find the duty cycle and time scale values needed for the VI.
4. Set a designated fuel mixing time, duty cycle, time scale, and any other necessary settings in the VI software.
5. Press the “Capture” button in the PCC software.
6. Press the “Go” arrow in the VI to initiate the experiment.
7. If performing a pump case, begin pumping once fueling has stopped; just as the mixing time is about to end, cease pumping, and shut three-way valves completely. Otherwise, wait until the fueling and mixing time have finished, and wait for main chamber to combust.
8. Press record button on Sony camera immediately following a successful combustion event.
9. Purge the main chamber once again after the spark plug has fired and experiment is complete.

10. Save a snippet of the schlieren video recording, and record all of the relevant data in the experiment log file, including room pressure and temperature, exact SCCM.s value reported by the VI, what data was recorded, comments about the experiments, etc.

And that concludes a single spark flame experiment. One has to also make sure that the VI output files are titled properly, and once complete, this process can be repeated as many times as necessary.

2.8.3 Steps for Stationary Hot Jet Ignition Experiments

Before moving forward with a stationary hot jet ignition experiment, the pre-chamber PT insert should be secured in the pre-chamber with PT1 wired into it, and the pre-chamber brake should be engaged so that the pre-chamber nozzle hole is perfectly centered in the main chamber channel entrance. As it turns out, the spark-ignited flame experimental procedure lays a good foundation for performing stationary HJI experiments; the key difference comes from the following steps that are to be performed before the steps listed in the previous section when conducting stationary HJI experiments:

1. Separate the chambers from one another, pull out nozzle assembly, and purge the inside of the pre-chamber.
2. Make/Select a small aluminum diaphragm disk, and score it with a “+”-pattern using the method outlined in Sect. 2.3.2.
3. Secure the diaphragm in the nozzle assembly, and screw this into the pre-chamber insert hole, using the correct orientation described in Sect. 2.3.1 as a guide.
4. Couple the two chambers together again using the XY table and c-clamp.
5. Attach the pre-chamber fuel line to the quick connect on the backside of the pre-chamber – the one opposite of the nozzle.
6. Record the gauge pressure reading while exposed to the ambient air; then seal the station so that the gauge is only exposed to the pre-chamber conditions and vacuum out the contents with the pump.
7. Record the vacuumed air pressure inside the pre-chamber, and fill the chamber back up with fuel close to the original ambient pressure reading, making sure to record this final “fueled” volume as well.

8. Save these values in the pre-chamber fuel calculate tab to verify correct equivalence ratio.

It should be noted that, if the pre-chamber equivalence ratio is not close enough, the pre-chamber must be purged again and refueled until properly satisfied. At this point, the above steps for spark flame experiments can be followed, and after completion, one stationary HJI experiment will have been successfully performed. This culmination of steps can then be done again and again to collect more stationary data.

2.8.4 Steps for Traversing Leak Analysis Experiments

Leak analysis tests involve rotation of the pre-chamber, so first, one must make sure to replace the pre-chamber PT insert with the solid pre-chamber insert and to disengage the pre-chamber brake before continuing on. After ensuring this has been done, the steps to perform a leak analysis experiment are almost the exact same as the steps for a stationary jet experiment; there are just a few major differences between the two. First, leak analysis tests do not require filling of the pre-chamber since no combustion is being performed, so the system can remain coupled using the flexible rope clamp throughout all of the experiments. Second, in-between steps 5 and 6 for spark flame tests, the start button on the VFD panel outside the lab room must be pushed in order to initiate rotation of the pre-chamber. Third, right after initiating pre-chamber rotation, the leakage gap must be set/confirmed using the tachometer and tweaking the clamping force made by the XY table and rope clamp, if need be. Fourth, the stop button on the VFD must be pressed once the experiment is done and data files have been captured. And fifth, the Sony camera does not need to be used in this case because there is no combustion event to see. With these changes in mind, the spark-ignited flame test framework can be followed, and a leak test case will be performed by the end of it for each time the steps are followed.

2.8.5 Design of Experiments

The experiments performed in this work were designed in such a way so as to analyze how stratification between air and various hydrocarbon fuels can affect hot jet ignition delay and other wave rotor channel properties. Because there was a wide range of conditions to evaluate and consider, a factorial methodology was adapted and detailed in the tables that follow (Tables 2.4-2.6). Throughout all the tests performed, the pre-chamber fuel-air mixture had an equivalence ratio

of 1.1 and utilized a 50%-50% CH₄-H₂ fuel blend. Additionally, every data point was repeated at least three times to confirm results and create the averages and standard deviations found in the following results section. Additionally, the leak test portion of this study only involves examining the fluid flow through the chamber while pumping when the pre-chamber is rotating and at rest; no combustion occurs in these cases.

Table 2.4. Experimental Design of Spark-Ignited Flame Tests.

Fuel	Φ	Mixing Time (t_{mix}), s	Mixing Method
CH ₄			
50%-50% CH ₄ -H ₂			
H ₂	0.4, 0.7, 1.0, 1.3	0, 10, 30	Diffusion, Recirculation Pump
46.4%-53.6% CH ₄ -Ar			
C ₃ H ₈			

Table 2.5. Experimental Design of Stationary Hot Jet Ignition Tests.

Fuel	Φ	Mixing Time (t_{mix}), s	Mixing Method
CH ₄			
50%-50% CH ₄ -H ₂			
H ₂	0.4, 0.7, 1.0, 1.3	0, 30	Diffusion, Recirculation Pump
C ₃ H ₈			

Table 2.6. Experimental Design of Traversing Leakage Tests.

Fuel	Φ	Pre-Chamber Rotation, RPM	Mixing Time (t_{mix}), s	Pump Orientation	Schlieren View
CH ₄	1.0			Top-to-Bottom	
H ₂	1.0	0, 400	0, 15	(T2B), Bottom-to-Top	Front Half, Back Half
C ₃ H ₈	2.0			(B2T)	

3. EXPERIMENTAL FINDINGS

3.1 Spark-Ignited Flame Experiments

This subsection delves into the results of the spark-ignited flame propagation experiments. These experiments served as a preliminary investigation into the stratification effects that Chowdhury first noticed towards the end of his work [42]. Previously, mixing was performed through diffusive means by allowing the fuel-air mixture to sit for various lengths of time, but with the addition of the recirculation pump system, these methods can be compared through both qualitative and quantitative means in order to see if these effects play an important role in combustion within the main chamber.

3.1.1 Flame Front Propagation

One of the ways to examine the pump's effectiveness in dealing with fuel-air layering is to see how the flame front propagates as it combusts through the chamber in the schlieren and flame luminosity recordings. Typically, in volumes with evenly distributed fuel-air mixtures, a small ignition kernel would expand radially outward toward the chamber walls and then evenly propagate down the remainder of the channel. Hydrodynamic and boundary layer effects within a flow have been shown to cause non-planar, symmetric flames, so the flames in a well-mixed combustion chamber should look symmetrical [46, 47]. In contrast, a stratified combustion chamber would mean that the fuel is unevenly distributed throughout the chamber either on the top or bottom; in this case, a fuel less dense than air would rise to the top of the chamber while fuel denser than the surrounding air would sink and stay toward the bottom. This would mean that the top or bottom of the chamber experiences the richest fuel-air density, and since combustion travels faster in areas of higher laminar flame speed (i.e., where equivalence ratios are slightly richer than stoichiometric), the flame would burn faster on the top or bottom depending on if a "lighter" or "heavier" fuel were used, respectively. This would look like an asymmetric flame front. Therefore, whichever mixing conditions produce symmetrical flames should indicate a well distributed fuel-air mixture.

The schlieren images in Figs. 3.1 through 3.5 display the methane, 50%-50% methane-hydrogen, hydrogen, 46.4%-53.6% methane-argon, and propane fuel cases, respectively. Only the

stoichiometric cases are presented as they are representative of the results for each fuel's flame propagation qualities found across all four equivalence ratios tested in this work (0.4, 0.7, 1.0, and 1.3). While each figure depicts every pumping case for each fuel, the methane-argon fuel did not combust without diffusivity or pumping occurring, which is why there is not photo for the 0s no pumping case.

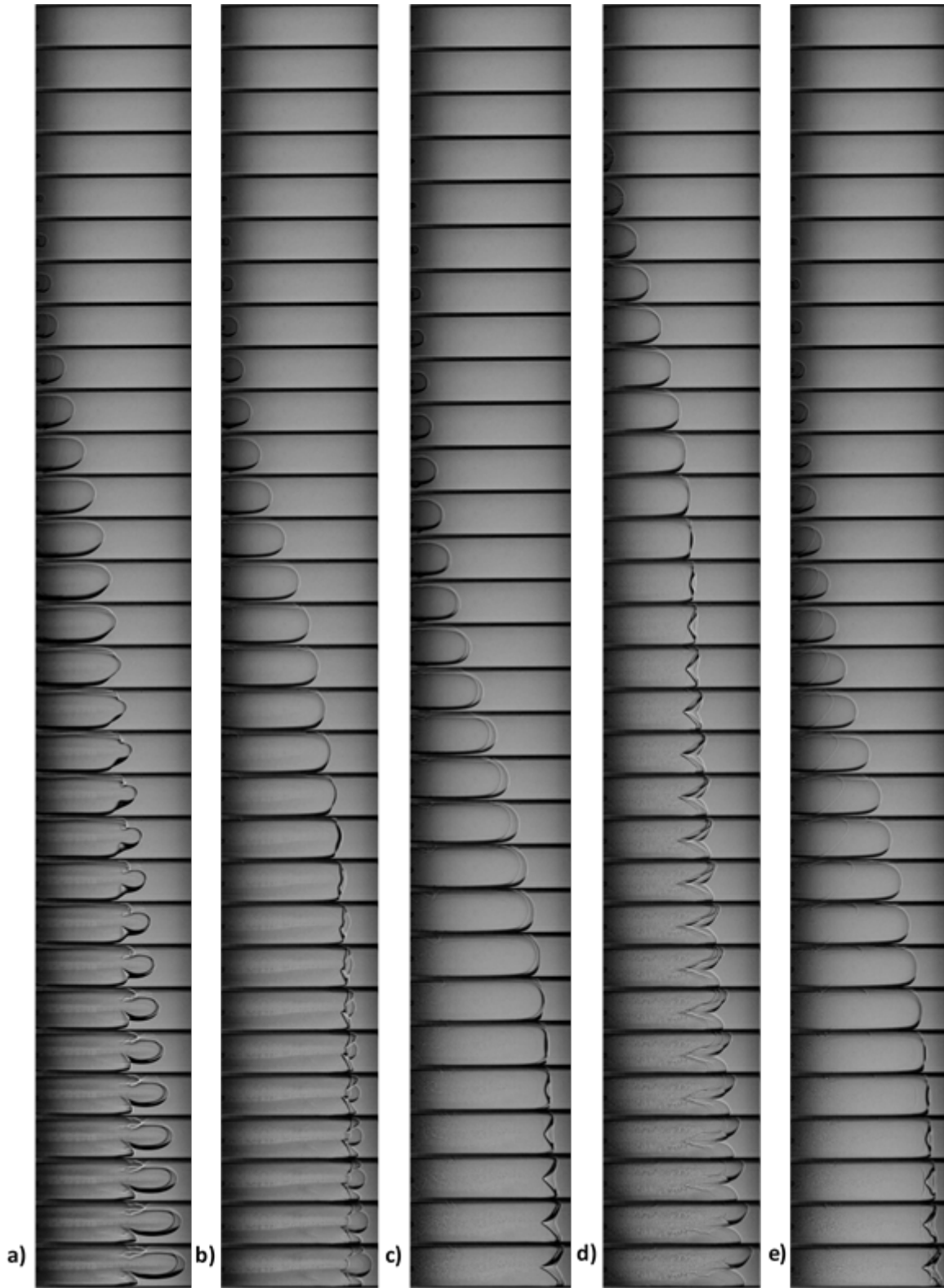


Figure 3.1. Schlieren filmstrips for five methane ($\Phi=1$) test cases: a) Trial 127: $\tau_{\text{mix}}=0\text{s}$, no pump; b) Trial 130: $\tau_{\text{mix}}=10\text{s}$, no pump; c) Trial 137: $\tau_{\text{mix}}=10\text{s}$, pump; d) Trial 135: $\tau_{\text{mix}}=30\text{s}$, no pump; e) Trial 140: $\tau_{\text{mix}}=30\text{s}$, pump.



Figure 3.2. Schlieren filmstrips for five 50%-50% methane-hydrogen ($\Phi=1$) test cases: a) Trial 186: $\tau_{\text{mix}}=0\text{s}$, no pump; b) Trial 190: $\tau_{\text{mix}}=10\text{s}$, no pump; c) Trial 210: $\tau_{\text{mix}}=10\text{s}$, pump; d) Trial 194: $\tau_{\text{mix}}=30\text{s}$, no pump; e) Trial 214: $\tau_{\text{mix}}=30\text{s}$, pump.



Figure 3.3. Schlieren filmstrips for five hydrogen ($\Phi=1$) test cases: a) Trial 235: $\tau_{\text{mix}}=0\text{s}$, no pump; b) Trial 239: $\tau_{\text{mix}}=10\text{s}$, no pump; c) Trial 260: $\tau_{\text{mix}}=10\text{s}$, pump; d) Trial 241: $\tau_{\text{mix}}=30\text{s}$, no pump; e) Trial 263: $\tau_{\text{mix}}=30\text{s}$, pump.

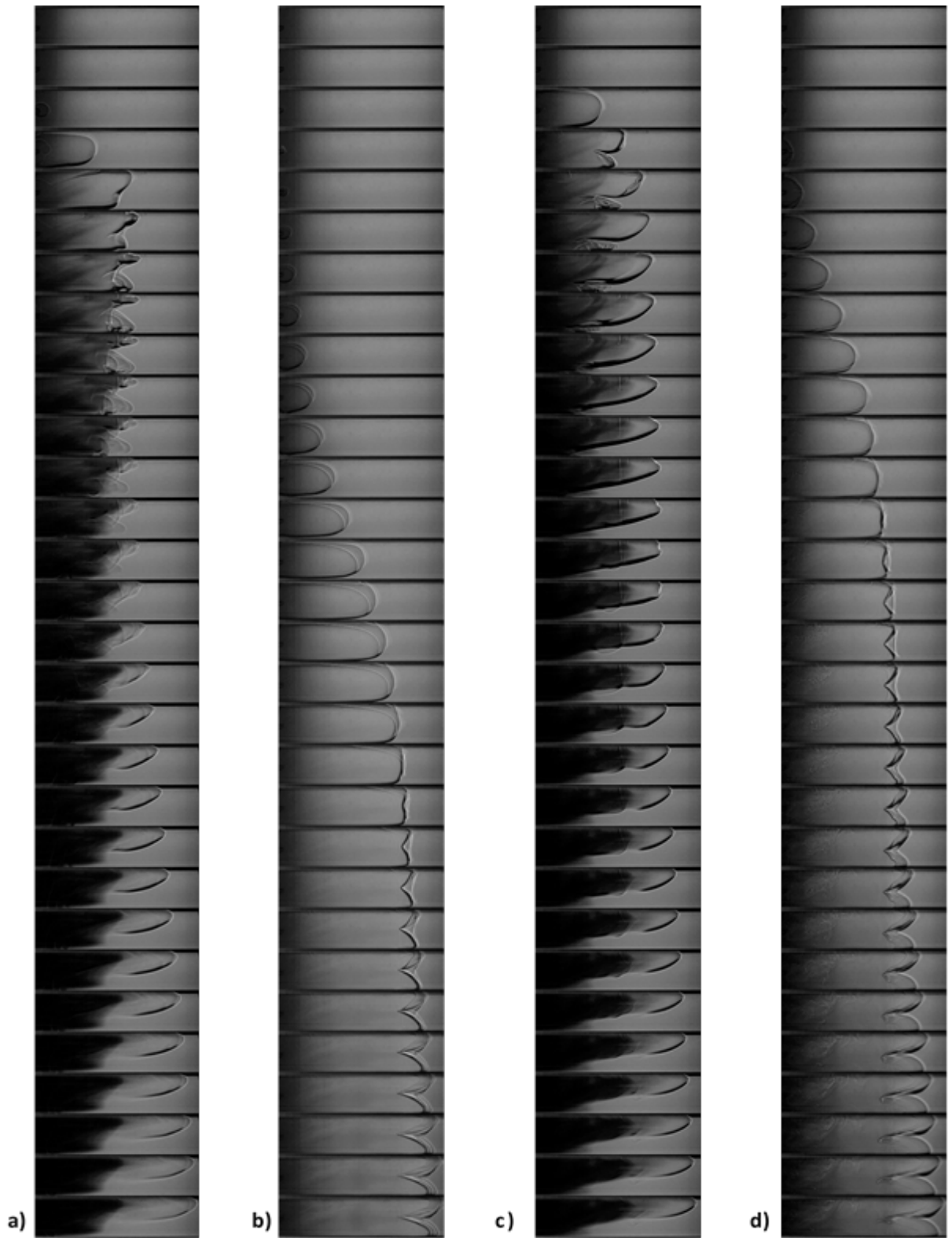


Figure 3.4. Schlieren filmstrips for four 46.4%-56.3% methane-argon ($\Phi=1$) test cases: a) Trial 433: $\tau_{\text{mix}}=10\text{s}$, no pump; b) Trial 472: $\tau_{\text{mix}}=10\text{s}$, pump; c) Trial 442: $\tau_{\text{mix}}=30\text{s}$, no pump; d) Trial 479: $\tau_{\text{mix}}=30\text{s}$, pump.

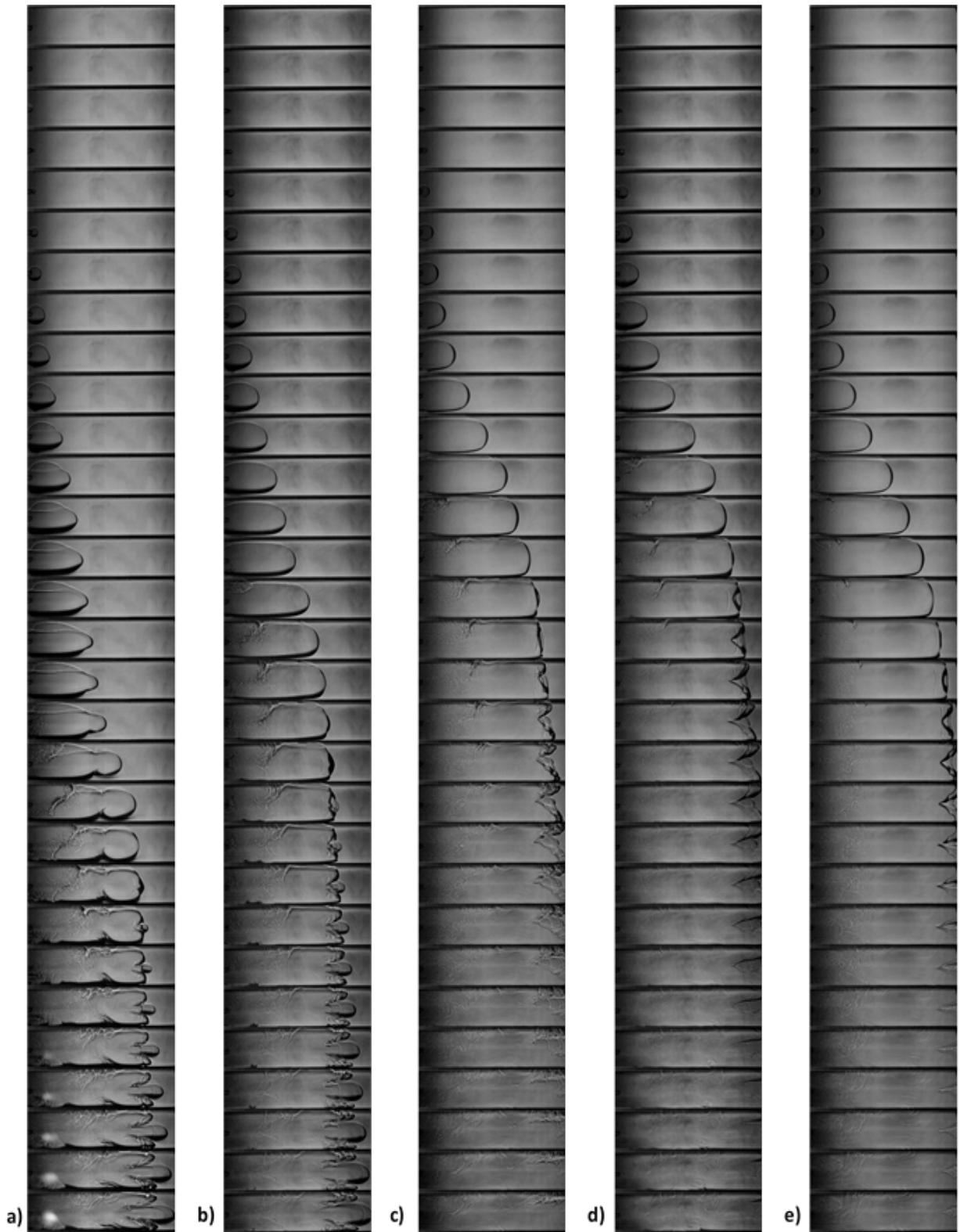


Figure 3.5. Schlieren filmstrips for five propane ($\Phi=1$) test cases: a) Trial 309: $\tau_{\text{mix}}=0\text{s}$, no pump; b) Trial 312: $\tau_{\text{mix}}=10\text{s}$, no pump; c) Trial 395: $\tau_{\text{mix}}=10\text{s}$, pump; d) Trial 315: $\tau_{\text{mix}}=30\text{s}$, no pump; e) Trial 396: $\tau_{\text{mix}}=30\text{s}$, pump.

In Figs. 3.1a and 3.1b representing methane combustion with no pumping for 0s and 10s of mixing time, the flame fronts start out as even and spherical before quickly breaking up and becoming asymmetrical and distorted, with the flame “bubbling” up at and propagating along the top of the main chamber. The longer 30s mixing time and pump cases, however, produce different results, as seen in Figs. 3.1c-e. In these cases, the “bubble” does not develop, and the flame fronts maintain a symmetric shape - appearing more spherical/planar at first before folding in and becoming more of a V-shaped “tulip flame.” Fig. 3.1d maintains a pretty symmetric shape; however, it does not rival the flame fronts made by the pumping cases, which stay symmetric for much longer.

Next, Fig. 3.2 depicts a comparable situation for the 50%-50% methane-hydrogen tests. One thing of note is the 10s and 30s diffusive mixing cases (Figs. 3.2b and 3.2d), which keep a more symmetric flame front throughout the propagation in the video frames than the diffusive cases in Fig. 3.1. The 10s and 30s pumping cases (Figs. 3.3c and 3.3e) do not form a tulip flame as quickly, however, so they are more well-mixed than the diffusive cases. Hydrogen is a highly diffusive fuel, so it does better under diffusive mixing situations compared to the methane case previously seen.

As can be seen in Fig. 3.3, Hydrogen burned much more quickly and brightly than all the other tests - propagating in a spherical flame front most of the time. Each non-pumping case (Fig. 3.3a, b, and d) formed a flame front resembling a tulip flame toward the end of the frames. In contrast, the pump cases shown in Figs. 3.3c and 3.3e develop crisper tulip flames farther along. These pumping cases also show bright flame spots developing much sooner than all the other cases as well. This is due to the faster combustion events produced by the pump cases; since the combustion events are occurring on faster time scales during these cases, they produce sooty flames sooner than their non-pump counterparts.

Looking to Fig. 3.4 for the methane-argon cases, while there is not a 0s no pumping case to compare against, the diffusive cases in Figs. 3.4a and 3.4c contrasted against the pump cases in Figs. 3.4b and 3.4d shows a major difference in the flow. The non-pump cases exhibit extreme stratification toward the top of the chamber immediately on, while the pump cases show well-formed tulip flames by the end of the filmstrips.

Lastly, Fig. 3.5 shows propane to be another fuel heavily affected by stratification. The 0s and 10s no pumping cases (Figs. 3.5a and b) are very asymmetrical in their propagation, while 30s of

diffusion (Fig. 3.5d) ended up distributing fuel comparable to 10s of pumping (Fig. 3.5c). In the end, however, the 30s pumping case (Fig. 3.5e) clearly produced the most symmetrical flame front of the group.

The flame luminosity figures below (Fig. 3.6-3.10) reveal what happened to the flames during the rest of the propagation for the 0 and 30s diffusion and 30s pump cases. These highlight the most difference between both methods of mixing, and the differences are quite noticeable in these figures. For most fuels, the 0s no pumping cases (Figs. 3.6a, 3.7a, 3.8a, and 3.10a) showed clear stratification, with methane, methane-hydrogen, and hydrogen all having a lopsided upper flame front and propane (Fig. 3.10a) having a longer bottom flame front. While 30s of diffusing seemed beneficial in each case (part b of each figure), the 30s of pumping made much more symmetrical flame fronts overall. Hydrogen burned really quickly through the chamber in Fig. 3.8, but slight stratification is noticeable in parts a and b. Additionally, methane-argon's 30s diffusive case (Fig. 3.9a) behaved much like the 0s cases in other fuels, but the 30s pumping case (Fig. 3.9b) was better mixed.

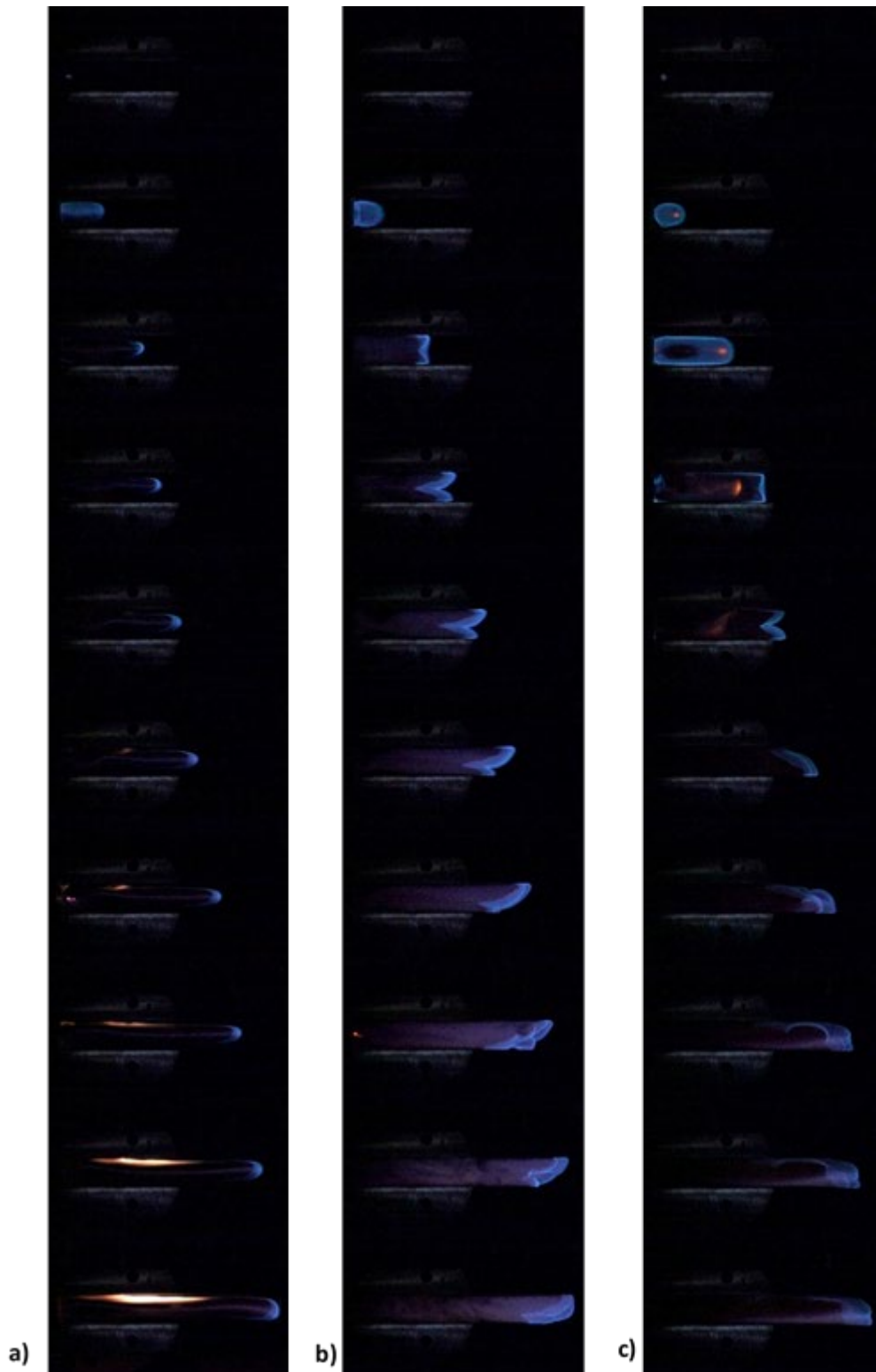


Figure 3.6. Flame luminosity filmstrips for 3 methane ($\Phi=1$) test cases: a) Trial 127: $\tau_{\text{mix}}=0\text{s}$, no pump; b) Trial 135: $\tau_{\text{mix}}=30\text{s}$, no pump; c) Trial 140: $\tau_{\text{mix}}=30\text{s}$, pump.



Figure 3.7. Flame luminosity filmstrips for 3 methane-hydrogen ($\Phi=1$) test cases: a) Trial 186: $\tau_{\text{mix}}=0\text{s}$, no pump; b) Trial 194: $\tau_{\text{mix}}=30\text{s}$, no pump; c) Trial 214: $\tau_{\text{mix}}=30\text{s}$, pump.

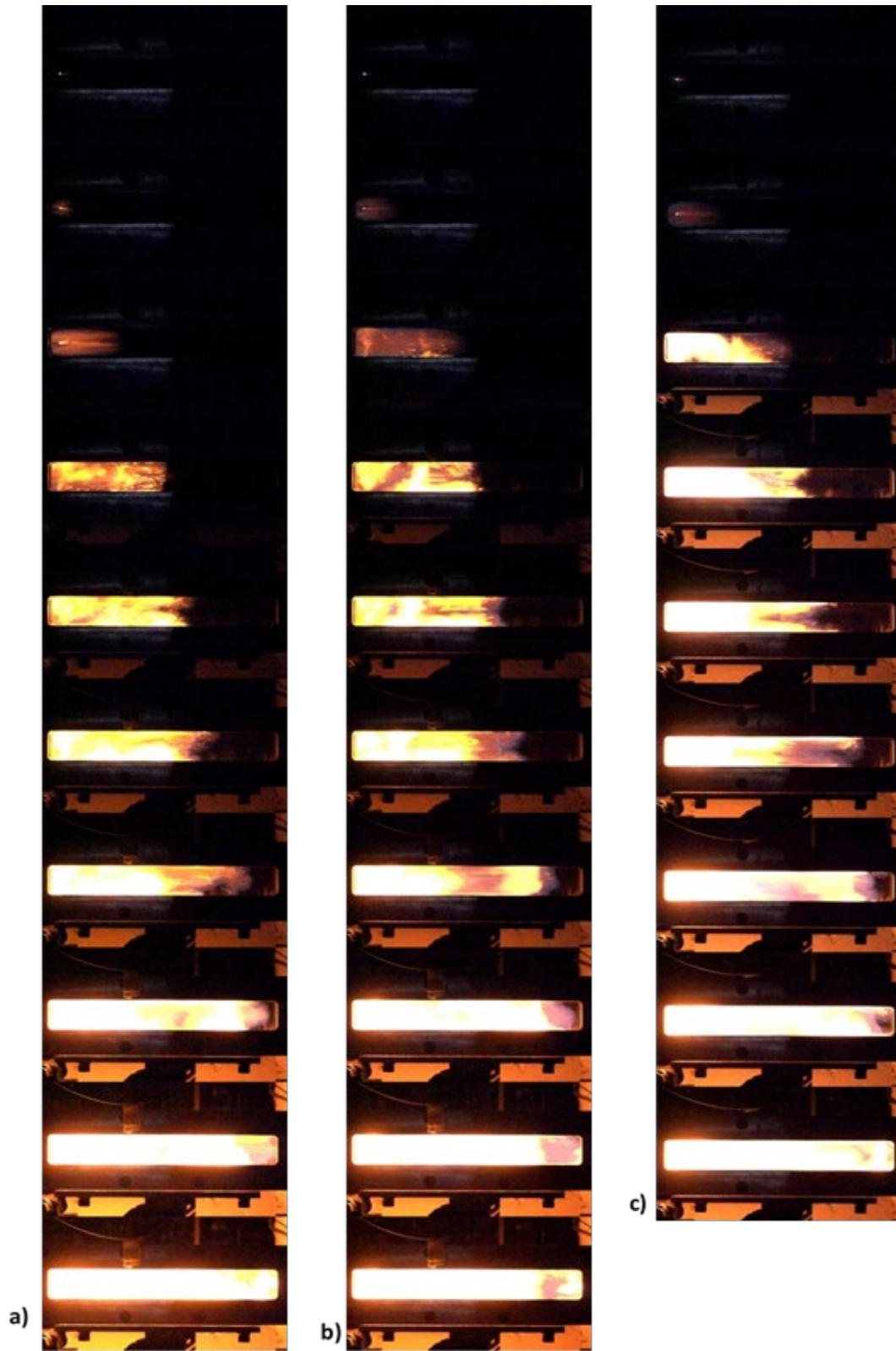


Figure 3.8. Flame luminosity filmstrips for 3 methane ($\Phi=1$) test cases: a) Trial 235: $\tau_{\text{mix}}=0\text{s}$, no pump; b) Trial 241: $\tau_{\text{mix}}=30\text{s}$, no pump; c) Trial 263: $\tau_{\text{mix}}=30\text{s}$, pump.

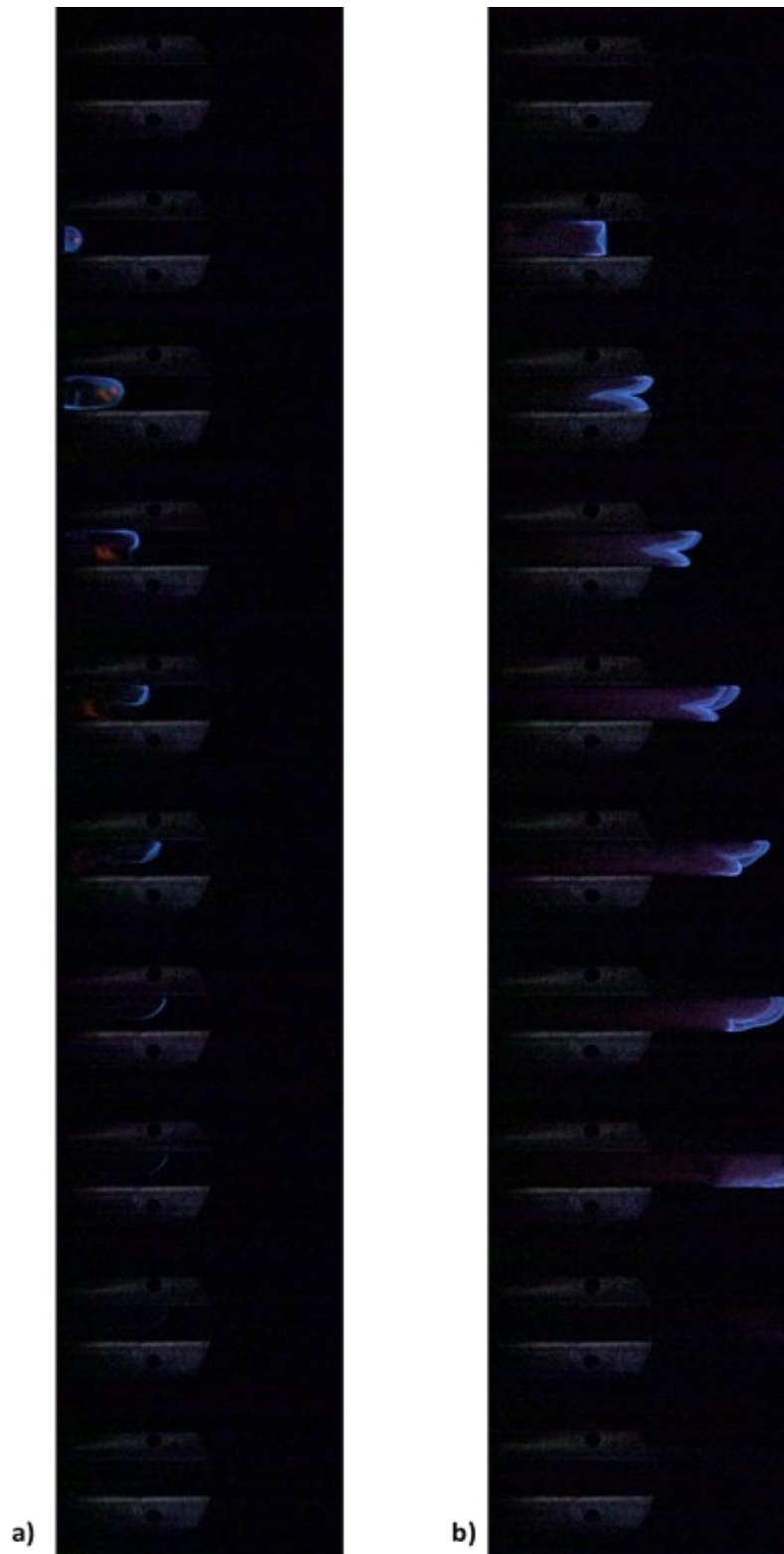


Figure 3.9. Flame luminosity filmstrips for 2 methane-argon ($\Phi=1$) test cases: a) Trial 442: $\tau_{\text{mix}}=30\text{s}$, no pump; b) Trial 479: $\tau_{\text{mix}}=30\text{s}$, pump.

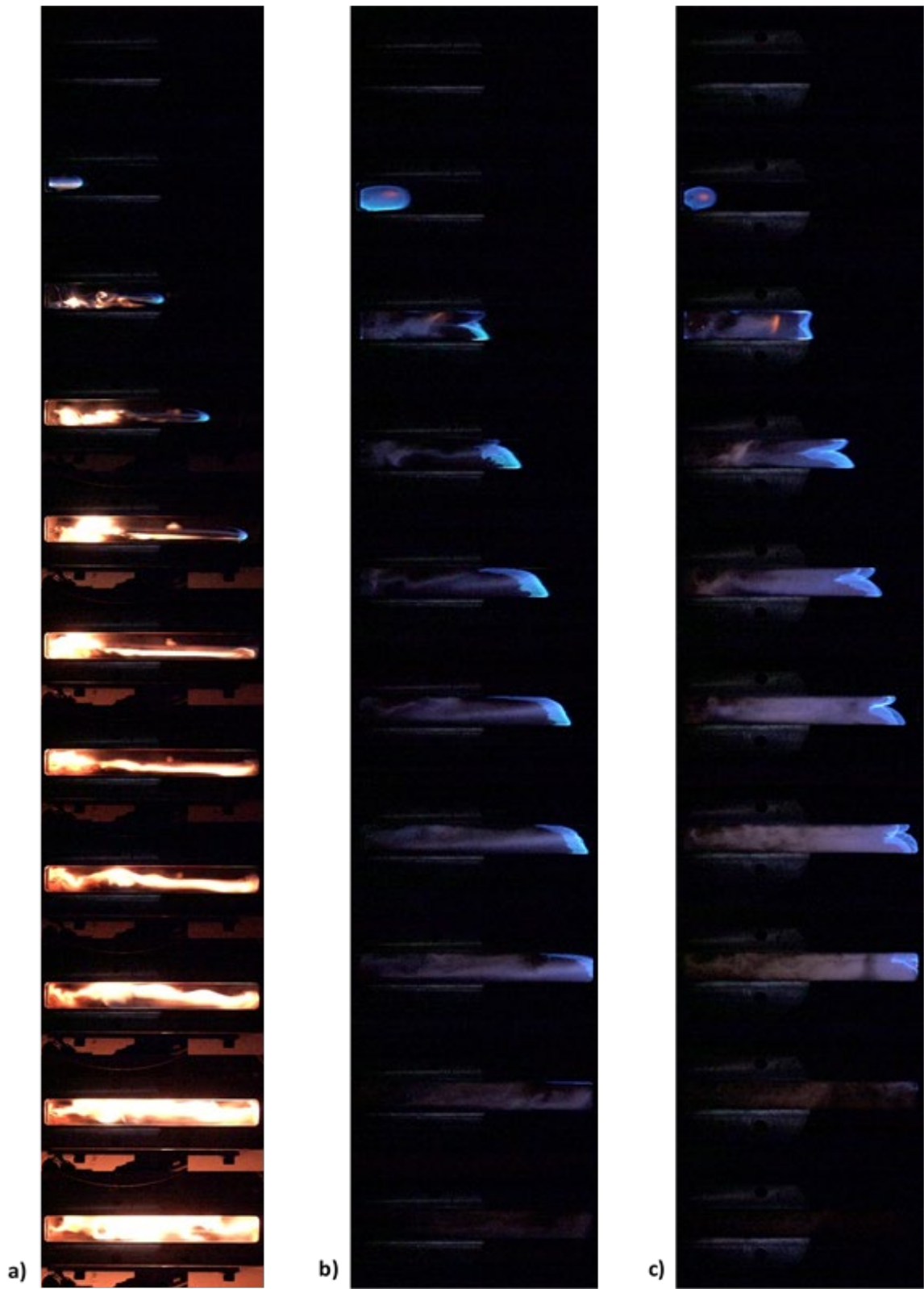


Figure 3.10. Flame luminosity filmstrips for 3 propane ($\Phi=1$) test cases: a) Trial 309: $\tau_{\text{mix}}=0\text{s}$, no pump; b) Trial 315: $\tau_{\text{mix}}=30\text{s}$, no pump; c) Trial 396: $\tau_{\text{mix}}=30\text{s}$, pump.

Overall, these figures clearly show that pumping the fuel-air mixture through the chamber is an effective way to eliminate stratification, with 30s of pumping ensuring this more than any other testing parameter. Additionally, the direction of the pump seems to have an effect on the pump's effectiveness. For most cases, the pump was oriented in the top-to-bottom orientation, but the propane cases would not fire under such conditions. After flipping the pump so that fluid would flow from the front bottom chamber end to the back top chamber side, combustion was able to occur, and as visible in Figs. 3.5 and 3.10, the mixture responded well to this change. Since propane is a "heavier" fuel, it is expected that the fuel would stay toward the bottom. While pumping up into it would help stir the mixture, taking it from the bottom and delivering it to the top should have the best chance at distributing the mixture. And this is backed up with the evidence found in these cases.

3.1.2 Pressure Data Comparisons

For a more quantitative analysis, Figs. 3.11 through 3.15 reveal the pressure histories occurring within the main chamber during each of the experiments seen in Figs. 3.1-3.10 above. The below plots show definitive differences in their shape, duration, and range between each test case. For the 0s and 10s non-pumping cases in each of the following figures, there appears to be a rather distinct peak shape in the plots that does not occur in most cases with the 30s non-pumping and 10s and 30s pumping cases. In fact, 30s of diffusing tends to broaden the curve, a phenomenon that is seen to carry over in most of the pumping cases. Additionally, the pumping cases tend to burn for shorter time scales compared to the non-pumping cases. Along with this, the pressure achieved by the system for each fuel increases the longer the fuel is allowed to mix and distribute in the chamber, aside from Hydrogen. Hydrogen is also special because it is typical to see an extremely tall spike in its PT4 pressure data. Upon further investigation with the schlieren camera, this is caused by an auto ignition event close to the back end of the wall right around where the transducer resides. Hence, this spike is neglected when making the maximum pressure plots later in this analysis. Lastly, the spark-ignition moment and locations of the flame front once it reaches the fueling port, halfway point in the chamber, and end wall as it propagates through the chamber are visible by the vertical colored lines in the plots. Interestingly, there is a little dip found in most of the plots in the PT2 line that occurs around the midway point in the flame's journey. This turns out to correspond with the flame front developing from a spherical flame front into a tulip flame

shape. Once developed and continuing on with its propagation, the flame continues building pressure, with this dip becoming less pronounced with more pumping. All of these effects can be attributed to the pumping cases creating a more homogeneous fuel-air mixture that allows for even combustion and pressure rise, with would combust much faster than a poorly mixed fuel-air mixture. Overall, there is a definitive difference in results between the two mixing techniques, and when paired with the schlieren data, this makes a compelling case that the pump performs an effective, necessary duty for every experiment.

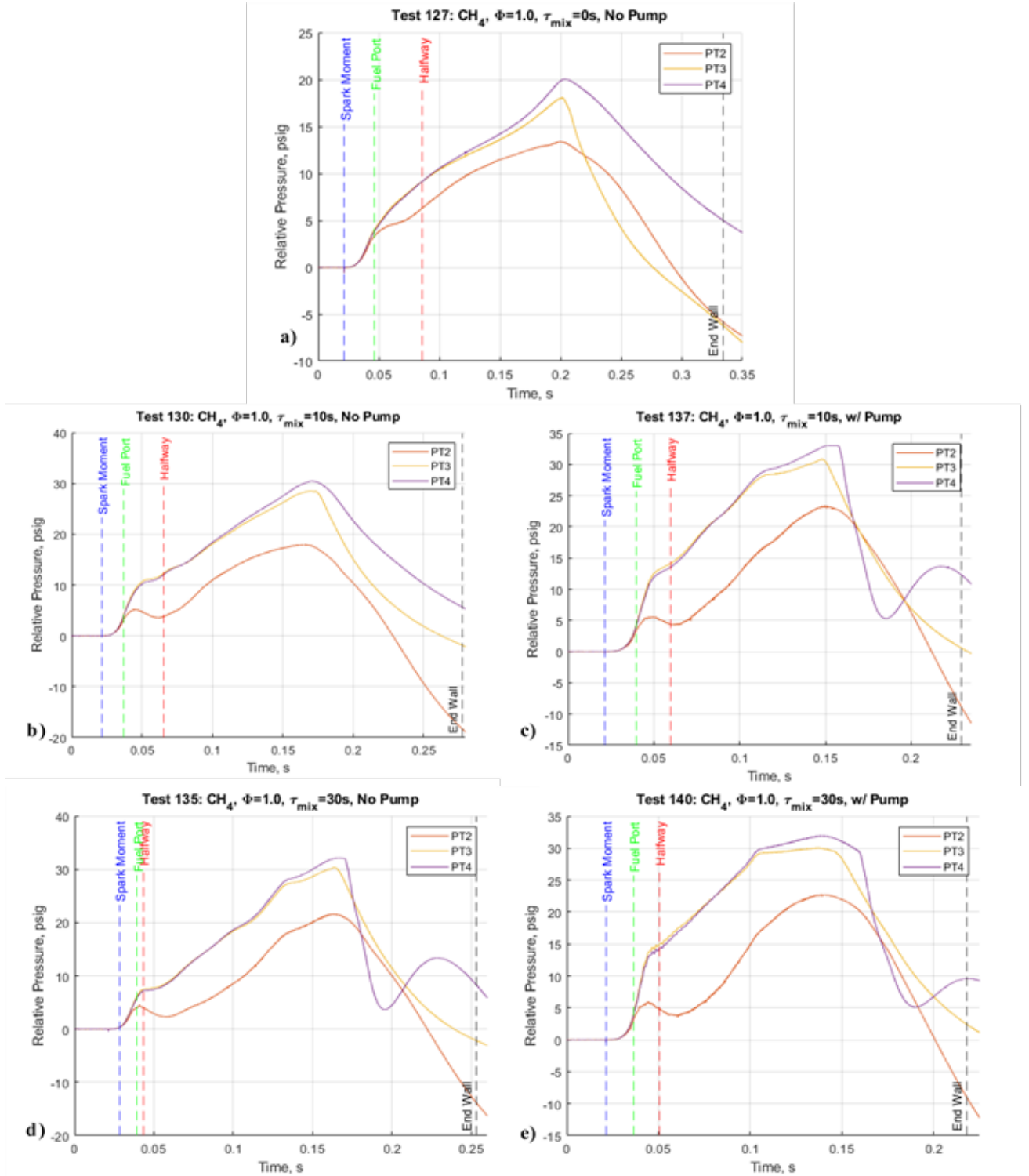


Figure 3.11. Pressure history plots for five methane ($\Phi=1$) test cases: a) Trial 127: $\tau_{\text{mix}}=0\text{s}$, no pump; b) Trial 130: $\tau_{\text{mix}}=10\text{s}$, no pump; c) Trial 137: $\tau_{\text{mix}}=10\text{s}$, pump; d) Trial 135: $\tau_{\text{mix}}=30\text{s}$, no pump; e) Trial 140: $\tau_{\text{mix}}=30\text{s}$, pump.

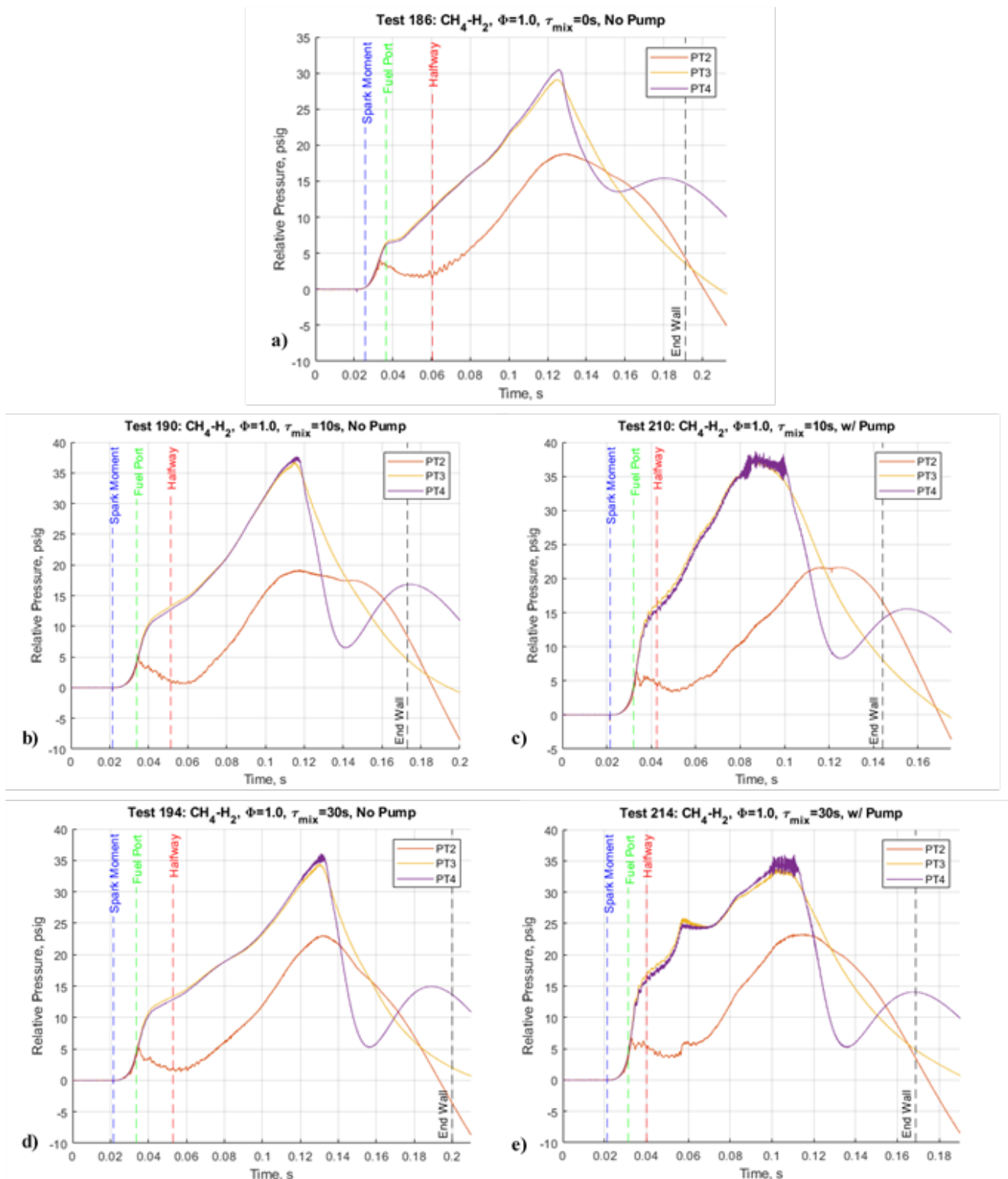


Figure 3.12. Pressure history plots for five 50%-50% methane-hydrogen ($\Phi=1$) test cases: a) Trial 186: $\tau_{\text{mix}}=0\text{s}$, no pump; b) Trial 190: $\tau_{\text{mix}}=10\text{s}$, no pump; c) Trial 210: $\tau_{\text{mix}}=10\text{s}$, pump; d) Trial 194: $\tau_{\text{mix}}=30\text{s}$, no pump; e) Trial 214: $\tau_{\text{mix}}=30\text{s}$, pump.

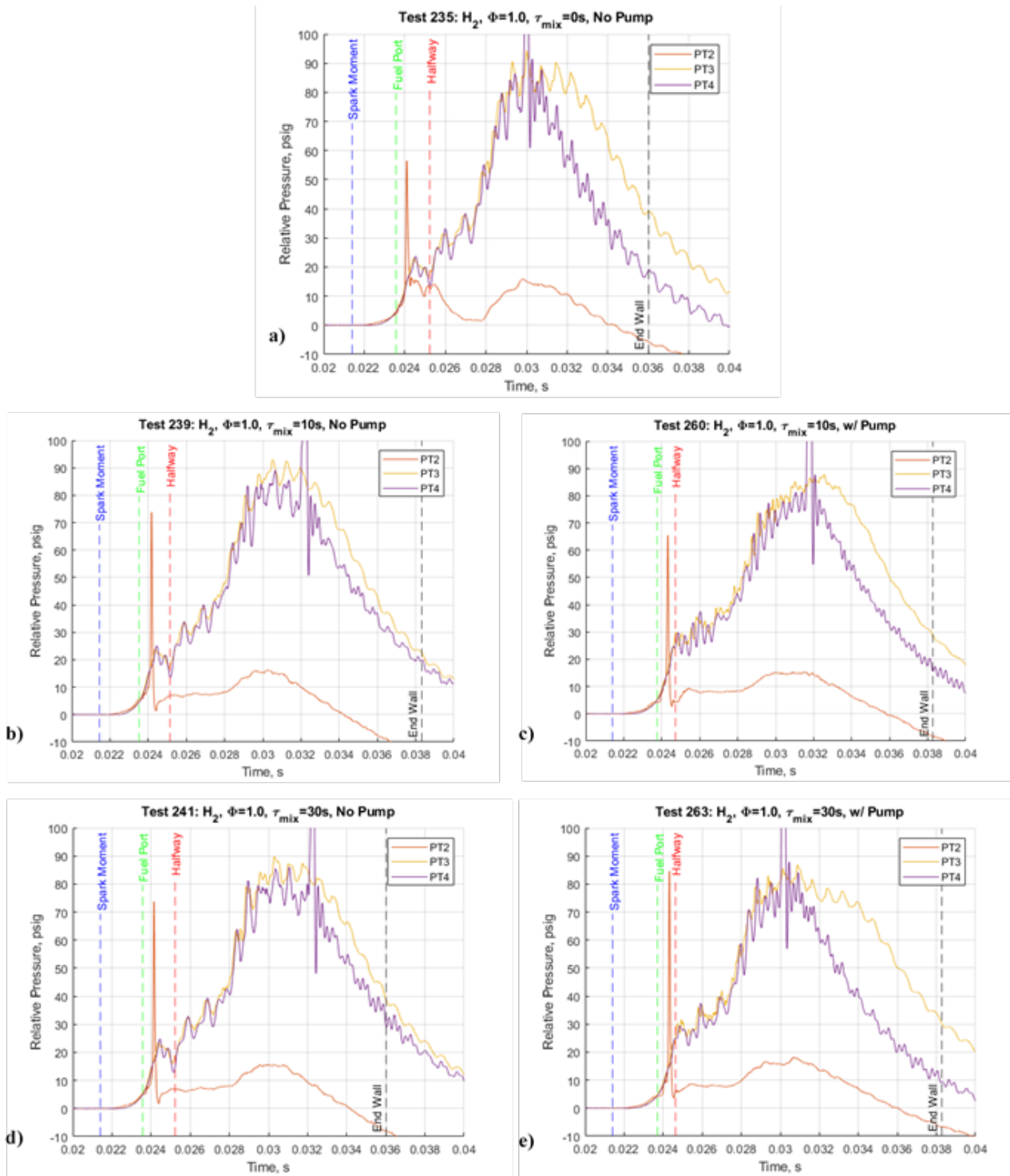


Figure 3.13. Pressure history plots for five hydrogen ($\Phi=1$) test cases: a) Trial 235: $\tau_{mix}=0s$, no pump; b) Trial 239: $\tau_{mix}=10s$, no pump; c) Trial 260: $\tau_{mix}=10s$, pump; d) Trial 241: $\tau_{mix}=30s$, no pump; e) Trial 263: $\tau_{mix}=30s$, pump.

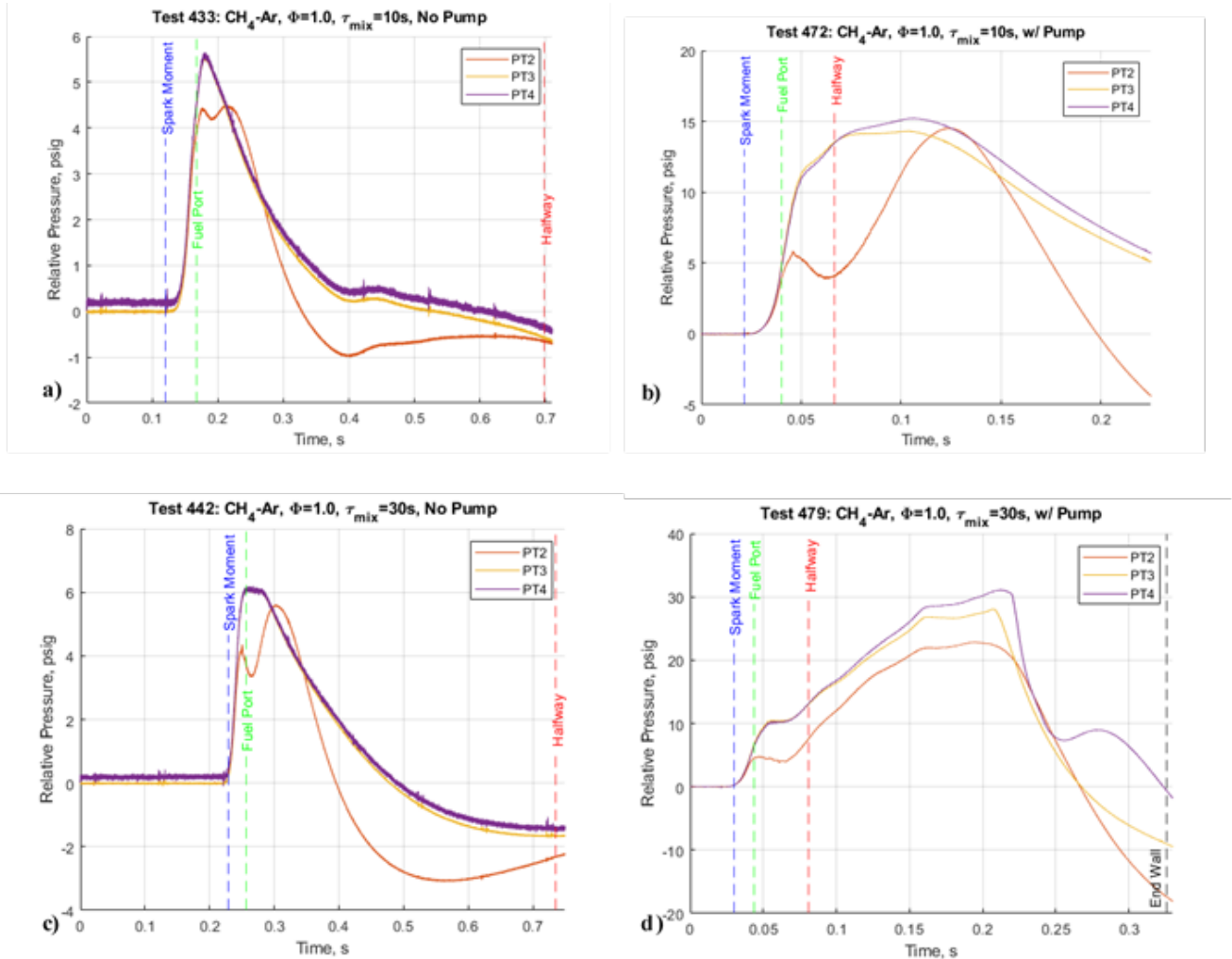


Figure 3.14. Pressure history plots for four 46.4%-56.3% methane-argon ($\Phi=1$) test cases: a) Trial 433: $\tau_{mix} = 10s$, no pump; b) Trial 472: $\tau_{mix} = 10s$, pump; c) Trial 442: $\tau_{mix} = 30s$, no pump; d) Trial 479: $\tau_{mix} = 30s$, pump.

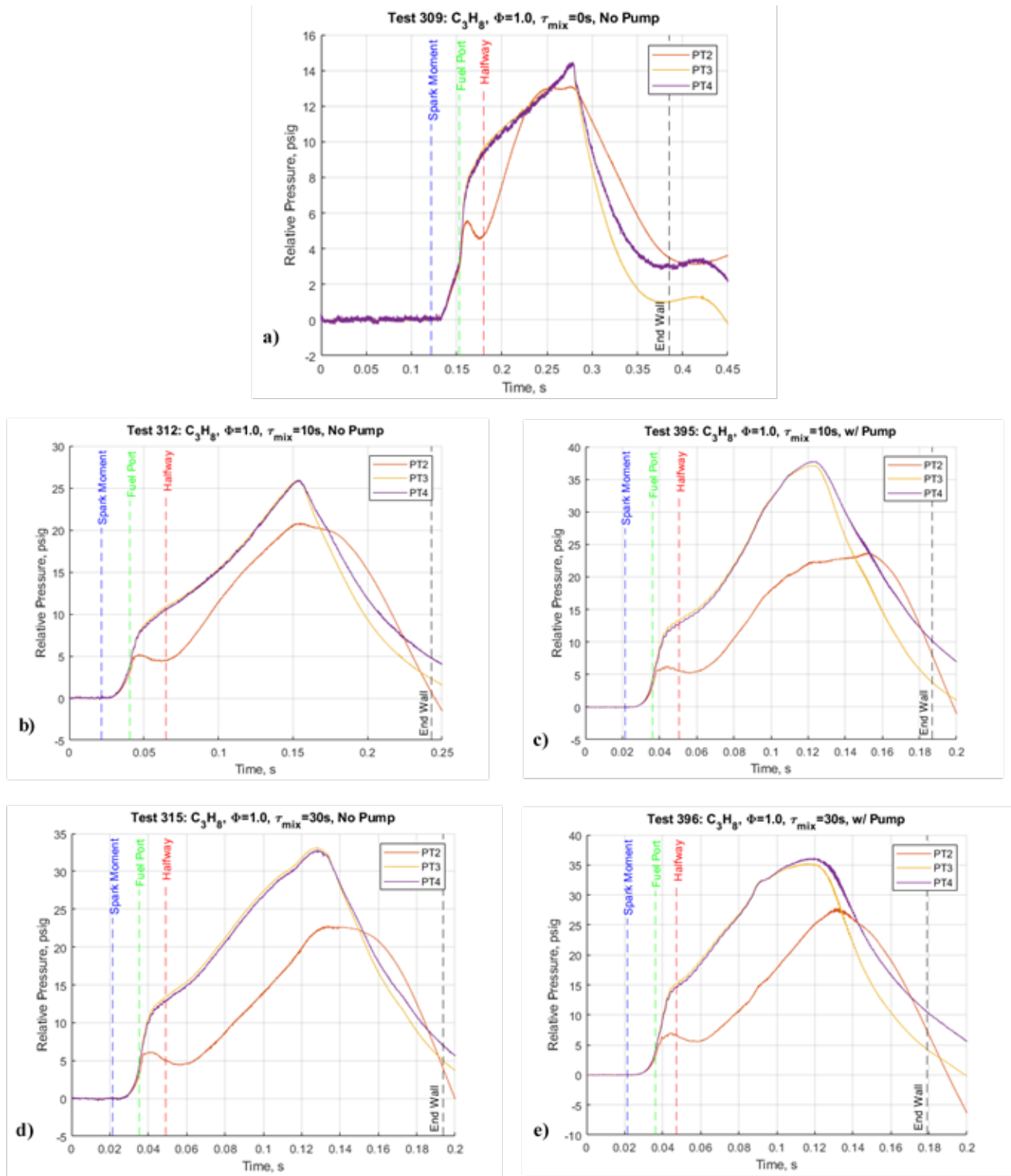


Figure 3.15. Pressure history plots for five propane ($\Phi=1$) test cases: a) Trial 309: $\tau_{mix}=0s$, no pump; b) Trial 312: $\tau_{mix}=10s$, no pump; c) Trial 395: $\tau_{mix}=10s$, pump; d) Trial 315: $\tau_{mix}=30s$, no pump; e) Trial 396: $\tau_{mix}=30s$, pump.

3.1.3 Maximum Pressure Comparisons

As a follow-up to the last point regarding the range of pressures increasing due to increased mixing, Figs. 3.16-3.20 feature the maximum pressures achieved by methane, methane-hydrogen, hydrogen, methane-argon, and propane, respectively. Additionally, Figs. 3.21 and 3.22 depict the combined plots for each of these fuels, with Fig. 3.21 showing all of the data and 3.22 only showing the 0s no-pumping, 30s diffusion, and 30s pumping cases. This data shows that, while not always having a consistent effect on the maximum pressures experienced in the main chamber, the difference is still there, and it is something worth considering. For some fuels, like methane-hydrogen (Fig. 3.17) and pure hydrogen (Fig. 3.18), the differences are small, but in less reactive fuels such as methane (Fig. 3.16), methane-argon (Fig. 3.19), and propane (Fig. 3.20), the differences can be significant. This just further extends the point made previously that these differences are not negligible and should be accounted for one way or another.

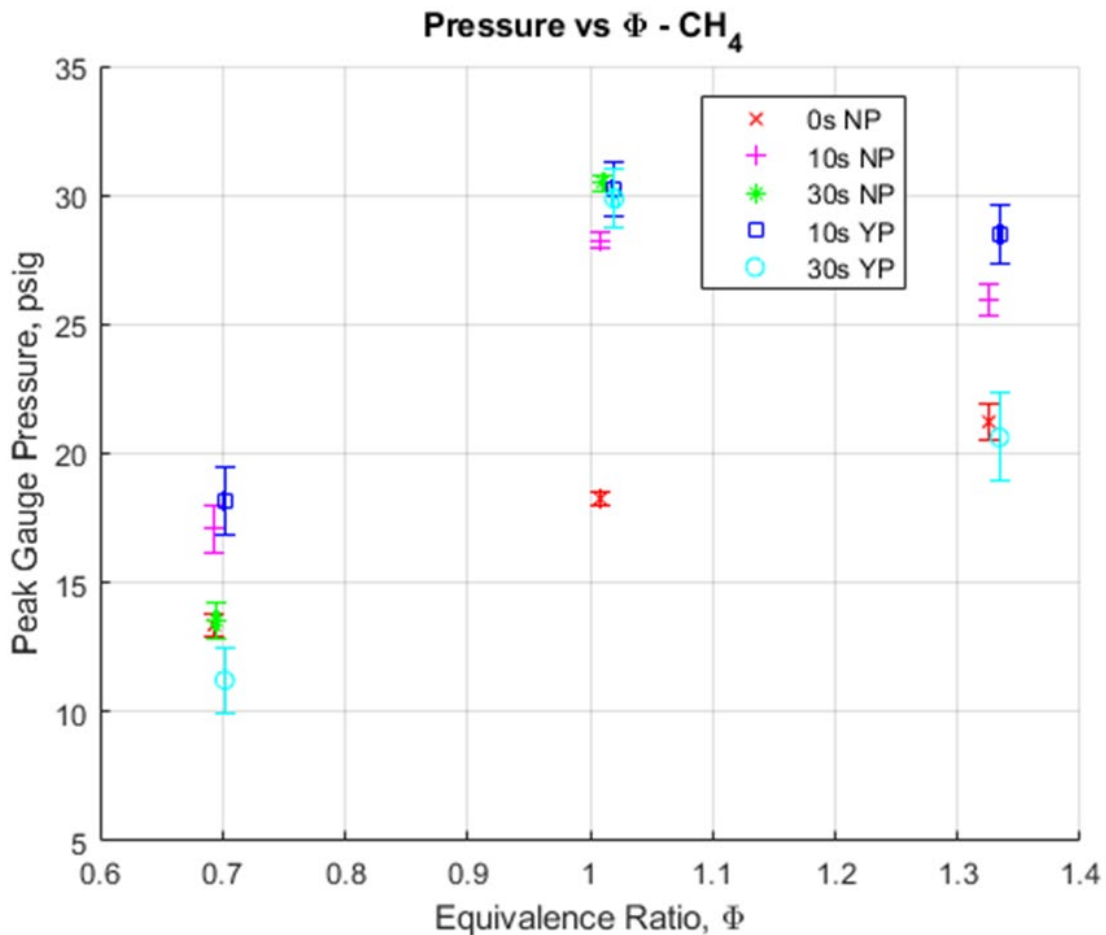


Figure 3.16. Maximum gauge pressure vs equivalence ratio for methane.

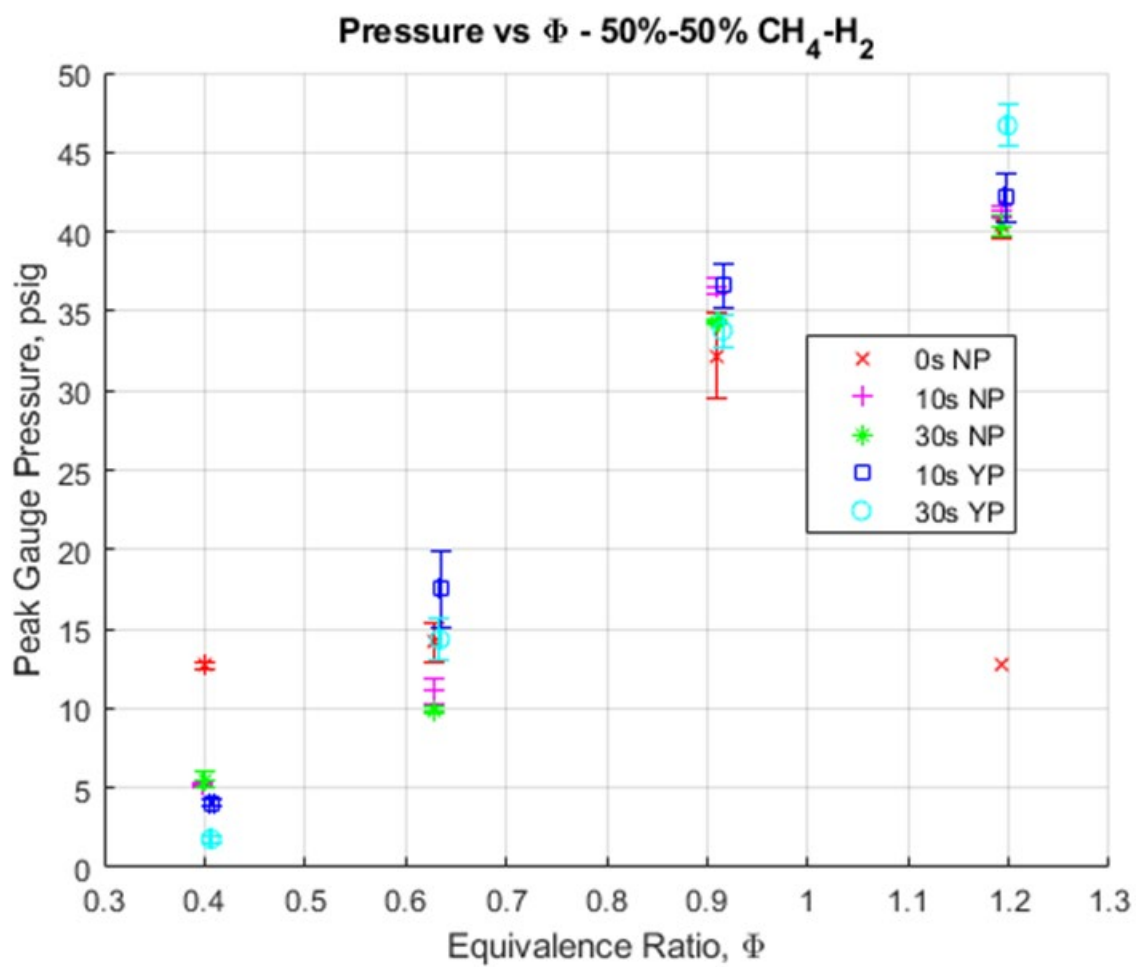


Figure 3.17. Maximum gauge pressure vs equivalence ratio for methane-hydrogen.

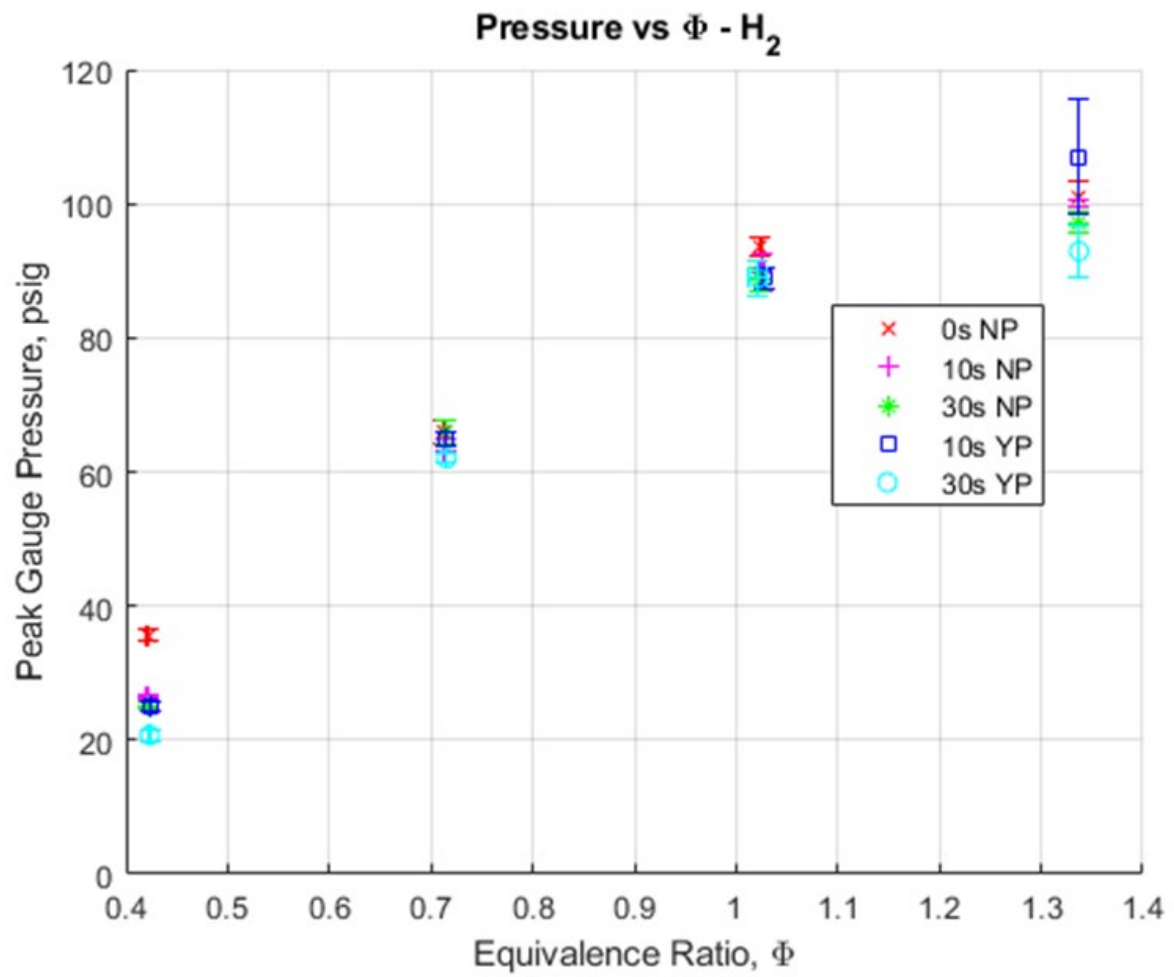


Figure 3.18. Maximum gauge pressure vs equivalence ratio for hydrogen.

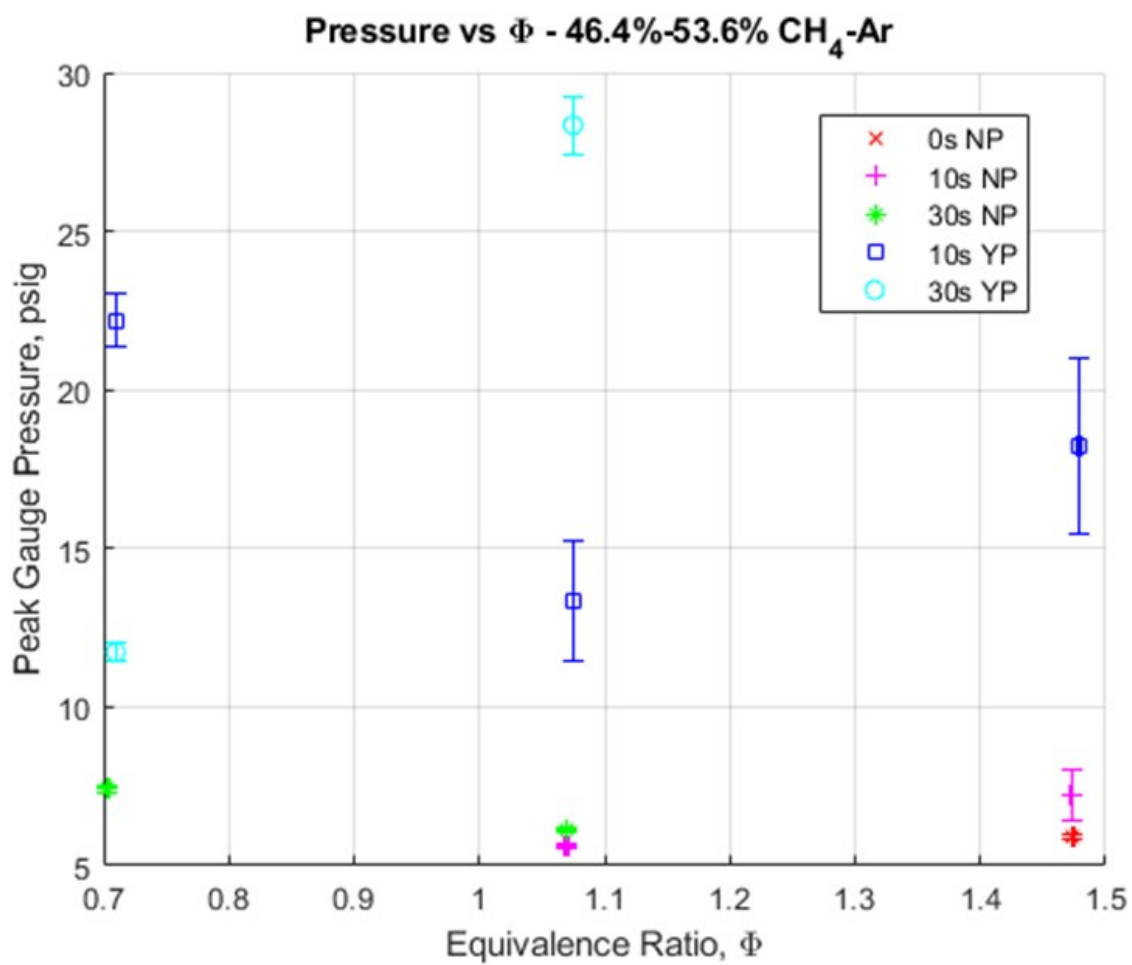


Figure 3.19. Maximum gauge pressure vs equivalence ratio for methane-argon

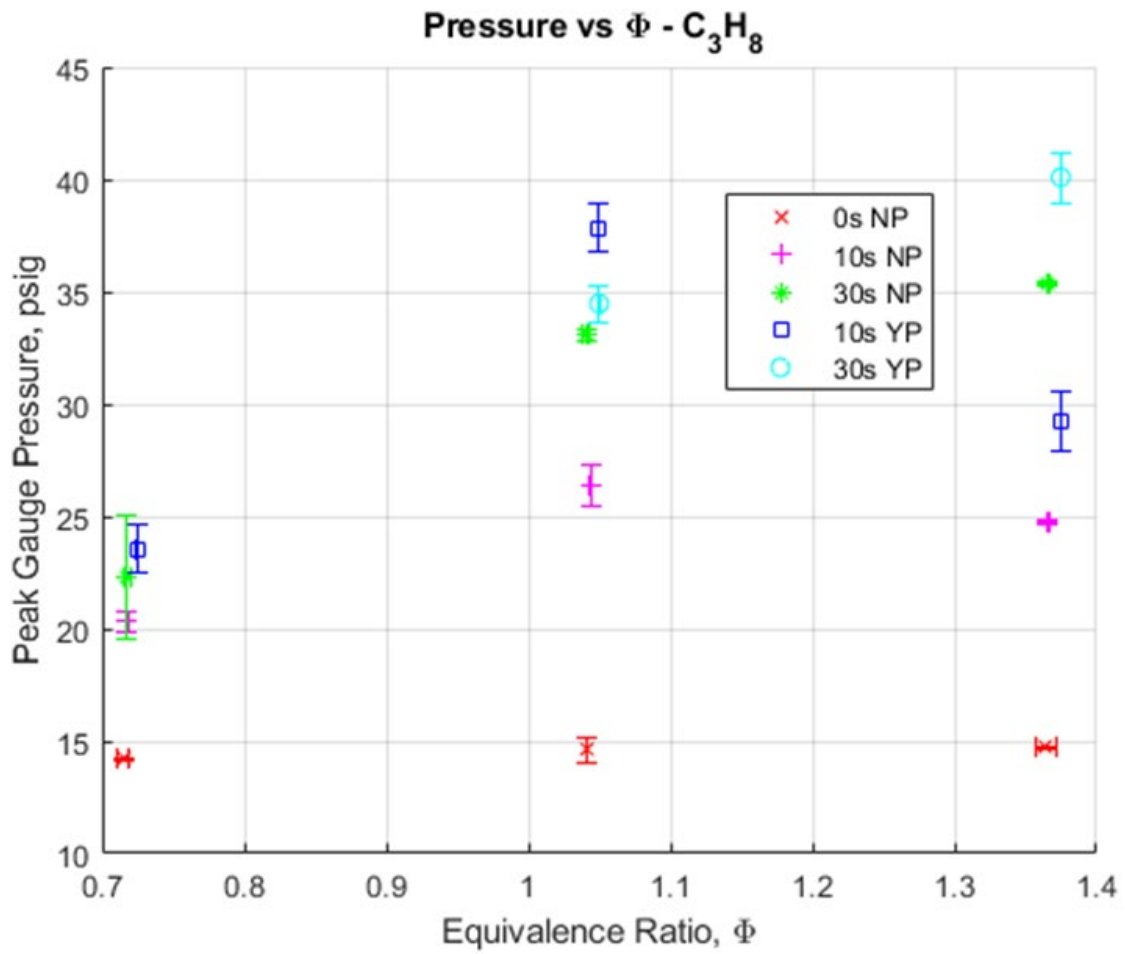


Figure 3.20. Maximum gauge pressure vs equivalence ratio for propane.

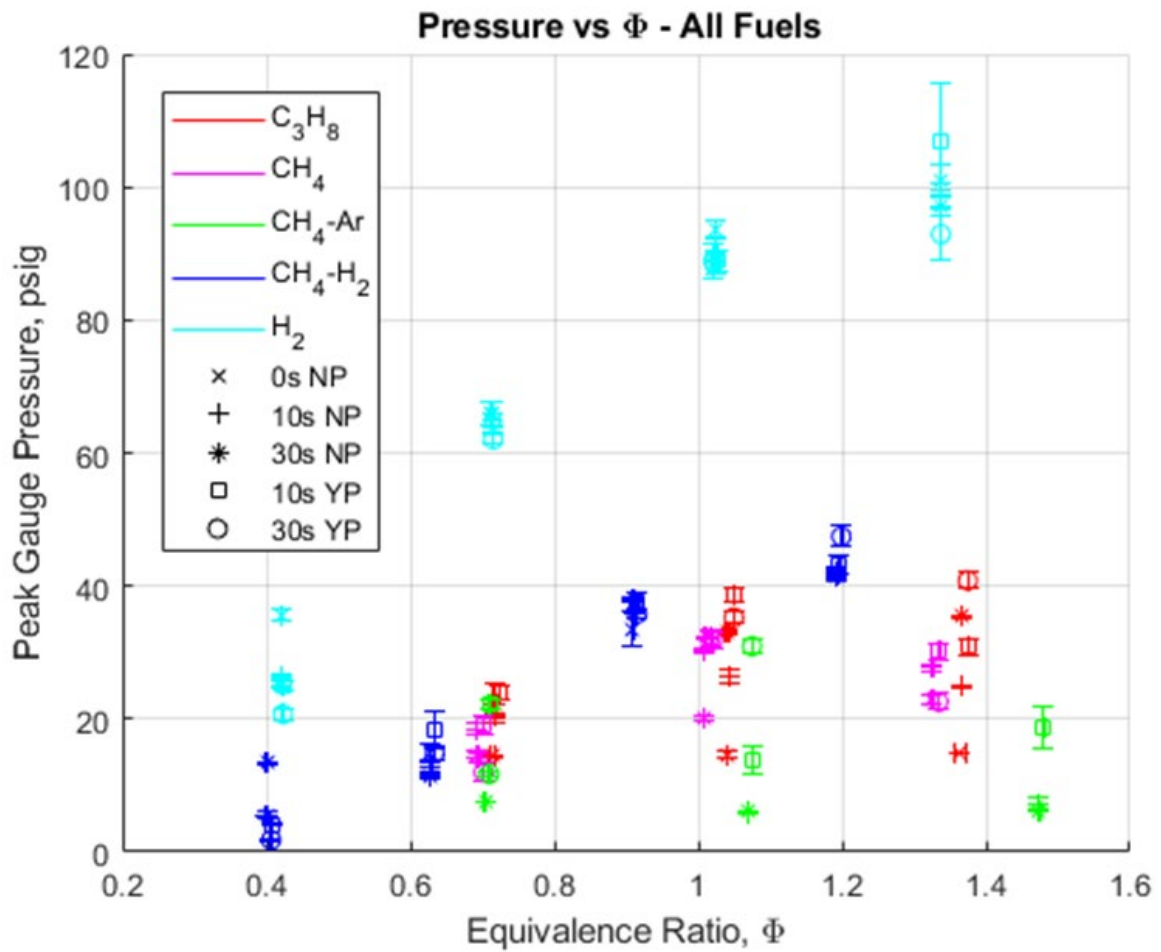


Figure 3.21. Maximum gauge pressure vs equivalence ratio for all of the spark flame data.

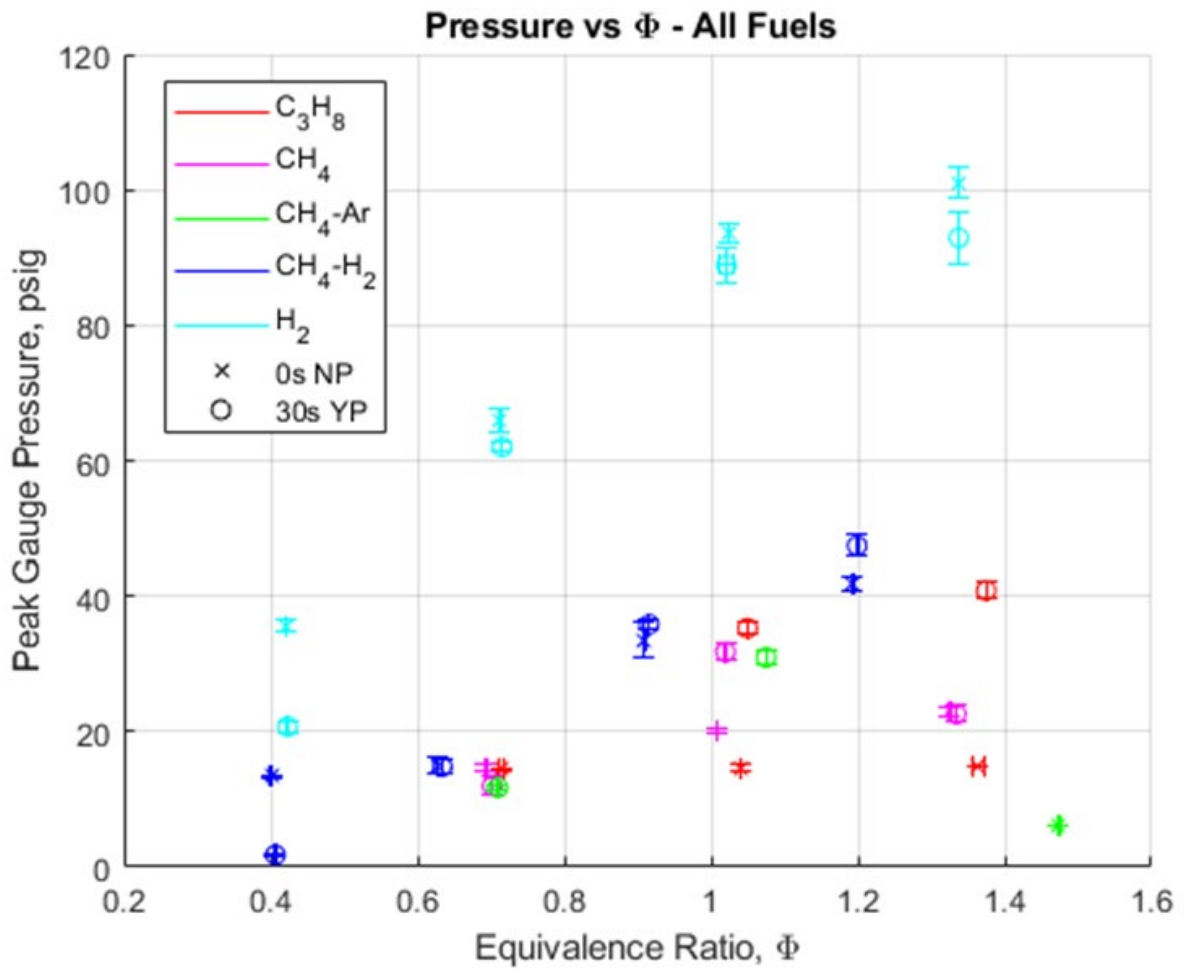


Figure 3.22. Maximum gauge pressure vs equivalence ratio for 0s, no pump (NP); 30s, no pump (NP); and 30s, pump (YP) spark flame data.

3.2 Stationary Hot Jet Ignition Experiments

This subsection describes the results obtained during the stationary hot jet ignition experiments. These experiments were conducted as an extension of the previous work performed by Chowdhury as well as all the other graduate students who studied ignition delay time from stationary jet ignition cases. With the new pump system, quantitative data (e.g., delay times, shock speeds, and pressure values) between cases in which no pumping occurred (as done by previous lab researchers) and those in which 30s of pumping occurred are compared to see if there is any noticeable difference in the results between the two. Some qualitative schlieren and flame luminosity pictures are presented here as well for comparison. As a note, hydrogen is not examined in the cases of ignition delay time and shock speed, for the hydrogen reacts too quickly to be able to determine such information. Additionally, the methane-argon fuel was no longer used in the rest of the experiments because its initial purpose was to be neutrally buoyant and see how stratification was affected. But now that the pump is installed and its effectiveness confirmed, the methane-argon fuel was no longer considered.

3.2.1 Ignition Delay Time

As previously stated, the ignition delay time is the amount of time between the moment of diaphragm rupture/injection of the hot jet of combustion products into the main chamber and the moment of ignition of the main chamber fuel. This time was previously derived a multitude of ways, but it has been refined over the years into a precise evaluation of the pressure history plots and schlieren data. Due to the highly time-resolved nature of the pressure transducers, the diaphragm rupture moment can be calculated simply by finding the moment of sudden pressure rise in both PT2 and PT3 in the pressure plots. Knowing the amount of time between these two rises and the distance these transducers are apart from each other, the shock speed can be calculated. Further, this shock speed can be used to back calculate from the moment of pressure rise to the rupture moment since the distance between the PT3 and the nozzle diaphragm is also known. Therefore, the exact rupture time can be deduced. For the last needed point, the ignition moment can be estimated using the pressure history plots as well, for the flush-mounted PT3 sensor picks up another sudden pressure rise as a result of the ignition moment of the main chamber fuel. This point can be found right where the pressure begins sharply increasing yet again later in the

plot and can be confirmed using the schlieren videos, since the exact time that the ignition kernel appears in the video can be correlated with the estimated time in the pressure plots. One note, however, is that this method – developed by Paik [41] – is only useful if the rupture shockwave is visible in the schlieren video so as to confirm the rupture moment. If not, then there is potential room for error in calculating the rupture moment, and thus the time ignition delay could be off. Therefore, this method only works for experiments with clearly visible shockwaves in the video data. Once these two moments are known, however, the ignition delay time can be calculated by subtracting the rupture moment time from the ignition moment time.

Many of the conclusions drawn by Kojok and Chowdhury have remained true throughout this investigation into ignition delay times in constant-volume combustors. In Fig. 3.26, all of the fuel and mixing conditions (either 0s no pumping or 30s pumping) combinations are displayed in one plot while individual plots in Figs. 3.23-3.25 highlight the methane, methane-hydrogen, and propane cases, respectively. As noted by Chowdhury [42], there is a positive global trend for each fuel's ignition time delay to increase as the equivalence ratio increases as well. Additionally, there is a larger variation in the ignition delays as equivalence ratio increases, and ignition delay is smaller for fuels that are more reactive/contain more hydrogen in their mixture. However, another variation exists here, which is that the ignition time delay tends to decrease after 30s of pumping has occurred. This is more easily seen in the individual fuel plots in Figs. 3.23-3.25. Along with this, the difference between stratified ignition delay times and non-stratified times increases as equivalence ratio increases, which can be seen in the methane (Fig. 3.23) and propane (Fig. 3.25) cases. Methane-hydrogen on the other hand holds a ~2ms difference between the two pumping cases throughout its variations in equivalence ratio. As opposed to Chowdhury's findings that the delay time varied considerably, the 30s pump delay times found in this study typically had little variation. The propane cases in Fig. 3.25 seemed to experience the most deviations between individual cases, but importantly, the variations between the pumping cases tended to be smaller than those between the stratified cases. This seems to backup Chowdhury's predictions that stratification within the chamber influences these times between individual studies.

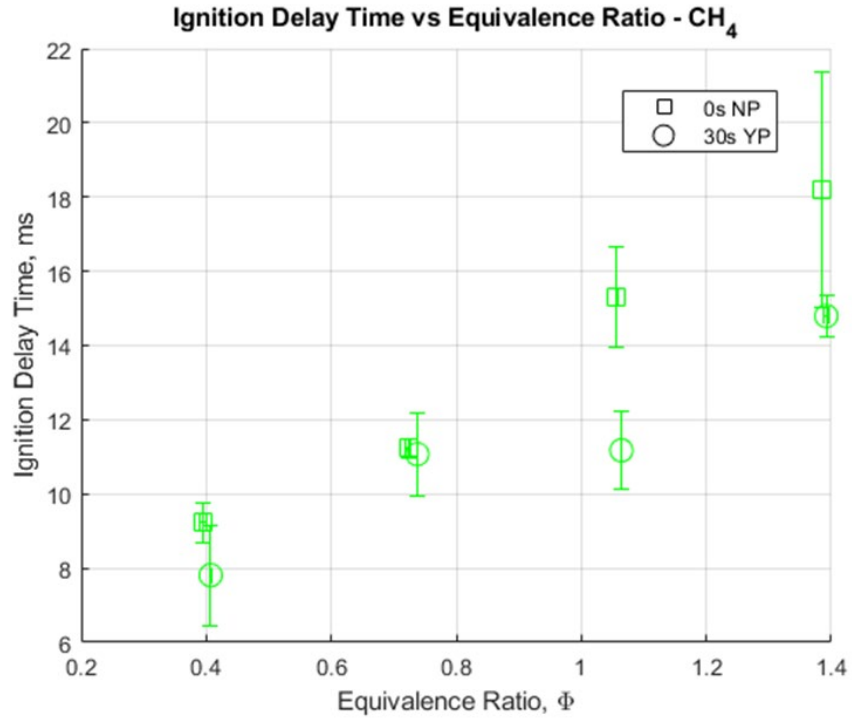


Figure 3.23. Ignition delay time vs equivalence ratio for methane.

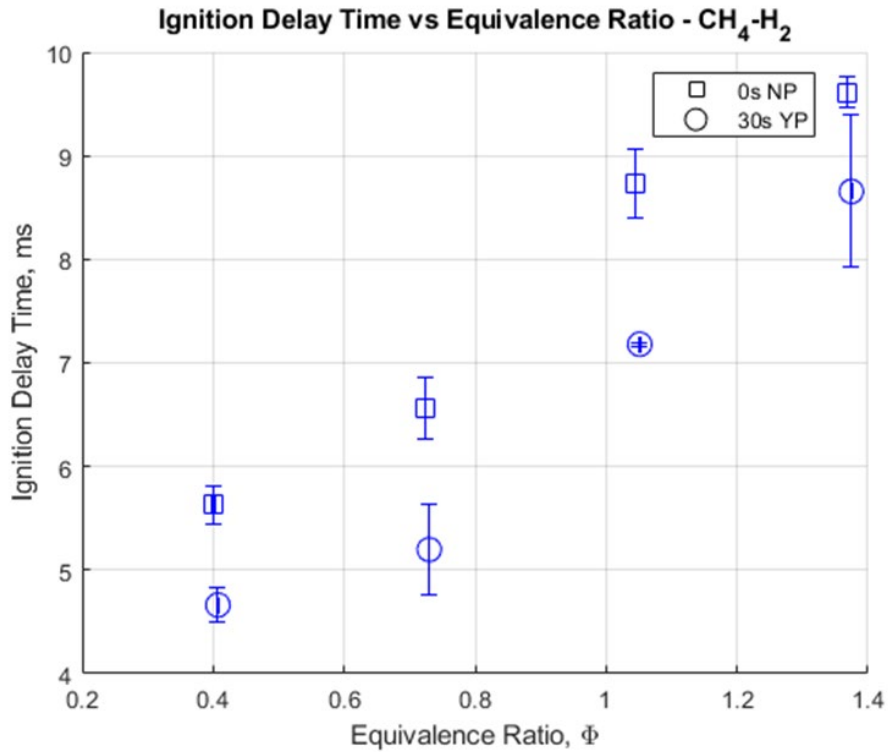


Figure 3.24. Ignition delay time vs equivalence ratio for methane-hydrogen.

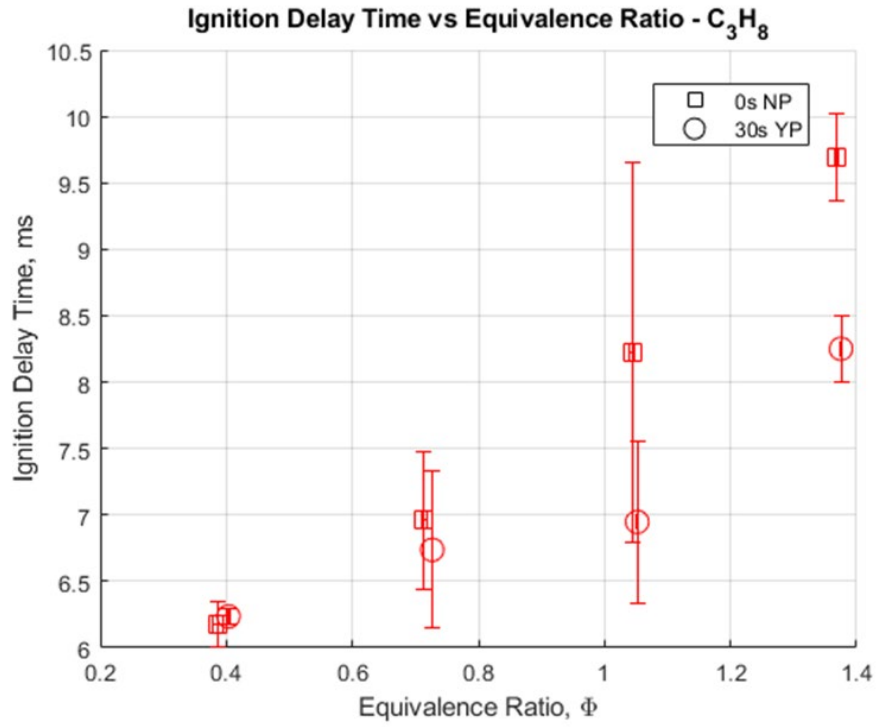


Figure 3.25. Ignition delay time vs equivalence ratio for propane.

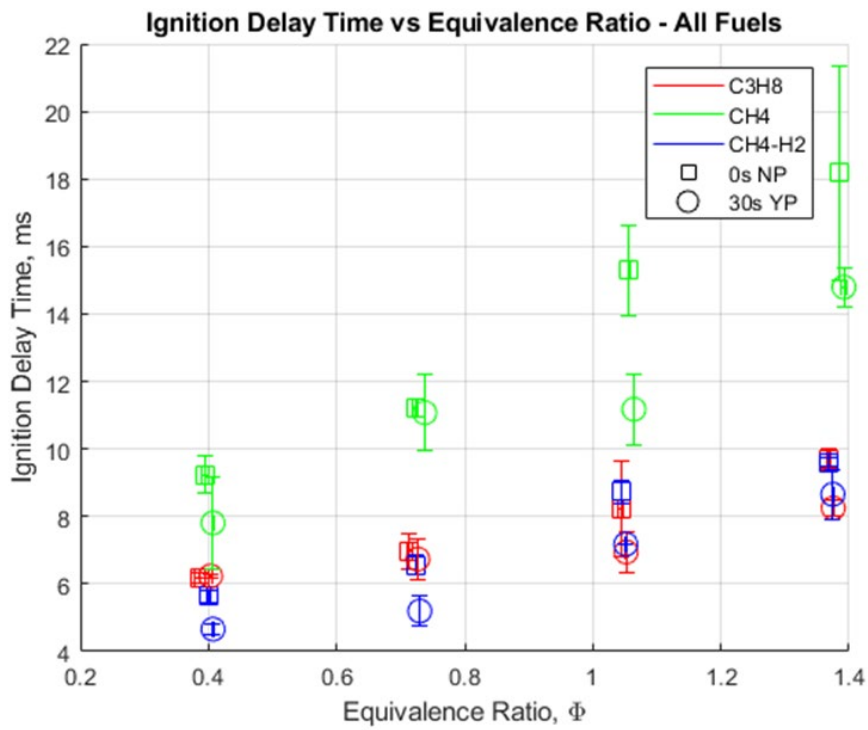


Figure 3.26. Ignition delay time vs equivalence ratio for all stationary jet data.

3.2.2 Shock Wave Speed

Following this thread, the shock speeds within the main chamber also show distinct differences between the stratified and evenly mixed cases, but in the opposite way. Below, Fig. 3.30 shows the shock speed calculations for every fuel used in this study. While Chowdury's experiences still hold up, in that the shock speed has quite a bit of variation between the different fuels and equivalence ratios, there is at least a slight change in shock speed once mixing has been implemented. Since the overall mixture becomes more distributed, there should not be as many variations in the flow that would otherwise slow down the resulting shockwaves. And in fact, that is just the case. This is more easily seen in Figs. 3.27-3.29 that show the shock speeds for methane, methane-hydrogen, and propane. The pump cases had slightly faster shock speeds than the non-pump cases; however, the pump cases experienced greater amounts of variation, like in the case of propane in Fig. 3.29.

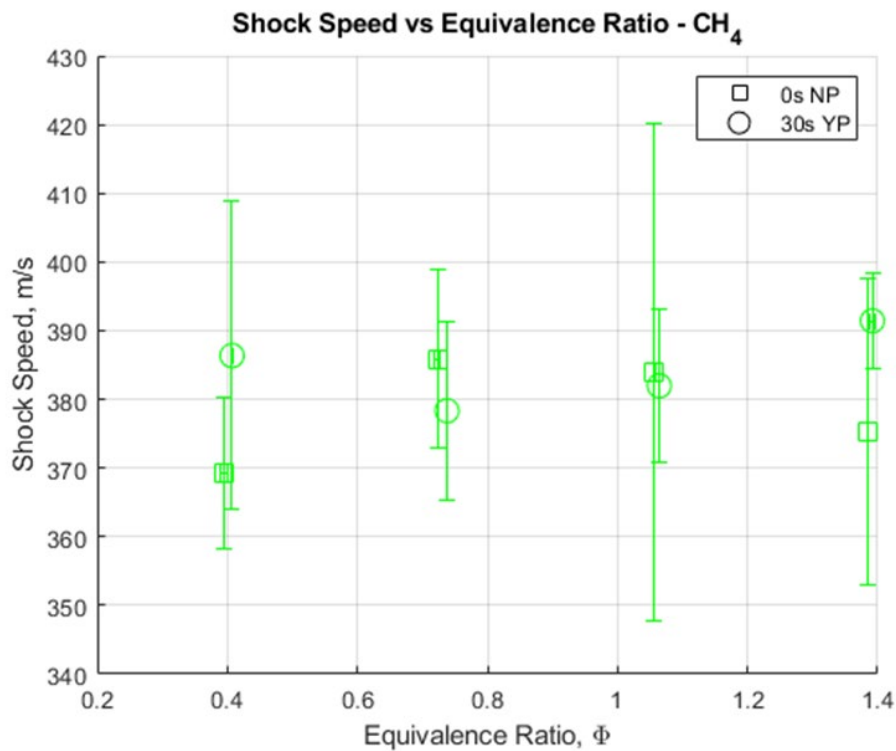


Figure 3.27. Shock speed vs equivalence ratio for methane.

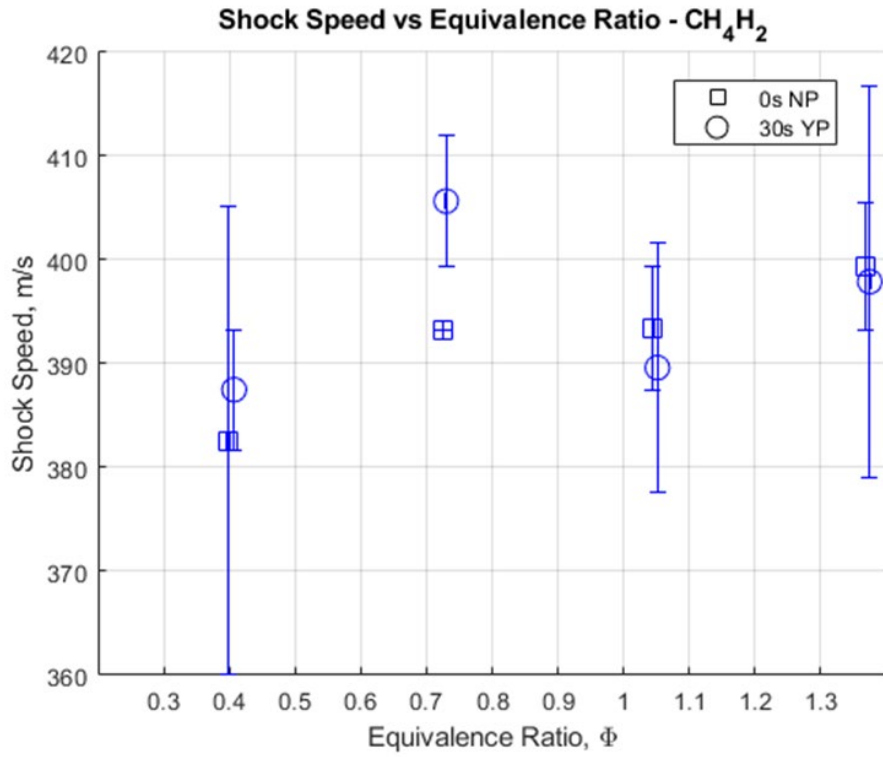


Figure 3.28. Shock speed vs equivalence ratio for methane-hydrogen.

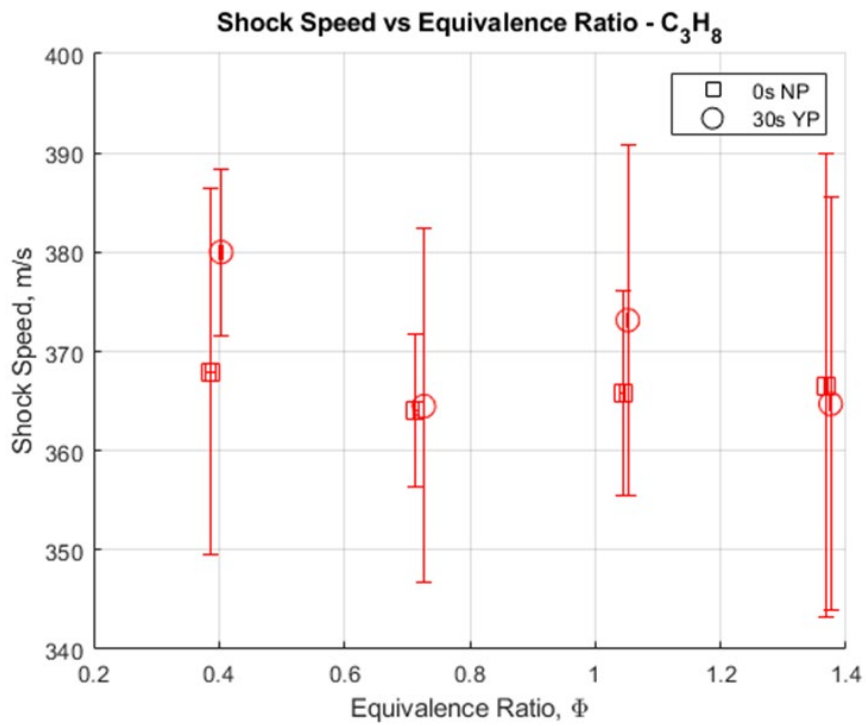


Figure 3.29. Shock speed vs equivalence ratio for propane.

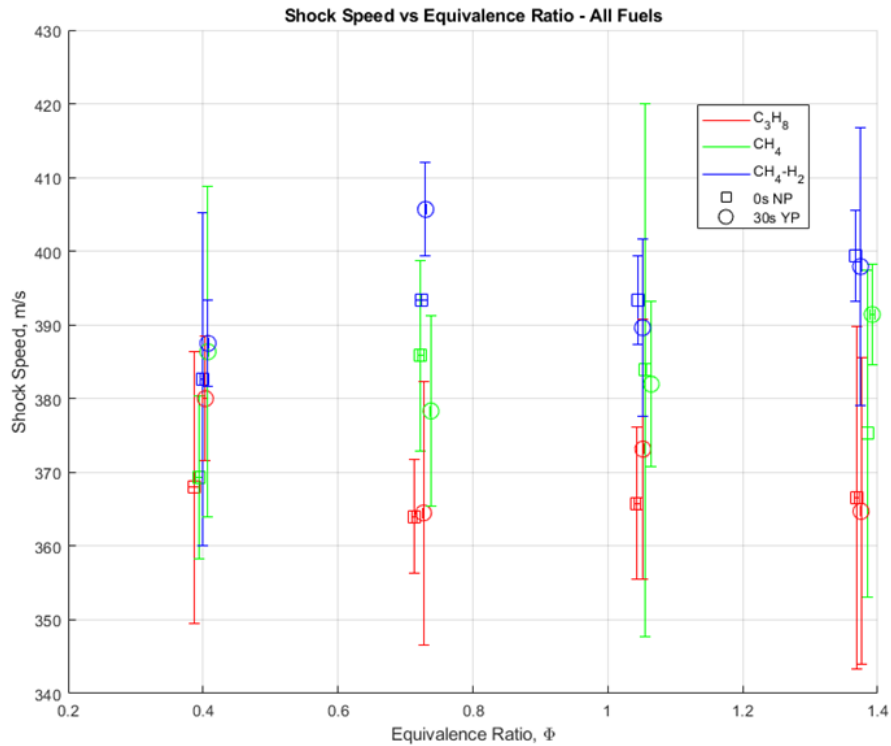


Figure 3.30. Shock speed vs equivalence ratio for all stationary jet data.

3.2.3 Pressure Data Comparisons

Similar to the pressure history plots in Sect. 3.1, the pressure history plots below in Figs. 3.31-3.34 feature moments of interest in the combustion event, such as the rupture moment, and ignition moment. Found in these figures, each fuel tended to have one of two reactions in their pressure histories between the mixed and unmixed cases. Previously, a distinct broadening of the peak occurred in each fuel's pressure profile as the mixture was more evenly distributed. However, in the case of stationary hot jet ignition cases, the pressure histories really had little change between them. While methane and methane-hydrogen fuels did show a marginally broader peak for the 30s pump cases (as seen in Figs. 3.31b and 3.32b), the pure hydrogen and propane cases see a narrowing of their peaks (Figs. 3.32 and 3.34). It is unknown why this is, but perhaps it has to do with these fuels being most and least dense fuels examined in this study, respectively. One last similarity that still holds up in these plots, however, is that the overall combustion time decreased after the pump was used.

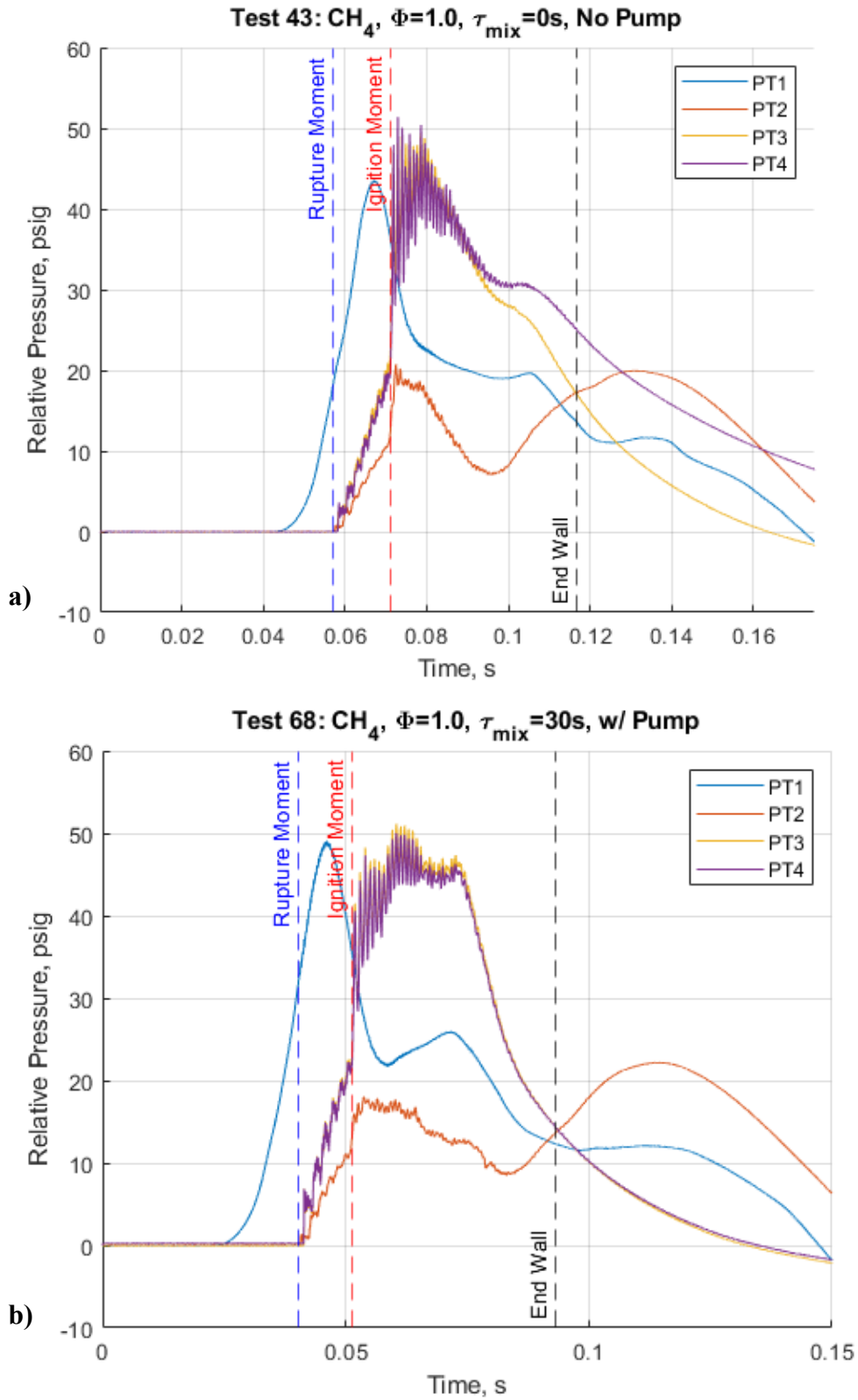


Figure 3.31. Pressure history plots for two methane ($\Phi=1$) stationary cases: a) Trial 43: $\tau_{\text{mix}}=0\text{s}$, no pump; b) Trial 68: $\tau_{\text{mix}}=30\text{s}$, pump.

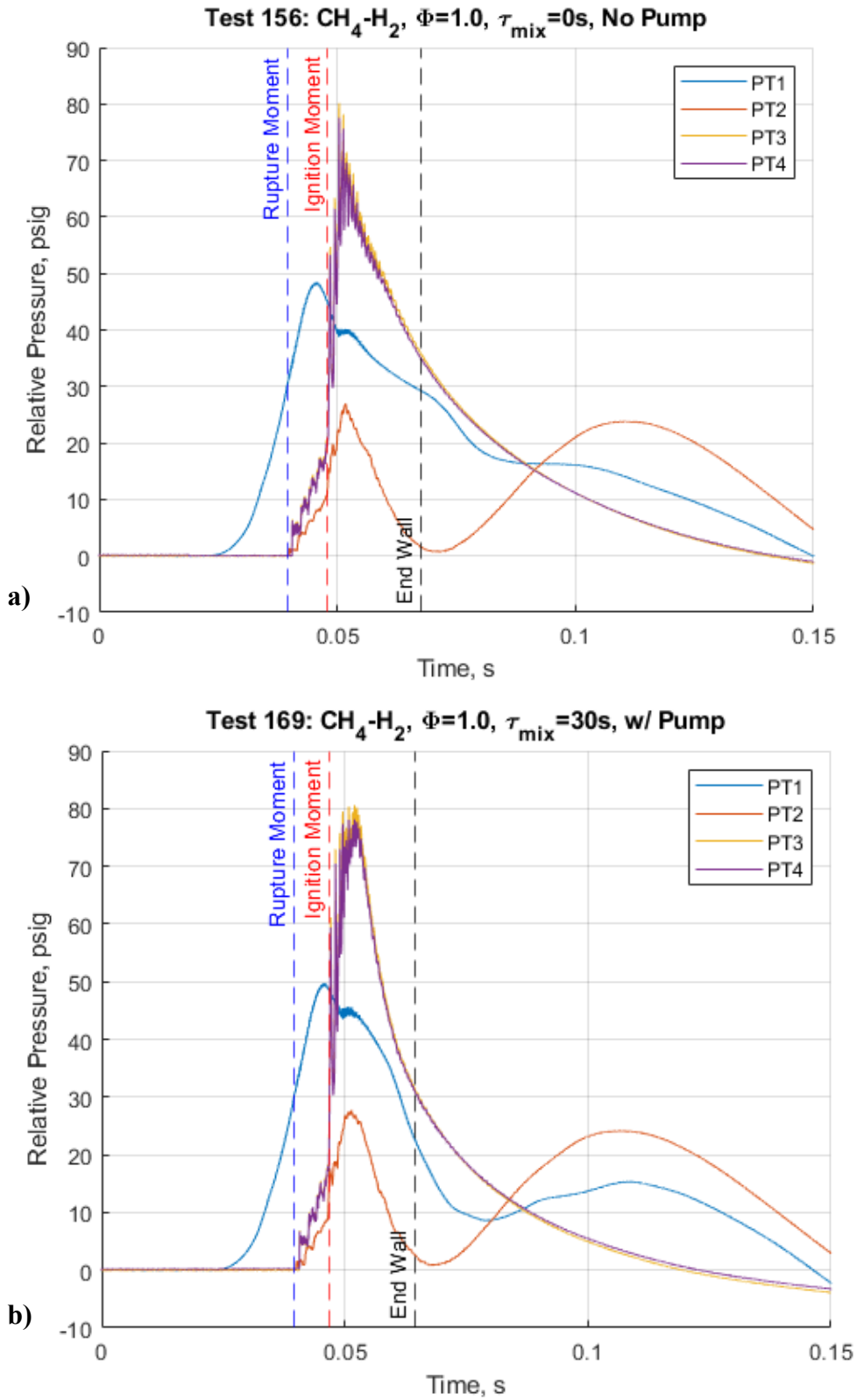


Figure 3.32. Pressure history plots for two 50%-50% methane-hydrogen ($\Phi=1$) stationary cases: a) Trial 156: $\tau_{mix}=0s$, no pump; b) Trial 169: $\tau_{mix}=30s$, pump.

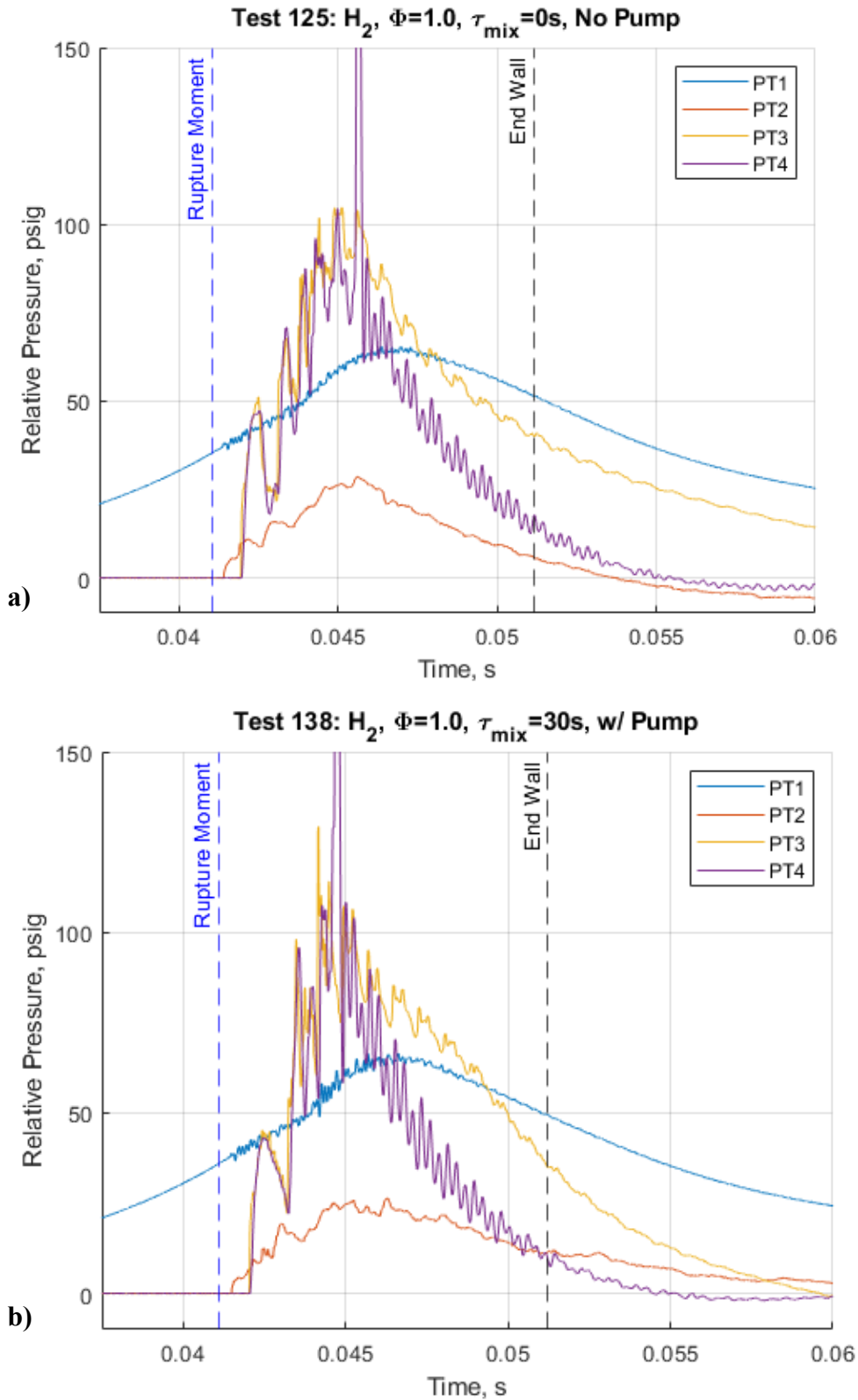


Figure 3.33. Pressure history plots for two hydrogen ($\Phi=1$) stationary cases: a) Trial 125: $\tau_{\text{mix}}=0\text{s}$, no pump; b) Trial 138: $\tau_{\text{mix}}=30\text{s}$, pump.

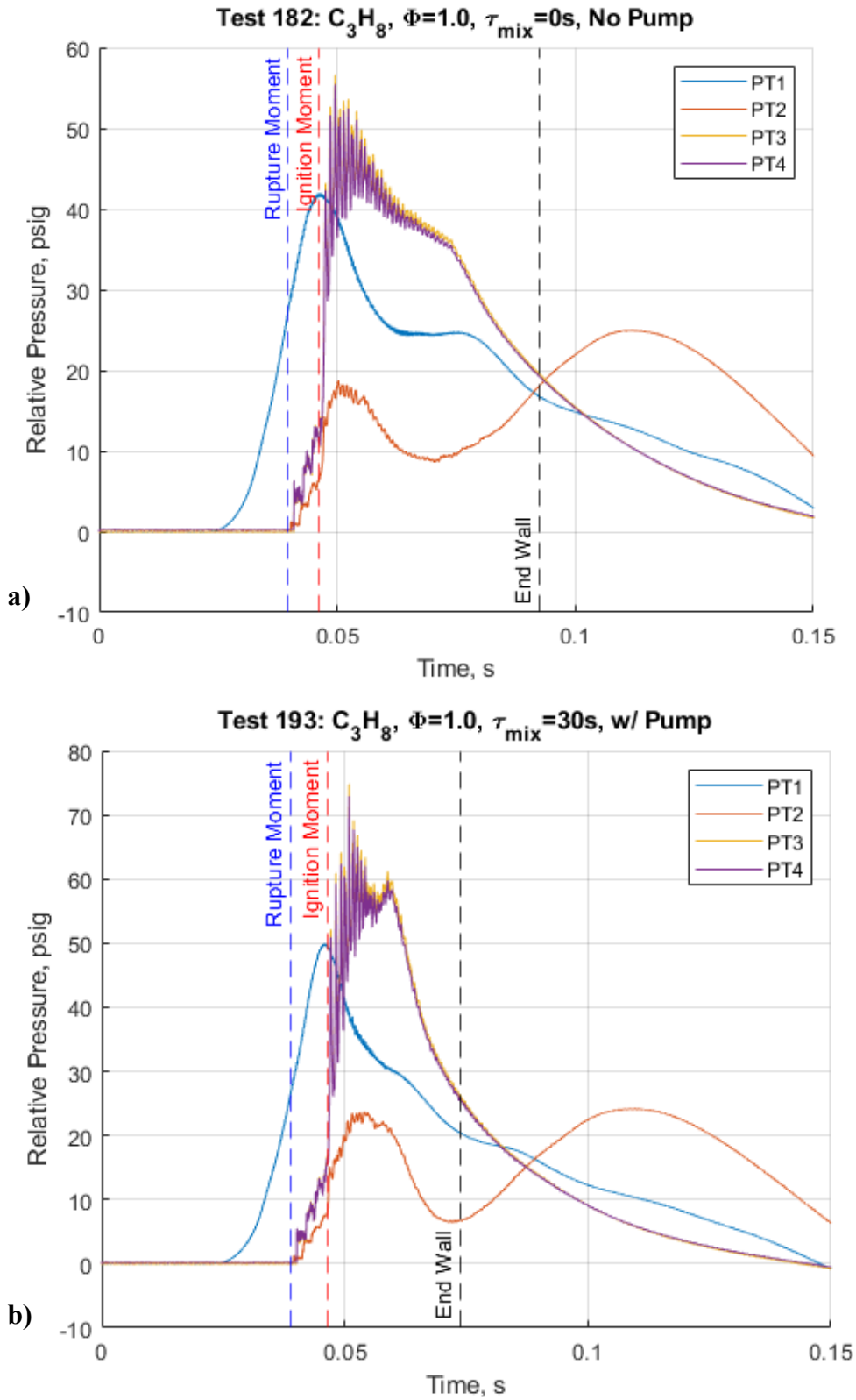


Figure 3.34. Pressure history plots for two propane ($\Phi=1$) stationary cases: a) Trial 182: $\tau_{\text{mix}}=0\text{s}$, no pump; b) Trial 193: $\tau_{\text{mix}}=30\text{s}$, pump.

Moving on, the maximum pressures experienced during these stationary jet cases showed some interesting results. An overall plot between equivalence ratio and maximum pressure for every fuel evaluated in these stationary jet cases can be found in Fig. 3.39, with each fuel represented individually in Figs. 3.35-3.38. Looking at the overall trends, it seems that the same relationships between the fuels remain the same as with the spark flame cases. Overall, maximum pressure tends to increase as the fuel-air mixture becomes richer; however, once past stoichiometric conditions, the maximum pressure can be seen slightly decreasing (or at the least plateauing) for the 1.3 ratio cases. Another point of interest is that the variations in maximum pressure between each fuel become greater with an increasing equivalence ratio as well. Going deeper, the individual fuel plots reveal the effects of stratification on the system. Most notably, while some differences can be found, the well-mixed cases proved to experience greater maximum pressures than the non-mixed cases. At times, the deviations in the averages tended to overlap; however, overall, there were considerable differences between the two test cases.

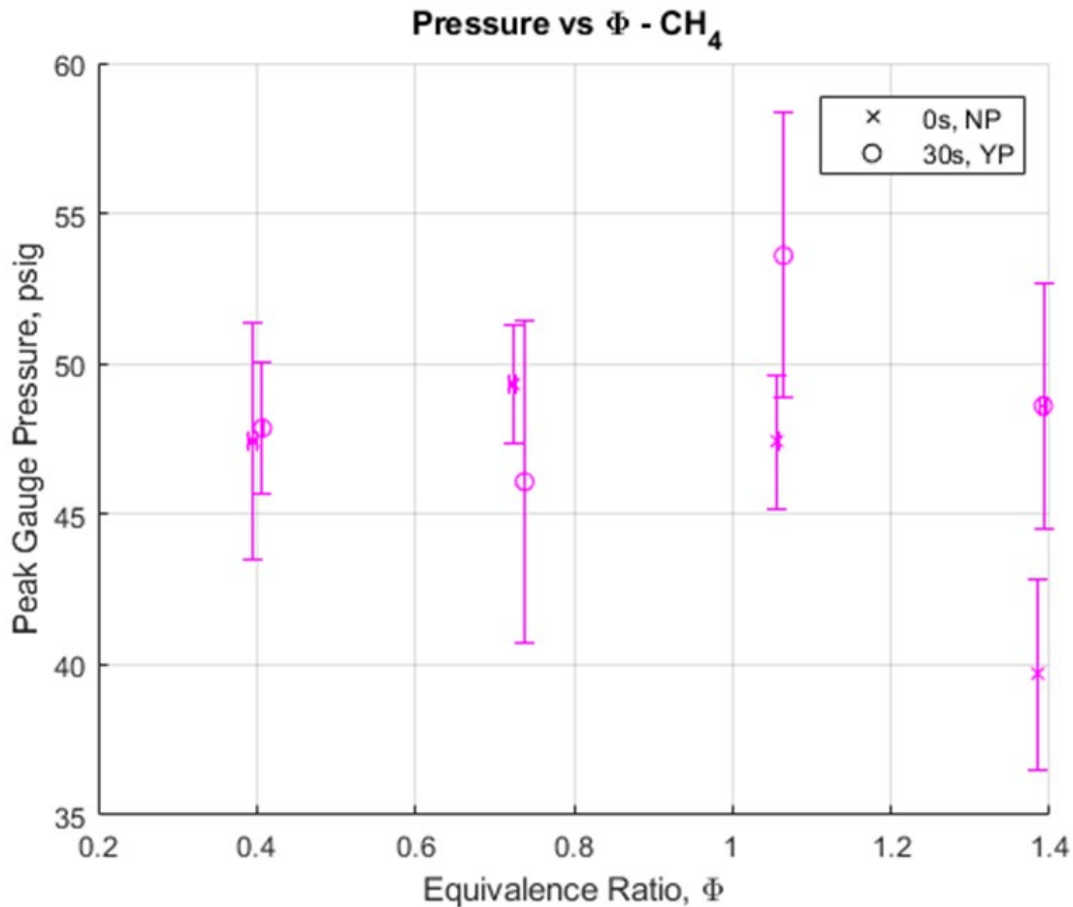


Figure 3.35. Maximum gauge pressure vs equivalence ratio for methane.

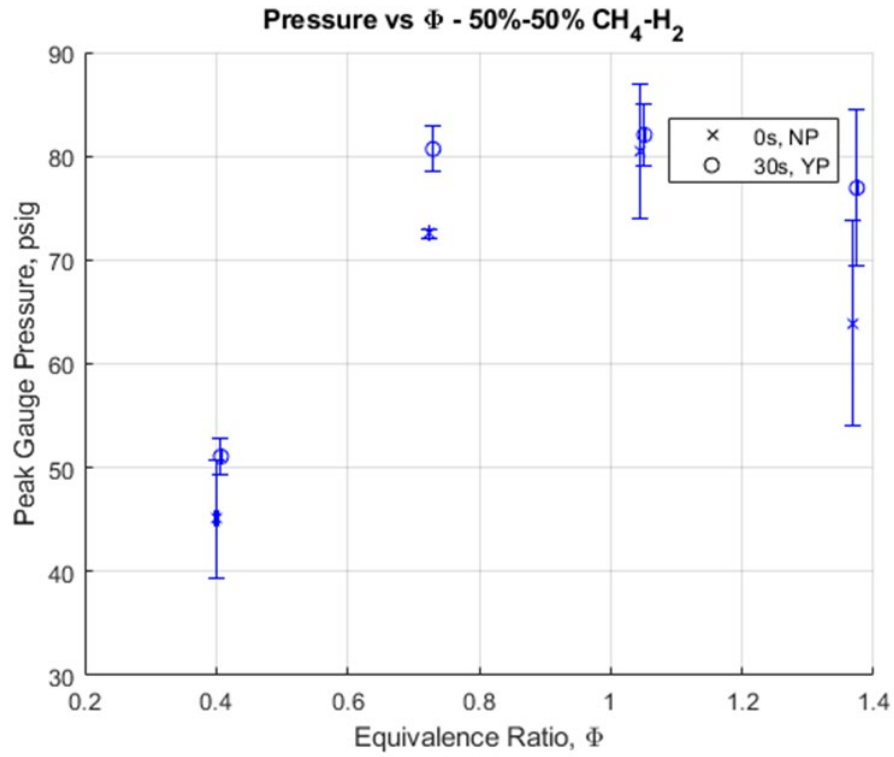


Figure 3.36. Maximum gauge pressure vs equivalence ratio for methane-hydrogen.

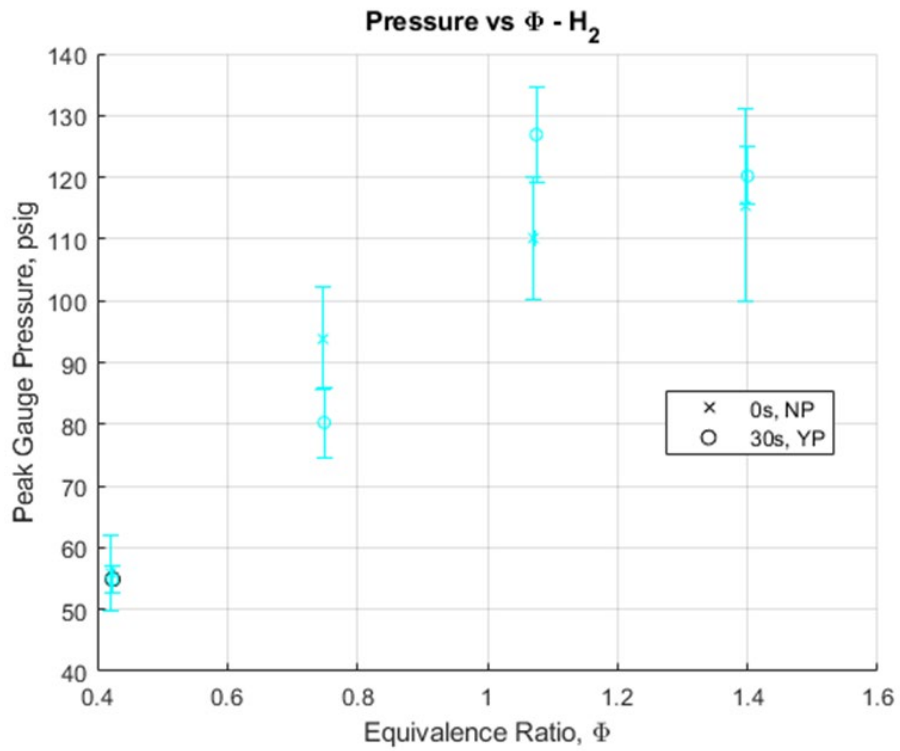


Figure 3.37. Maximum gauge pressure vs equivalence ratio for hydrogen.

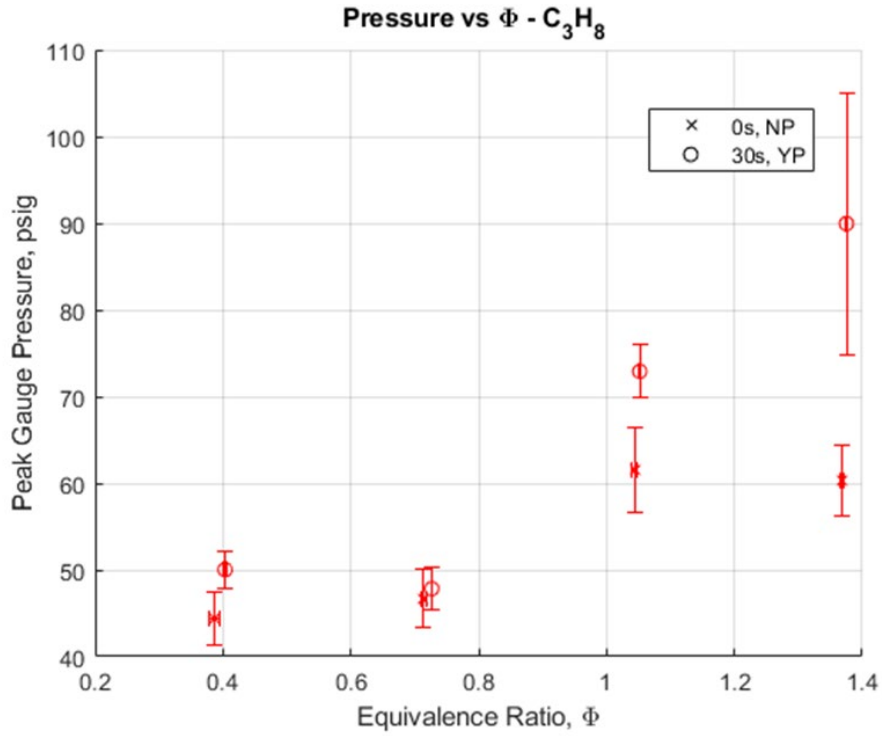


Figure 3.38. Maximum gauge pressure vs equivalence ratio for propane.

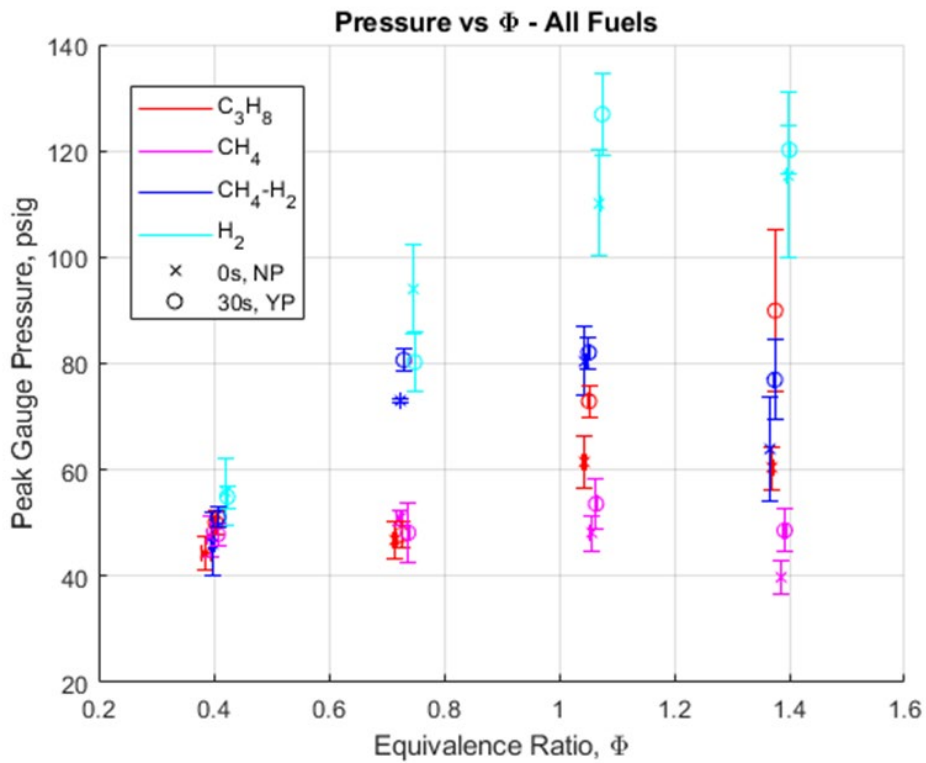


Figure 3.39. Maximum gauge pressure vs equivalence ratio for all stationary data.

3.2.4 Visual Comparisons

The schlieren videos for each case type only further back up the findings made above. Figures 3.40-3.43 show schlieren and flame luminosity images for the pump and non-pump cases side-by-side for the various fuels. The combustion events themselves were much faster than the spark flame experiments, and the jets themselves can barely be seen in the flame luminosity images below. One thing to note, though, is that the jets entering well-mixed fuel-air mixtures visually reach the end of the schlieren window faster than in the unmixed mixtures. This has to do with the same reason the shock speeds increase for the pump cases. Fewer variations in the fuel-air mixture cut down on the shear stresses/friction/drag experienced by the jet upon entering the chamber. As a result, the jets can maintain their speeds for longer and can travel further down in the chamber than in cases where lots of variations in the local equivalence ratios exist. Additionally, the schlieren images seem to show that the time between jet injection and ignition is less for pump cases than non-pump cases, based on the frame moments in which the ignition kernels appear. The flame luminosity images also show that the pump cases tend to be a little less bright and have fewer orange flames than the non-pump cases; this could be a result of evening out the local equivalence ratios throughout the chamber due to pumping, as doing so would decrease the number of regions with rich fuel-air equivalence ratios where such flames tend to occur.

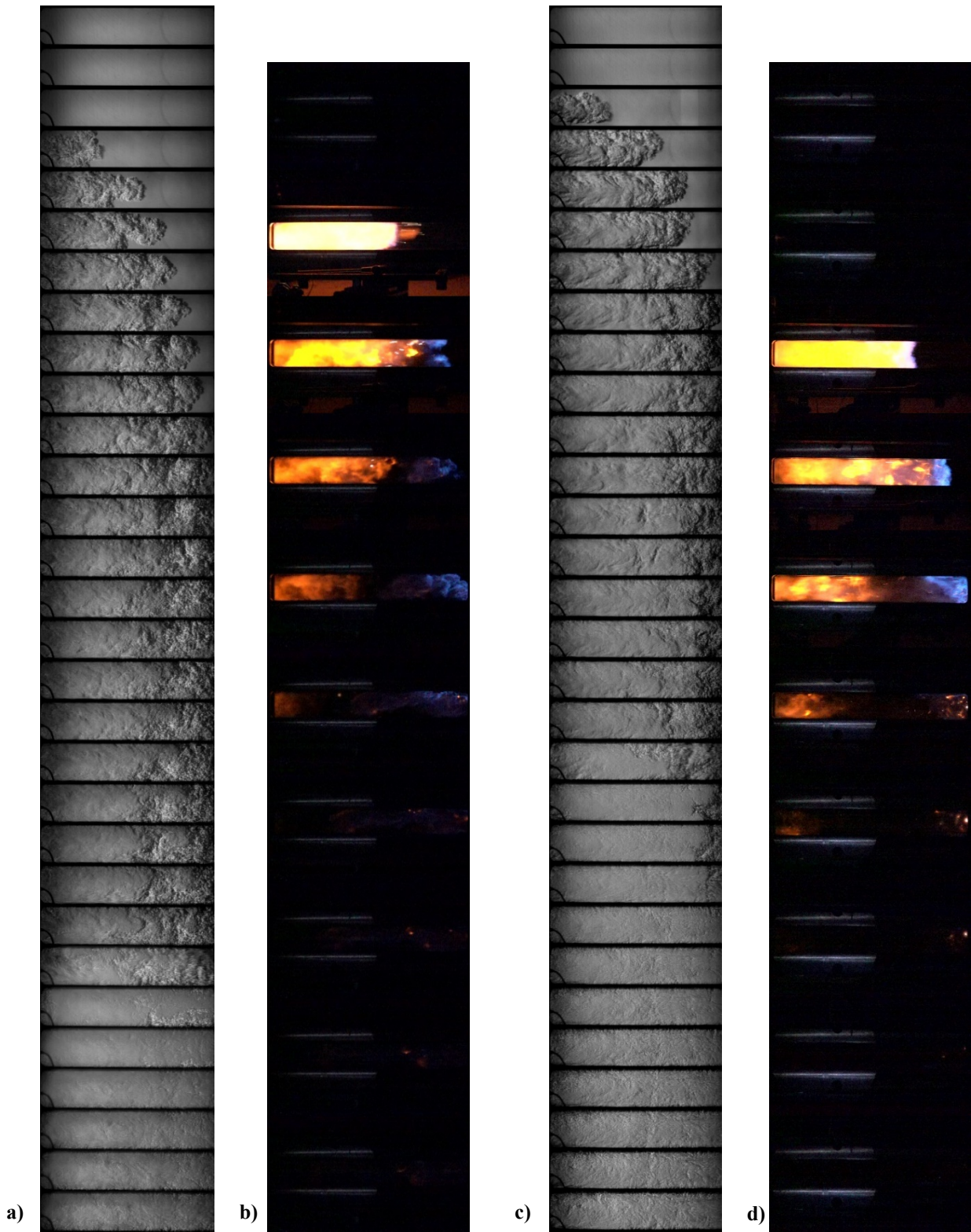


Figure 3.40. Filmstrips for two methane ($\Phi=1$) test cases: a) schlieren and b) flame luminosity for Trial 43: $\tau_{\text{mix}}=0\text{s}$, no pump; c) schlieren and d) flame luminosity for Trial 68: $\tau_{\text{mix}}=30\text{s}$, pump.

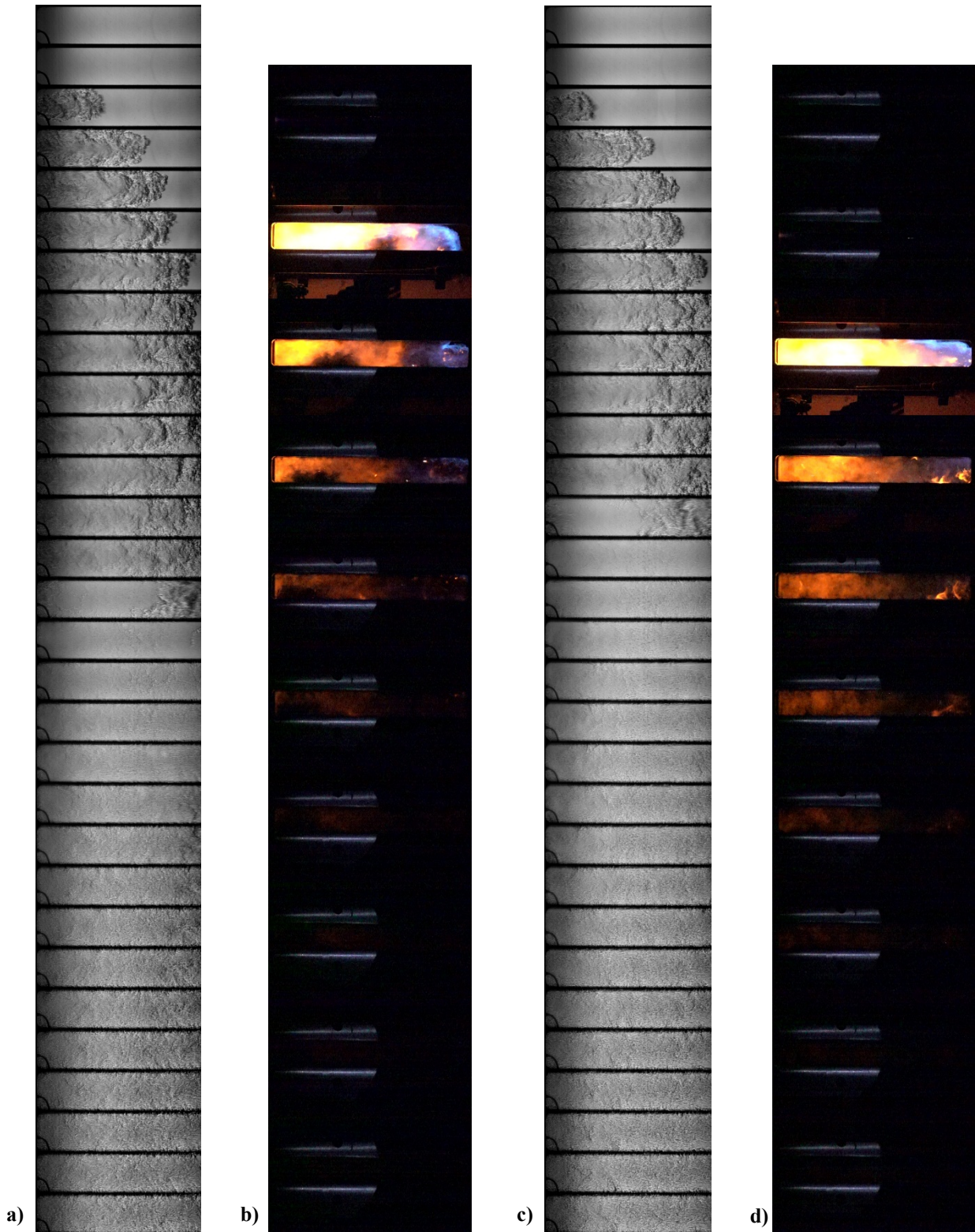


Figure 3.41. Filmstrips for two methane-hydrogen ($\Phi=1$) test cases: a) schlieren and b) flame luminosity for Trial 156: $\tau_{\text{mix}}=0\text{s}$, no pump; c) schlieren and d) flame luminosity for Trial 169: $\tau_{\text{mix}}=30\text{s}$, pump.

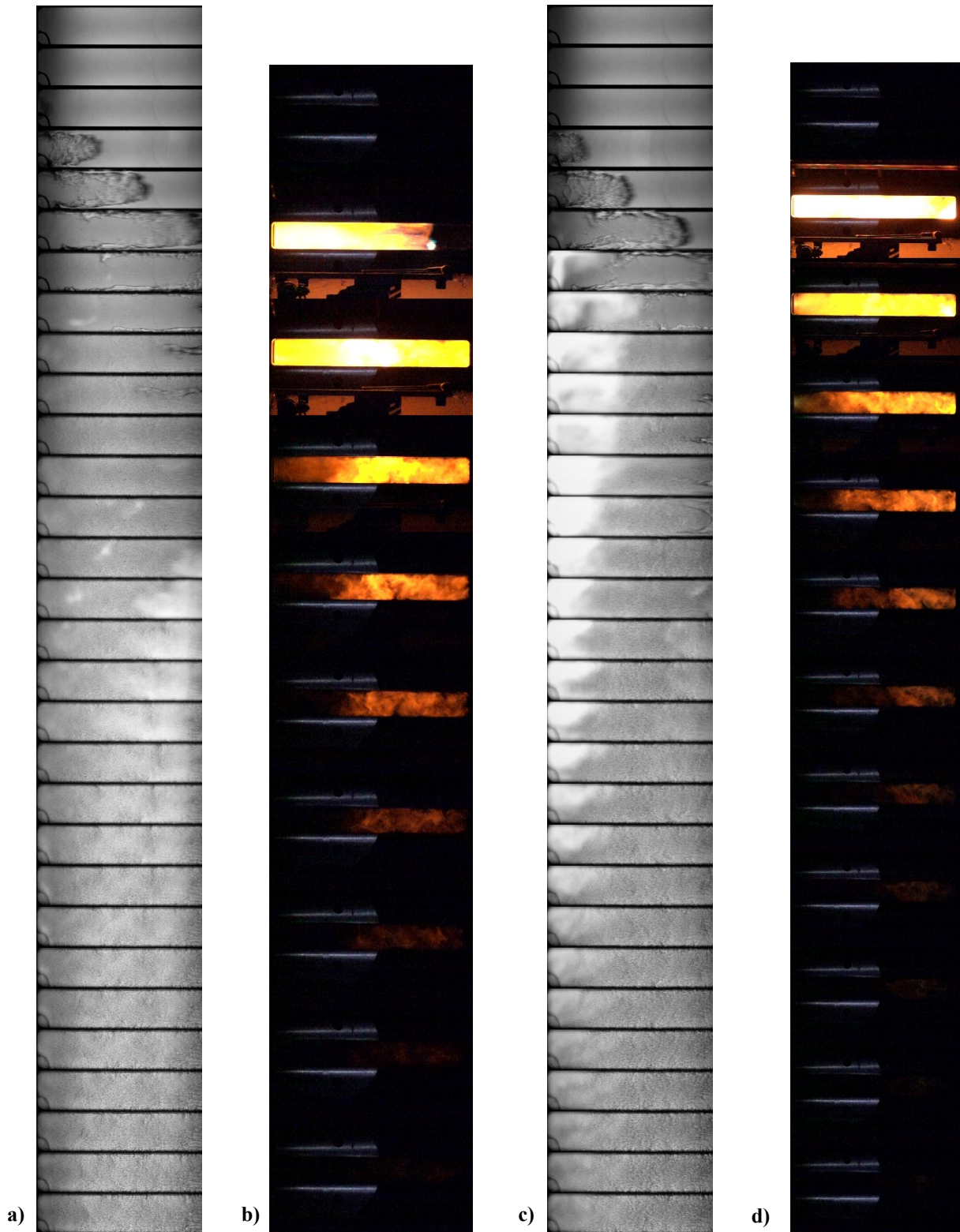


Figure 3.42. Filmstrips for two hydrogen ($\Phi=1$) test cases: a) schlieren and b) flame luminosity for Trial 125: $\tau_{\text{mix}}=0\text{s}$, no pump; c) schlieren and d) flame luminosity for Trial 138: $\tau_{\text{mix}}=30\text{s}$, pump.

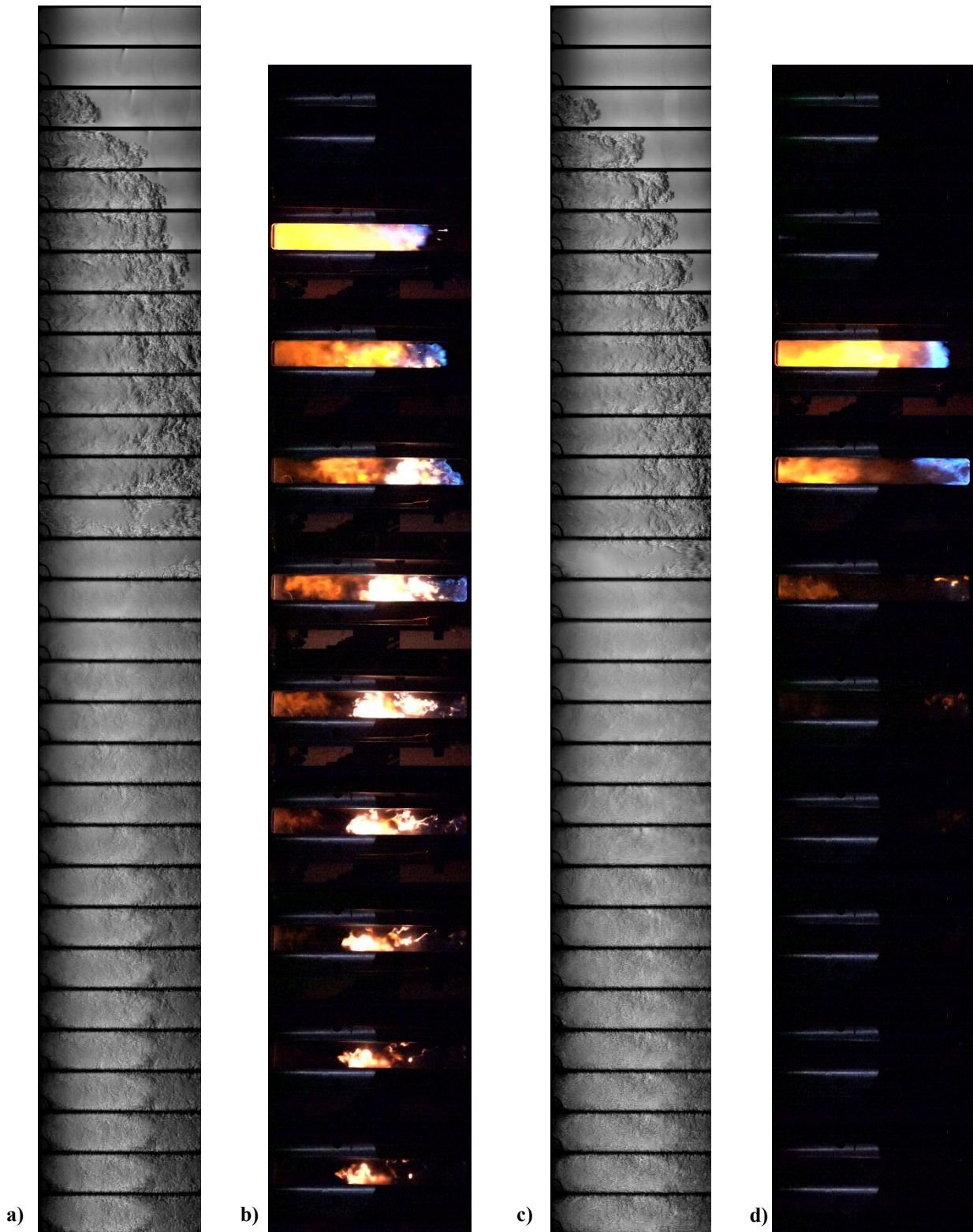


Figure 3.43. Filmstrips for two propane ($\Phi=1$) test cases: a) schlieren and b) flame luminosity for Trial 182: $\tau_{\text{mix}}=0\text{s}$, no pump; c) schlieren and d) flame luminosity for Trial 193: $\tau_{\text{mix}}=30\text{s}$, pump.

3.3 Leak Analysis

This subsection takes a look at the data gathered during the leak analysis experiments. Traversing HJI cases were initially tried a multitude of times; however, the pre-chamber refused to trigger a consistent rupture moment, and as a result, traversing cases were set aside in favor of a more detailed analysis on the leakage rate experienced during traversing cases, especially with the addition of a new pump system. Data was collected while the oil-impregnated seal plate was kept on the main chamber and the chambers were coupled together, and the pump orientation was flipped so that pumping and diffusion effects could be analyzed for both rotational and non-rotational situations. Comparisons between some of the different cases' schlieren videos and pressure data plots are provided below. While data was collected for propane, hydrogen, and methane, only the propane cases will be showcased in this subsection, for they present the most visually noticeable data sets while also representing the phenomena that occurred with all three fuels.

3.3.1 Schlieren Visualization

Each test was performed twice, with the Phantom high-speed camera pointed at either the front or back of the main chamber for each test. For the stationary videos, as highlighted in Fig. 3.44, the pumping port is clearly present with a lot of turbulent mixing, while the suction port is serving as a method of drawing some of the fuel back to the far end of the chamber. Looking at the front end (the first link), the suction action of the pump appears to draw in fluid from left of the pump port – where the little nozzle cavity is accessible through the nozzle exit – as well as from the fueling port on top of the chamber. There is a potential for air to enter the system from this front end as well, for the bronze seal plate does not allow for a perfectly flush seal, especially at the bottom of the plate.

Figure 3.44. Video links for two propane ($\Phi=2$) 0 RPM top-to-bottom pump leak test case, with a.) [the first video of the front of the main chamber](#) and b.) [the second video being the back of the main chamber](#).

Next, the rotational set of cases offered intriguing results pertaining to the leakage of the system, which is best showcased in Figs. 3.45. At 400 rpm, there seems to be a little vortex present throughout the duration of the traversing cases, but it only affects the front half of the chamber.

On top of this, a particularly alarming situation in which there are moments where an exceptionally large plume of fluid rushes into the front part of the chamber. After calculating the frequency of when this occurs, it seems to coincide with the frequency of the pre-chamber rotation at 400 rpm. Presumably, this rush of air is caused by the solid nozzle insert coming in line with the front main chamber opening. Because there is a large gap between the pre-chamber face and the solid insert face, the nozzle is able to connect the outside surrounding air with the inside of the main chamber for a very brief moment. However brief this moment is, though, it is enough time for a large rush of air to enter the main chamber, especially in cases where the pump also happens to be in its suction phase. This large plume of air can greatly affect the equivalence ratio held within the main chamber and throw off the results of an experiment. Additionally, the suction port has a little vortex ring that comes out of it during these times in other videos as well. While also present in the stationary cases, the traversing ones tend to be larger and correspond with this nozzle insert alignment. Overall, these videos show the desperate need for better sealing in the traversing cases, especially if one is to use the pump when conducting them.

Figure 3.45. Video links for two propane ($\Phi=2$) 400 RPM top-to-bottom pump leak test case, with a.) [the first video of the front of the main chamber](#) and b.) [the second video being the back of the main chamber](#).

3.3.2 Pressure Histories

The pressure data for these kinds of cases is also very telling with regards to leakage from the main chamber. In Fig. 3.46a, the pressure from a leak case looking at a stationary pre-chamber and oil-impregnated bronze seal plate is plotted to provide a baseline against the rotational case. With it being a stationary case, the pressure holds relatively well in the chamber while pumping. The lines are consistent and showcase the periodic nature of the recirculation pump. Figure 3.46b on the other hand shows a traversing case, and its plot is very remarkable. Not only does the plot indicate that pressure is being lost in the main chamber system during rotation, but also, there appears to be an oscillatory nature going on, seen by the amplitude of the line decreasing before slightly increasing again toward the end of data collection. This could be due to continual encounters with the solid nozzle insert in the form of a beat frequency.

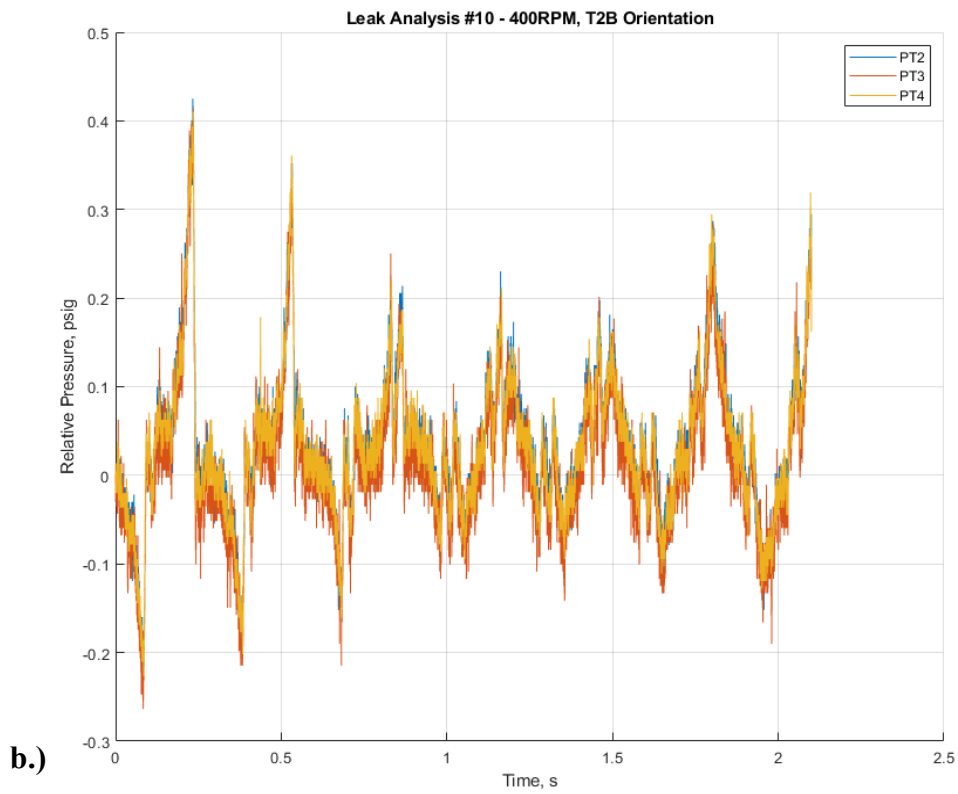
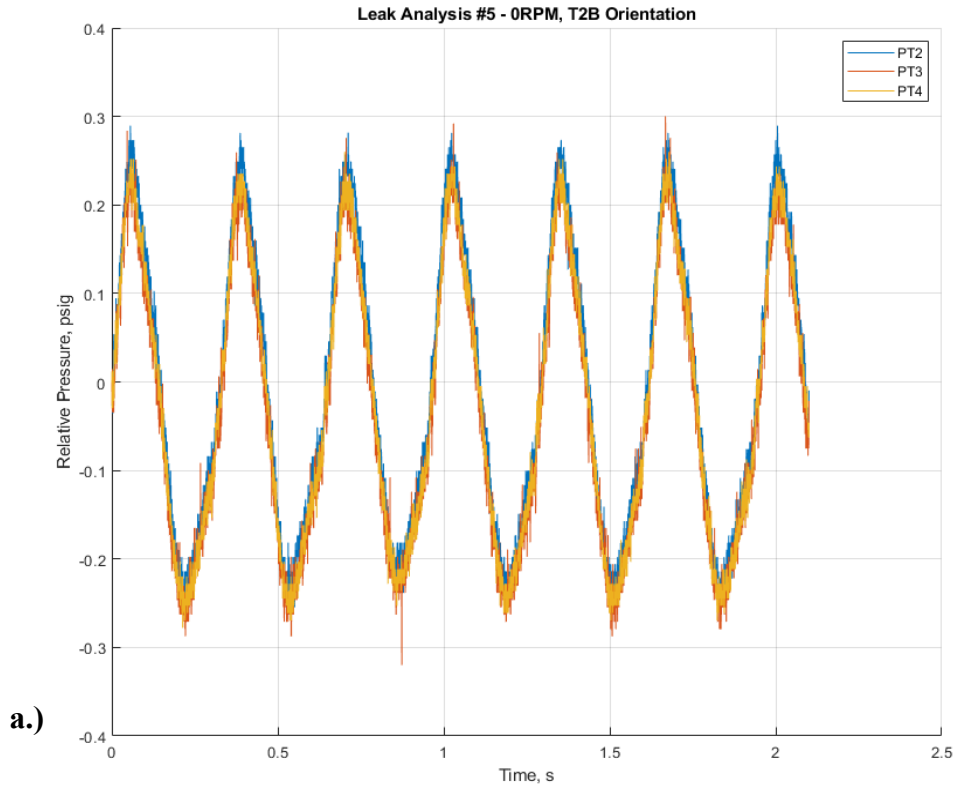


Figure 3.46. Pressure history plots for a propane ($\Phi=2$) a.) 0 RPM top-to-bottom pump leak test case and b.) 400 RPM top-to-bottom pump leak test case.

3.3.3 Recommendations

The current bulb pump has an internal volume of around 32.4ml, and total, the pump system has a volume of around 165ml – making the main chamber volume when the pump is engaged around 969.3ml. To pump the entire chamber's worth of volume through the pump one time over, one would need to pump the system 30 times. For the experiments performed in this study, the pump was cycled 30 times every 10 seconds. In the schlieren footage, the plumes of fuel-air mixture from the pump begin to blend in and become difficult to see within the first 10-15 seconds of pumping, after around 30-45 pumps have occurred. Therefore, pumping the system for 1 chamber-volume's worth of times should mix the inside of the chamber well enough for adequate fuel distribution. As seen in the previous sections, the best results come after pumping the system for 30 seconds; however, as seen in the videos, a lot of leaking can occur in that amount of time, so it is best to try and reduce the time it takes to pump the system. At the very least, it is recommended that the recirculation system be pumped only around 30 times with the given setup.

Another option that has been carried out already is to design a new pump system featuring a thinner hose to reduce the total volume of the main chamber pump system. With the new piping, the pump system's volume was reduced from 165ml to around 81.5ml, which means the pump only needs to be used for around 25 or less pumps in order to achieve the same effect. This helps reduce the chances of leakage from the system while also making the experimentation process more efficient overall.

Lastly, for traversing cases specifically, it is recommended that a new solid nozzle insert be designed so that there is not a gap that produces such a large intake of surrounding air into the system and thus diluting the experiments. Along with this, the main chamber is currently only able to sweep in a radial fashion on the horizontal plane so as to allow for a good flush contact surface to be found in order to create the dynamic seal with the bronze seal plate. However, it does not have this feature in the vertical orientation, and thus there is a gap towards the bottom of the deal plate that allows for the fuel-air mixture to escape during traversing experiments. This should be corrected in order to give the seal plate the best chance at creating a seal and prevent as much leakage as possible in the system.

4. SUMMARY

4.1 Conclusions

An experimental study was performed for the purpose of comparing fuel-air mixing methods and determining an effective way at minimizing stratification effects within a constant-volume combustion. The experimental setup was comprised of a rotating cylindrical pre-chamber and a fixed rectangular main chamber, with the pre-chamber housing a nozzle that formed a jet of hot combustion products that entered the main chamber as a source of ignition known as hot jet ignition. The pre-chamber always contained a 50%-50% methane-hydrogen fuel-air mixture set at a 1.1 equivalence ratio; however, the main chamber fuel was varied between different hydrocarbon fuels. To mitigate stratification, a new circulation pump was designed and implemented on the main chamber. For each experiment, pressure data is collected through several pressure transducers embedded in the chambers, and there are two cameras recording the internal combustion phenomena within the main chamber.

To study the spark-ignited flame propagation within the main chamber, a spark plug seal plate was used to seal the main chamber while it was fueled with methane, 50%-50% methane-hydrogen, 46.4%-53.6% methane-argon, hydrogen, and propane to make equivalence ratios of either 0.4, 0.7, 1.0, or 1.3. Additionally, the chamber was allowed to sit for 0, 10, and 30s before ignition to encourage diffusive mixing as a baseline, and the pump was used for 10 and 30 seconds in different cases in order to compare. For cases in which a stationary hot jet was used to ignite the main chamber, methane, methane-hydrogen, hydrogen, and propane fuels were used at the same equivalence ratios, and the pre-chamber and main chamber were coupled together. Instead of the full range of mixing options, however, the pump was only used for 30s for half of the tests while the other half had no time to mix. Lastly, for leak analysis of the main chamber during traversing cases, the main chamber was filled with propane (at $\Phi=2.0$), methane (at $\Phi=1.0$), and hydrogen ($\Phi= 1.0$) while the pre-chamber was kept empty and rotated at 0 and 400rpm. Similar to the stationary cases, the pump was either used for only 15s or not at all in order to compare the initial mixing conditions.

For the spark-ignited flame propagation tests, the camera footage showed more symmetrical flame propagation in cases where the pump was used over cases in which diffusion was the primary

mixing method. Additionally, pump cases experienced higher pressures for longer periods of time while the overall combustion events were shorter than their non-pump case counterparts. For every 30s of diffusion, 10s of pumping produced around the same results, and the longer the pump was allowed to go, the more the mixture became evenly distributed based on the visual and pressure data. Many times, fuels would not combust, no matter how many times were attempted, such as methane, methane-argon, and propane at $\Phi = 0.4$. Overall, when the pump was not used, fuels that were denser than air (e.g., propane) were shown to spread only along the bottom of the main chamber, while “lighter” fuels floated primarily along the top (e.g. hydrogen, methane, etc.) – as visualized by the asymmetric flame front shapes. Additionally, the pump orientation and pumping rate mattered when distributing fuels. “Heavy” fuels like propane distribute best when the pump takes the fuel-air mixture from the bottom front of the chamber and delivers it to the top back port. On the other hand, “lighter” fuels distribute best when taken from the top back portion of the chamber and brought to the bottom front port of the tank. Each fuel had the most consistent success during the trials when pumped at a rate of 30 pumps every 10s, as well. Overall, pumping in this manner with the fuel’s density taken into account showed a dramatic reduction in fuel-air stratification and buoyancy effects and has proven to be a necessary step in the process of studying pressure-gain combustion and wave rotor combustors.

Stationary hot jet ignition tests also saw similar benefits from the use of the pump. While similar pressure effects were seen, the propagation of the jet in the main chamber was quite different. Upon further analysis, the issuing jet from the pre-chamber can travel faster and a little farther before ignition occurs due to the evenly distributed, relatively homogenous environment of the main chamber following adequate pumping. Furthermore, ignition delay time between the moment the jet enters the main chamber and the moment the main chamber fuel combusts was noticeably affected by the pump. For recirculated fuel-air mixtures, the ignition delay time is shorter than in cases where the pump is not used; however, the shock speeds tend to increase only slightly with sufficient pumping, if at all. Overall, these properties are crucial to understanding constant-volume combustion systems and improving them for future implementation into everyday life. As such, accuracy is necessary in making sure these devices are capable of major tasks, so they must be accurate. While a manual hand pump will not be implemented into a wave rotor combustor, it serves the vital need of ensuring that the conditions within the laboratory model are as accurate to real-world conditions as possible.

While traversing cases were unable to be performed for this study, the rotating pre-chamber was still able to help in determine the leakage occurring in the main chamber during traversing experimental setups, which has potentially changed due to the addition of the recirculation pump. The footage from these cases revealed several beneficial and unfortunate phenomena. On the positive side, the traversing movement of the pre-chamber as well as the pumping action of the pump proved to be much better at mixing than previously thought. The pump, itself, produces numerous vortex rings during its pumping phase, and the resulting vortex shedding promotes extra mixing opportunities as opposed to a more laminar pumping jet. Additionally, the rotation of the pre-chamber induces a bulk vortex motion in the front of the main chamber, which only boosts mixing even further. Unfortunately, the leakage during traversing cases is incredibly significant and made only worse by the addition of the pump. At times, a large intake of outside air will rush into the system, caused by the alignment of the pump's suction action with the passing-by of the solid pre-chamber nozzle insert. The several courses of action exist to reduce these major leaks in the system, though. One method has already been implemented, with the volume of the pump system having been reduced by half, thereby requiring less pumps to cycle the main chamber contents. Additionally, the pre-chamber nozzle insert and the traversing oil-impregnated bronze seal plate should be redesigned/adjusted to prevent gaps in the system that allow air and fuel to leak into and out of the system.

4.2 Recommendations

1. The current primary visualization technique for combustion in the main chamber is through a Z-type schlieren setup, and so far, it has been very effective at visualizing the processes within the chamber. However, this method does not capture all of chamber and requires multiple runs of the same experiment in order to full visualize the flow. Implementing a background-oriented schlieren setup in conjunction with the main chamber would provide the entire chamber in the field of view of the schlieren recordings, as well as require less equipment in the way of the machinery. Additionally, if done properly, the flow field density and refractive index information gathered from this technique could be used to find the temperature of the flow field as well. The quartz glass' ability to absorb much of the light that passes through the chamber will need consideration, but this information would be a great benefit in studying the main chamber combustion events.

2. The fueling station works well for the purposes of the lab, but since its creation, the lab itself has changed quite a bit over time. The option of different fuel tank sources is helpful, but the construction of the mass flow controller piping in its current design only gives two points of contact for support in keeping the device level – one of which is the threaded port, which more than likely will develop a leak over time if continual strain is kept on it. Perhaps a simpler station can be designed in which the fuel tanks can directly connect to the mass flow controller, thus minimizing points of failure and potential leaks and ensuring the fuel mixtures do not become diluted from previously stored gases in the mixing tank.
3. The current oil-impregnated bronze seal plate, while a good idea that is worth keeping and using, is not very effective in the rig's current state because the face plate itself is unable to make a perfectly level contact with the pre-chamber wear plate. The main chamber can be adjusted from left to right to account for this, but it cannot be angled up or down relative to the horizontal plane. Currently, it does not sit very flush, and this allows for a noticeable gap between the pre-chamber and main chamber that allows for fuel mixtures to escape. Creating a way to provide this degree of freedom would vastly improve the maneuverability of the chamber and help with effectively sealing the chamber during traversing cases.
4. Consideration in redesigning the nozzle inserts should be looked at relatively soon. The current ones are effective; however, the inserts used opposite the nozzle do not provide a flush surface when performing traversing experiments, and as seen in the leak assessment, this gap can lead to major leaks from the outside surrounding air into the main chamber during rotation. Additionally, the nozzle insert itself has a high probability of the small screws becoming stripped over time. On top of this, little pieces of the diaphragm are known to end up in-between the screw threads and subsequently get caked onto the screw's threads and become very difficult to remove.
5. The light source used in the current schlieren setup is getting fairly old, and there are more up-to-date LED light sources that could work very well, including some very small, flexible lights that do not require as much covering in order to transform them into point light sources for the schlieren images.
6. Currently, the electrical system controlling the firing of the spark plug in the pre-chamber is not being consistent and leading to extreme randomness as to when in the rotation the

pre-chamber will fire. This should be looked at carefully and remedied as soon as possible so that rotation cases are possible once again. This may be an issue with LabVIEW or with the connection between the ignition coil and the pre-chamber spark plug or something else entirely. It is recommended that the whole system be thoroughly evaluated and that fixes are implemented as soon as possible.

7. While the pump design is useful in recirculating the fuel-air mixture throughout the system, there are still some potential places within the main chamber that may experience different local equivalence ratios than other points in the chamber. It is really hard to judge how evenly distributed the fuel-air mixture is without sampling the mixture directly. One way to do this is by adapting an existing pressure transducer port to accommodate a gas chromatograph. Instead of the fuel port, a diaphragm port would allow the taking of gas samples from that location and derive how the local equivalence ratio at that location using the chromatograph. Implementing such a device and sampling port would improve the lab's understanding of how the fuel gets distributed throughout the chamber, and with this knowledge, the main chamber can be further adapted to improve the distribution of fuel throughout the channel.
8. Placing ion sensors along the length of the main chamber or within the inside of the pre-chamber would be another useful way of evaluating gas concentrations during combustion events in the chambers themselves. Another similar idea would be to implement a pressure transducer onto the back of the pre-chamber through one of the extra quick connect fueling ports so that pressure data can still be collected from the pre-chamber, even in traversing cases.

REFERENCES

- [1] Akbari, P., Nalim, R., and Mueller, N., A review of wave rotor technology and its applications, *Journal of Propulsion and Power*, 128(4):717–735, 2006.
- [2] Kentfield, J. and O’Blenes, M., Methods for achieving a combustion-driven pressure-gain in gas turbines, *Journal of Propulsion and Power*, 110(4):704–711, 1988.
- [3] Weber, H. E., 1986, “Shock-Expansion Wave Engines: New Directions for Power Production,” ASME Paper 86-GT-62.
- [4] Weber, H. E., *Shock Wave Engine Design*, John Wiley and Sons, New York, 1995.
- [5] Perera, U. L. I. U., *Experimental investigation into combustion torch jet ignition of methane-air, ethylene-air, and propane-air mixtures*, Master’s thesis, Indiana University Purdue University Indianapolis, 2010.
- [6] P. Akbari and M.R.Nalim, “Review of recent developments in wave rotor combustion technology,” *Journal of Propulsion and Power*, vol. 25, no. 4, pp. 833–844, 2009.
- [7] Kojok, A. T., *Hot Jet Ignition Delay Characterization of Methane and Hydrogen at Elevated Temperatures*, Master's Thesis, Mechanical Engineering Department, Indiana University-Purdue University Indianapolis, Indianapolis, IN, 2017.
- [8] Nalim, M.R., Longitudinally stratified combustion in wave rotors, *J. Propul. Power*, 16(6):1060–1068, 2000.
- [9] Wijeyakulasuriya, S. D., *Transient and translating gas jet modeling for pressure gain combustion applications*, PhD thesis, Purdue University, West Lafayette, 2011.
- [10] Nalim, M.R., Preliminary assessment of combustion modes for internal combustion wave rotors, *ASME J. Eng. Gas Turbines Power*, 121(2):265–271, 1999.
- [11] Nalim, M.R., Snyder, P.H., and Kowalkowski, M., Experimental test, model validation, and viability assessment of a wave-rotor constant-volume-combustor, *Journal of Propulsion and Power*, 33(1):163–175, 2017.
- [12] Knauff, R., “Converting pressures of liberated gas energy into mechanical work,” British Patent 2818, 1906.
- [13] Knauff, R., “Converting Internal Gas Energy into Mechanical Work,” British Patent 8273, 1906.
- [14] Burghard, H., “An Improved Compressor or Air Pump,” British Patent 19421, 1913.

- [15] Lebre, A.F., "Method and apparatus for compressing fluids," British Patent 290669, 1928.
- [16] Burghard, H., "Process for compressing gases," German Patent DE485386C, 1928.
- [17] N. Energie-Forschungs-Fonds and H. Gränicher, *NEFF 1977-97: Förderung der Energieforschung : allgemeiner Rechenschaftsbericht zum Abschluss der Tätigkeit des NEFF; Bedeutung der NEFF-Förderung; zwanzig ausgewählte Forschungsprojekte.* vdf, Hochschulverlag an der ETH Zürich, 1997.
- [18] Claude, S., "Gas turbine installation," US Patent 2461186, 1949.
- [19] Pearson, R.D., A pressure exchange machine for burning Pyroil as the end user in a cheap power from biomass system, 15th International Congress of Combustion Engines, Paris, 1983.
- [20] Mathur, A., A brief review of the GE wave engine program, Proceedings of ONR/NAVAIR Wave Rotor Research and Technology Workshop, Report NPS67-85-008, pp. 171-193, Naval Postgraduate School Monterey, CA, 1985.
- [21] Colman, R.R., Wave engine technology development, Final Report of GPC for AFWAL, Contract No. AFWAL-TR-83-2095, 1984.
- [22] Moritz, R., Rolls-Royce study of wave rotors (1965-1970), Proceedings of ONR/NAVAIR Wave Rotor Research and Technology Workshop, Report NPS67-85-008, pp. 116-124, Naval Postgraduate School Monterey, CA, 1985
- [23] Rose, P.H., Potential application of wave machinery to energy and chemical processes, *Proceedings of the 12th International Symposium on Shock Tubes and Waves*, pages 3–30, 1979.
- [24] Nalim, M.R. and Paxson, D.E., A numerical investigation of premixed combustion in wave rotors, *ASME J. Eng. Gas Turbines Power*, 119(3):668–675, 1997.
- [25] Snyder, P.H., Wave rotor demonstrator engine assessment, NASA CR-198496, 1996.
- [26] Lear, W.E. and Candler, G., Direct boundary value solution of wave rotor flow fields, AIAA Paper 93-0483, 1993.
- [27] Okamoto, K., Nagashima, T., and Yamaguchi, K., Introductory investigation of micro wave rotor, ASME Paper IGTC03-FR-302, Japan, 2003.

- [28] T. Ma, H. Zhao, J. Li, and N. Ladommatos, “Experimental investigation of controlled auto-ignition (cai) combustion in a 4-stroke multi-cylinder gasoline engine and drive cycle simulations,” *A new generation of engine combustion processes for the future*, pp. 115–124, 2001.
- [29] Sadanandan, R., Markus, D., Schiel, R., U. Maas, Olofsson, J., Seyfried, H. M. Richter, and Alden, M., Detailed investigation of ignition by hot gas jets, *Proceedings of the Combustion Institute*, 31(1):719–726, 2007.
- [30] Elhsnawi, M. and Teodorczyk, A., Experimental study of hot inert gas jet ignition of hydrogen-oxygen mixture, *First International Conference on Hydrogen Safety*, Pisa, Italy, pages 8–10, 2005.
- [31] Iglesias, I., Vera, M., Sanchez, A., and Linan, A., Numerical analyses of deflagration initiation by a hot jet, *Combustion Theory and Modelling*, 16(6):994–1010, 2012.
- [32] Biswas, S. and Qiao, L., Prechamber hot jet ignition of ultra-lean h₂/air mixtures: Effect of supersonic jets and combustion instability, *SAE Int. J. Engines*, 9(3), 2016.
- [33] A. Karimi, M. Rajagopal, and R. Nalim, “Traversing hot-jet ignition in a constant-volume combustor,” *Journal of Engineering for Gas Turbines and Power*, vol. 136, no. 4, 2014. Paper No: GTP-13-1325; doi: 10.1115/1.4025659.
- [34] Attard, W.P., Toulson, E., Huisjen, A., Chen, X., Zhu, G., and Schock, H., Spark ignition and pre-chamber turbulent jet ignition combustion visualization, Technical Report, SAE Technical Paper, 2012.
- [35] Adams, T.G., Torch ignition for combustion control of lean mixtures, Technical Report, SAE Technical Paper, 1979.
- [36] Garrett, T. K., Porsche stratified charge engine, *Environmental Science & Technology*, 9(9):826–830, 1975.
- [37] Brandstetter, W., The Volkswagen lean burn pre-engine concept, Technical Report, SAE Technical Paper, 1980.
- [38] E. Toulson, H. J. Schock, and W. P. Attard, “A review of pre-chamber initiated jet ignition combustion systems,” tech. rep., SAE Technical Paper, 2010.
- [39] Bilgin, M., *Stationary and rotating hot jet ignition and flame propagation in a premixed cell*, PhD thesis, University of Washington, Seattle, Washington, 1998.

- [40] Chinnathambi, P., *Experimental investigation on traversing hot jet ignition of lean hydrocarbon-air mixtures in a constant-volume-combustor*, Master's thesis, Indiana University Purdue University Indianapolis, 2014.
- [41] Paik, Kyong-Yup, *Experimental investigation of hot-jet ignition of methane hydrogen mixtures in a constant-volume combustor*, Master's thesis, Indiana University Purdue University Indianapolis, 2016.
- [42] Chowdhury, M. A. Z., *Traversing hot jet ignition delay of hydrocarbon blends in a constant volume combustor*, Master's thesis, Mechanical Engineering Department, Indiana University-Purdue University Indianapolis, Indianapolis, IN, 2018.
- [43] M. A. Hopcroft (2021). LVM file import (<https://www.mathworks.com/matlabcentral/fileexchange/19913-lvm-file-import>), MATLAB Central File Exchange. Retrieved September 28, 2021.
- [44] Froelich, B., Development of single channel wave-rotor rig combustor rig components, CPRL Internal Project Report, 2010.
- [45] Settles, G.S., *Schlieren and shadowgraph techniques: visualizing phenomena in transparent media*, Springer-Verlag, Berlin Heidelberg, 2001.
- [46] Xiao, H., Houim, R., Oran, E., "Formation and evolution of distorted tulip flames," *Combustion and Flame*, Volume 162, November 2015. doi:10.1016/j.combustflame.2015.08.020.
- [47] Matalon M, Metzener P., "The propagation of premixed flames in closed tubes," *Journal of Fluid Mechanics*, April 1997. doi: 10.1017/S0022112096004843Pu.